Storm Tracks, Baroclinic Waves Propagation and Their Interannual Variability in the Northern Hemisphere

by

Yijian Chen
B.S., Peking University, 1995

Submitted to the the Department of Earth, Atmospheric, and Planetary Sciences
in partial fulfillment of the requirements for the degree of

Master of Science

at the

MASSACHUSETTS INSTITUTE OF TECHNOLOGY

September 1997

Author .....
the Department of Earth, Atmospheric, and Planetary Sciences
July, 1997

Certified by .....
Edmund K. M. Chang
Assistant Professor of Meteorology
Thesis Supervisor

Accepted by .....
Thomas H. Jordan
Department Chairman

Storm Tracks, Baroclinic Waves Propagation and Their Interannual Variability in the Northern Hemisphere

by

Yijian Chen

B.S., Peking University, 1995

Submitted to the the Department of Earth, Atmospheric, and Planetary Sciences
on July, 1997, in partial fulfillment of the
requirements for the degree of
Master of Science

Abstract

The goal of this study is to investigate the properties of storm tracks and baroclinic waves propagation in the Northern Hemisphere. The general characteristics and low-frequency (interannual) variability are the central work of this thesis, which are examined in both observational analysis and theoretical interpretation. We use NCEP/NCAR reanalysis data of 12-hourly wind and geopotential height at 300 hpa, isentropic potential vorticity (IPV) at 330K (potential temperature), monthly mean zonal wind and temperature at 700 and 850 hpa in 23 winters (DJF, 1973-1996) and 16 summers(JJA, 1980-1995).

First, complex demodulation technique is applied to meridional wind (v', seasonal mean removed) data to get 12-hourly wave amplitude packets (ve). Based on the data of v' and ve, we compute the timelag correlation (for lags of -2 and +2 days). After this, the wave coherence index (WCI) and packet coherence index (PCI) are constructed to indicate the coherence of waves and wave packets propagation. Contrary to previous study by Wallace et al. (1988), baroclinic wave guides revealed in our study has impressively different distribution with storm tracks, probably due to the unfiltered data we used in calculation of timelag correlation. PCI is found to be in good agreement with the relative change of wave packets in propagation. We suggest that the chaotic development in regions of high baroclinicity can be the reason for the decrease of PCI. 12-hourly group velocity and phase velocity are obtained by tracking the most spatially coherent waves and wave packets between 12-hour time interval, respectively. Based on 12-hourly group velocity, mean growth (decay) rate of wave amplitude following group velocity is calculated. Secondly, theoretical analysis of spatial and temporal coherence of wave packets is given from dispersion view of spatial and temporal packets. The concept of temporal coherence, rather than spatial coherence, is shown to be closer to the timelag correlation. Temporal coherence of wave packets depends on the dispersion relation and group velocity, which can partly explain why the wave coherence is somehow associated with the basic state flow.

Spatial coherence of wave packets, however, is mainly determined by the dispersion relation. We also theoretically analyze two special conditions of spatial coherence of wave packets in the atmosphere. In order to give quantitative indication of spatial coherence of baroclinic waves and wave packets, we apply a box technique to calculate 12-hourly spatial coherence of v' and ve respectively. The spatial coherence index (SCI, time-mean result) of wave packets is found to be higher in the regions of lower meridional IPV gradient in winter and summer. This observation shows that PV front theory isn't good at describing the spatial coherence of baroclinic wave packets. The mid-latitude SCI of baroclinic waves is a bit higher than that of baroclinic wave packets in winter, which suggests the way to forcast weather by exploring the evolution of wave packets may not work in winter.

The interannual variabilities of storm tracks and baroclinic waves propagation are investigated mainly by using the empirical orthogonal function analysis (EOF's) and composite charts. Interannual seesaws of many fields such as westerlies, baroclinicity, RMS(v') are impressive features in midlatitudes. And close relation among these oscillations can be observed. Interannual variability of the first leading EOF mode of RMS(v') is closely associated with the variations of basic state flow and baroclinicity. The relations between other EOF modes and propagations of baroclinic waves and wave packets are also examined. Both WCI and PCI are found to have high relations the interannual variability of storm tracks. We further investigate interannual variations of timelag correlations of v' and ve in different regions along the baroclinic wave guides. Low and high composite charts of basic state flow and intensity of storm tracks, which are constructed according to the seasonal magnitude of of timelag correlation of v', show that higher correlations are always accompanied by intensification of storm tracks, and sometimes by the stronger basic state flow. We also find in general timelag correlation of ve is higher when correlation of v' is higher.

Thesis Supervisor: Edmund K. M. Chang
Title: Assistant Professor of Meteorology

Acknowledgments

I would like to express my sincere thanks to my thesis advisor, Dr. Edmund K. M. Chang. I greatly appreciate his guidance, insightful counsel, and patience throughout the whole process of my thesis research. His allowing me considerable independence to develop my own ideas and conduct the research will definitely benefit me much in future study. I also wish to thank Dr. Mario Molina, who broadened my view on other scientific fields, for his kindness and academic support.

My special thanks are given to my sisters, Yijuan and Yishi, for their continuous concern and suggestions, both in my personality and career choice. Their experience helps me to make some important decisions.

Among the many students and friends I have known here, I express my deep appreciation to Xiaoyun Zang, Yuanlong Hu, Bruce Kuo, Ji-Yong Wang, Stephanie Shaw, Chris Winkler, Jessica Neu, and Adam Sobel, for their inspiration and friendship.

I will also acknowledge PAOC (formerly CMPO) support staff for their excellent work and helpfulness during my stay at MIT.

Finally, the deepest thanks will go to my parents, Jianhui Chen and Sulian Qiu, who gave me the life and help me to explore it. Their love and encouragement continue to inspire me to do my best. To express my thanks, I will dedicate this thesis to them.

Contents

List of Figures

List of Tables

Chapter 1

Introduction

1.1 Description of the dataset and analysis procedures

In a series of recent papers, Chang and Yu (1997, hereafter referred to as CY) applied complex demodulation technique to separate zonal spatial wave packets from their carrier waves, while keeping the wave functions of y (meridional coordinate) and t (time) undemodulated, so that they could follow temporal evolution of zonal wave packets. They also defined some coherence indices to depict the main characteristics of waves and wave packets propagation. In this thesis, we apply CY's method to analyze meridional wind data of 23 winters (DJF, 1973-1996) and 16 summers (JJA, 1980-1995) produced by NCEP/NCAR reanalysis project. Our data consist of 12-hourly wind and geopotential height at 300 hpa, isentropic potential vorticity at 330K (potential temperature), and monthly mean zonal wind, temperature at 700 and 850 hpa. For the purpose of convenience, we describe some concerned methodology next.

First, we demodulate wave field of v' (unfiltered meridional wind at 300 hpa with seasonal mean removed) to get ve, assuming that:

$$v'(x,t) = Re[A(x,t)e^{ikx}] \tag{1.1}$$

where k is the wave number of a typical mid-latitude baroclinic wave, and $A(x,t)$

is the envelope of the wave group and is slowly varying in space. ve is the absolute value of $A(x,t)$:

$$ve = |A(x,t)| \tag{1.2}$$

Secondly, for each base point, we calculate the timelag correlation (for lags of -2 days and +2 days) of v' and ve in every winter season (1973-1996) to get 23 seasonal results. The indications of coherence of waves and wave packets are obtained by averaging the last 16 (1980-1996) timelag correlation maps. [1] The first index, plotted in Fig. 1-1a, is the maximum correlation (in 16-winter mean map) of v' between the base point and the larger of the first negative center or positive center *upstream* with a *negative* timelag of -2 days. It's called wave *upstream* coherence index. Similarly, we construct wave *downstream* coherence index by using *positive* timelag correlation and the result is plotted in Fig. 1-1b. The pattern shown in Fig. 1-1c is the average of the wave upstream and downstream coherence indices and referred to as wave coherence index (WCI hereafter). Following similar steps as above, we construct the packet upstream index (Fig. 1-2a) and downstream coherence index (Fig. 1-2b) for ve. Again, the packet coherence index (PCI hereafter, Fig. 1-2c) is obtained by averaging the packet upstream and downstream coherence indices, which is used as a quantity to show the coherence of wave packets propagation. We strongly recommend readers to read relevant description in CY carefully to get a full understanding of the method and all indices we will use next.

The interannual variabilities of storm tracks and baroclinic waves propagation are investigated mainly by applying the empirical orthogonal function analysis (EOF's) to the 23-season data. Usually, the leading EOF modes will explain the principle variations. More detail about this technique can be found in the works by Peixoto and Oort (1992).

[1] The reason to use 16-season result is just for the purpose of convenience. Actually, we have also looked at the 23-season result and found it's almost the same.

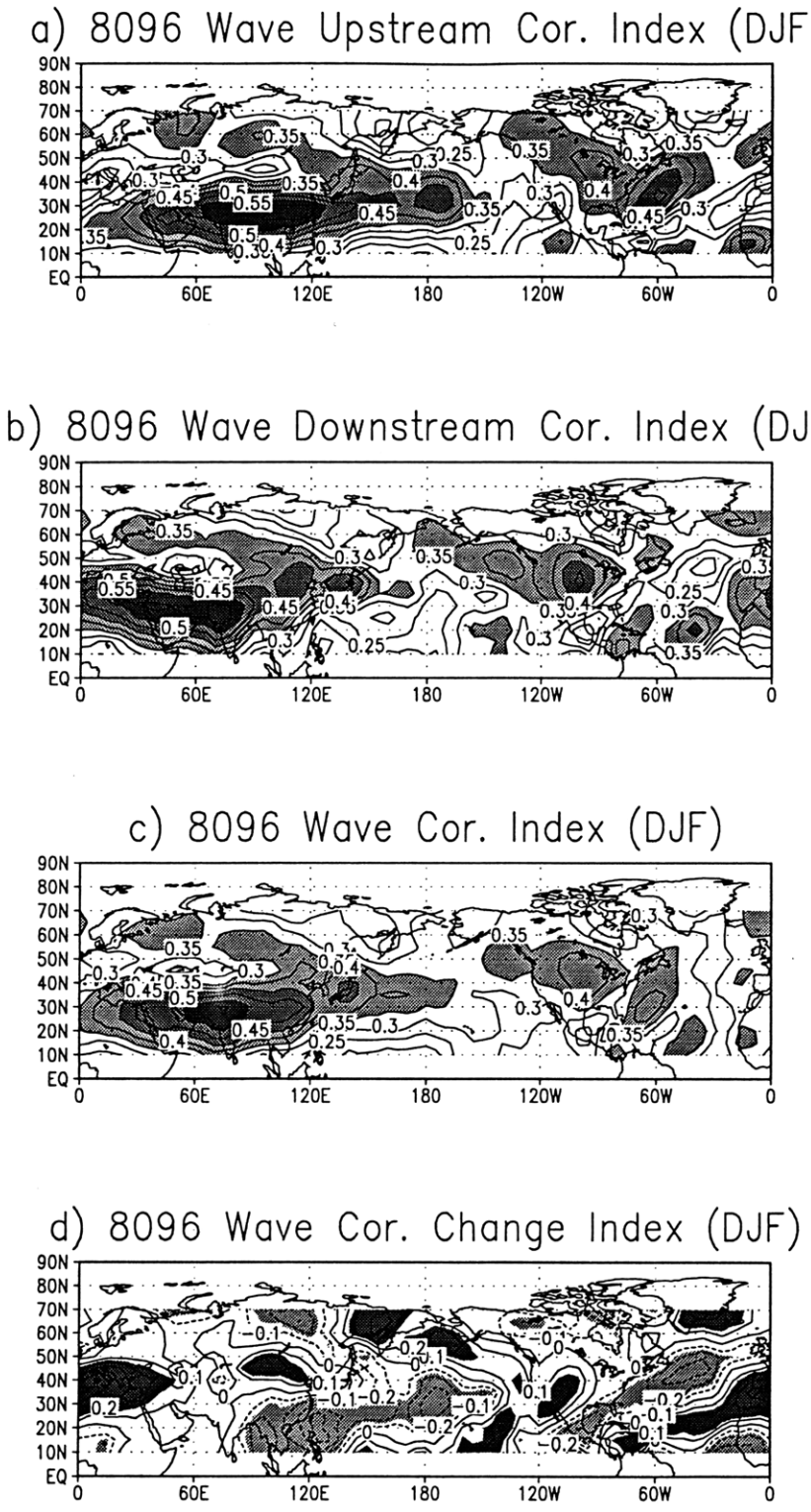

Figure 1-1: a) Wave upstream coherence index. b) Wave downstream coherence indx. c) Wave coherence index (WCI). d) Relative change of wave coherence index. See text for explanation. Contour intervals are 0.05 in a), b) and c) and 0.1 in d). The different shades in a), b) and c) represent values greater than 0.35, 0.45 and 0.55. In d), the dark and light shades represent positive and negative values respectively.

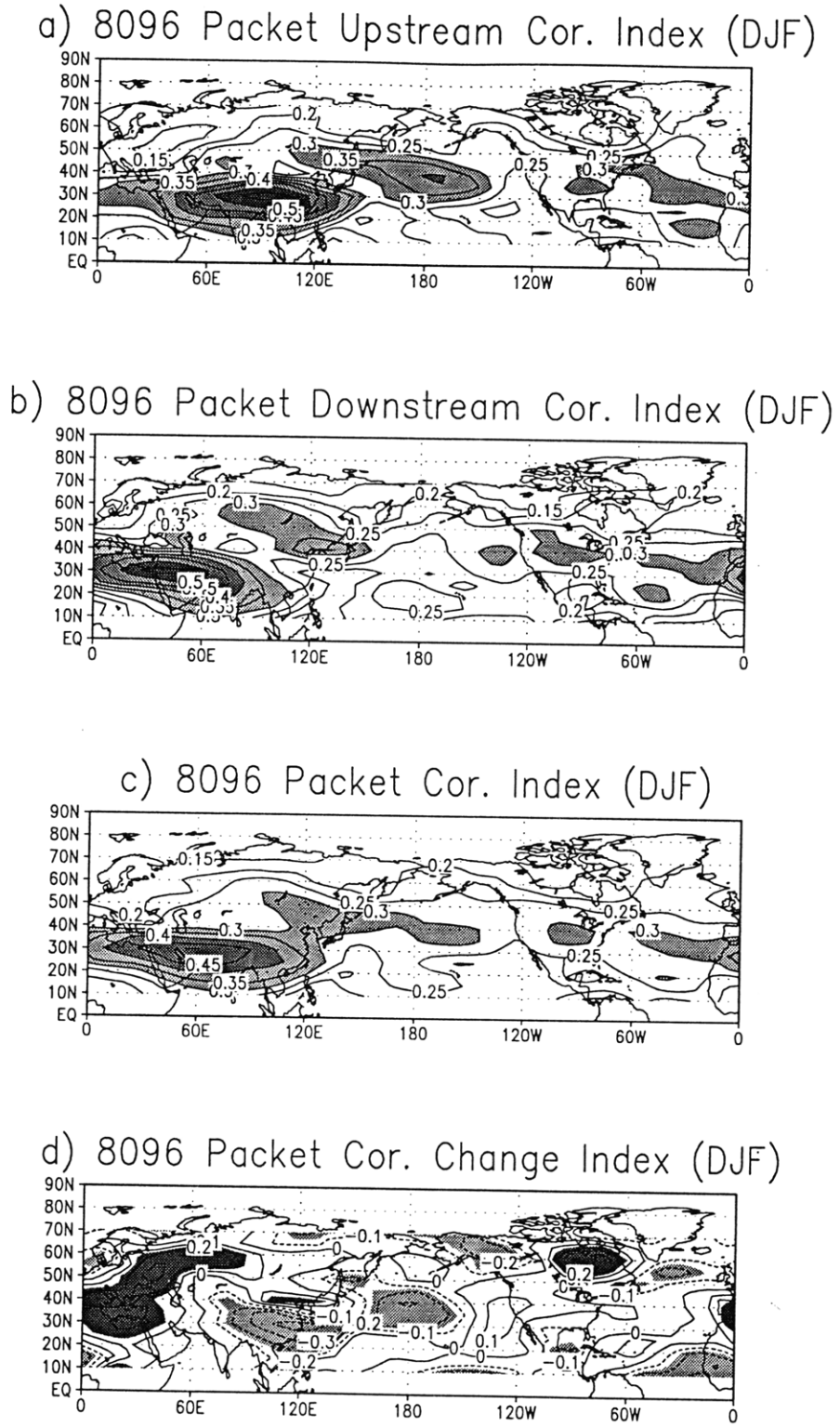

Figure 1-2: a) Packet upstream coherence index. b) Packet downstream coherence indx. c) Packet coherence index (PCI). d) Relative change of packet coherence index. See text for explanation. Contour intervals are 0.05 in a), b) and c) and 0.1 in d). The different shades in a), b) and c) represent values greater than 0.3, 0.4 and 0.5. In d), the dark and light shades represent positive and negative values respectively.

1.2 Review of storm tracks, baroclinic wave guides and spatially coherent path

The term of storm tracks was first brought up by Blackmon (1976). It's referred to a mid-latitude band with the strongest baroclinic activities. However, there are different opinions about how to define this band. Wallace et al. (1988) argued that baroclinic waveguides would be a better term for it because both cyclones and anticyclones contribute to the formation of this band and obviously anticyclones don't bring bad weathers before they move off one local region. The difference between storm tracks and the path of cyclones was pointed out by Nakamura (1992) but the concept of storm tracks was still used in his paper, even though in some sense it was misleading. In Fig. 1-3, we show the standard deviation (RMS hereafter) of three variables: v', ve and z' (time-filtered geopotential height at 300 hpa). Here, RMS patterns for different variables are given for a more complete picture of storm tracks. Difference between filtered and unfiltered data for the wave evolution in storm tracks can be found in papers by Chang (1993) and Berberry and Vera (1996). They found unfiltered meridional wind is better in describing temporal evolution of wave packets. Geopotential height data in this paper are processed using a simple two-step difference filter suggested by Wallace et al..

In Fig. 1-3d, we can see an obvious break in the RMS field of z', which is located between the Pacific storm track and Atlantic storm track. However, such a break in RMS fields of v' and ve isn't impressive. Even some small differences exist among RMS fields of v', ve and z', we still can observe a similar band of maxima (dedicated by dark colors) extending along the middle latitude. Next it will be referred to as storm tracks. Based on the analysis of filtered data, Wallace et al. argued that baroclinic wave guides were located on the same positions as storm tracks thus they were considered to be the same concept. It is found in our study that this is not true. The observed difference between baroclinic wave guides (see shaded band in Fig. 1-2c) [2] and storm tracks is due to the fact that we use unfiltered meridional wind data

[2]In CY, it has been shown that compared with WCI, PCI is better in depicting the baroclinic

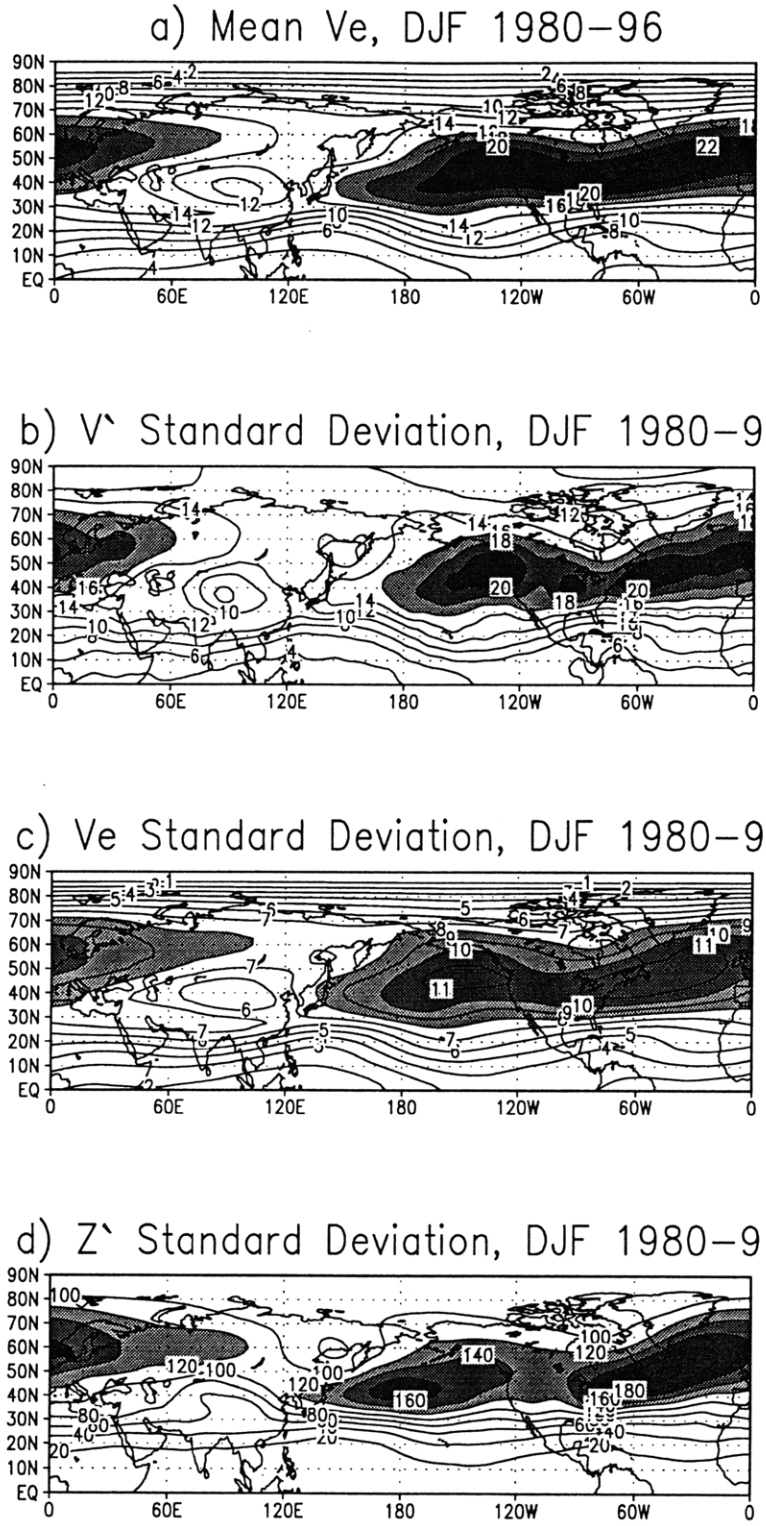

Figure 1-3: a) 16-winter mean of ve. b) Standard deviation of 300 hpa v', averaged over 16 winters. c) Standard deviation of ve. d) Standard deviation of z'. contour intervals are 2 ms^{-1} in a) and b), 1 ms^{-1} in c), and 20 gpm in d). Different shades represent values greater than 16, 18 and 20 in a) and b), 8 and 10 in c), while 120, 140 and 160 in d).

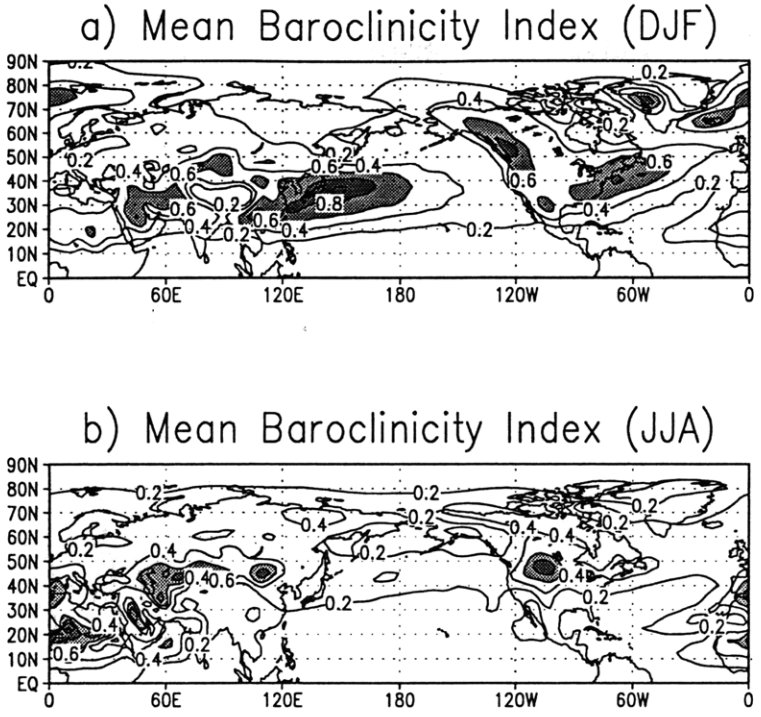

Figure 1-4: a) Eady growth rate in winter, computed from differences between 700 and 850 hpa levels. b) Same as a), except in summer. Contour interval 0.1 day^{-1}. The shades represent values greater than 0.6 and 0.8 respectively.

to calculate the timelag correlation. Next, we shall distinguish two definitions: storm tracks and baroclinic wave guides. Storm tracks are referred to the regions with higher RMS of certain chosen wave variable while baroclinic wave guides are referred to the regions with higher PCI. They have definitely different distribution.

Hoskins and Valdes (1990) argued that diabatic heating is essential to the maintenance of storm tracks, provided that high baroclinicity is the direct reason for storm tracks. Using a channel model, Chang and Orlanski (1993) showed that downstream radiation of fluxes by upstream perturbations is important to the zonal extension of storm tracks.

The baroclinicity index in winter and summer, which actually is Eady Growth Rate at lower level (700-850 hpa):

---

wave guides during Northern Hemisphere winter. Hence we regard PCI as the indication of baroclinic wave guides here.

$$\sigma_{BI} = 0.31 f |\frac{\partial u}{\partial z}| N^{-1} \tag{1.3}$$

is calculated (by using monthly mean zonal wind and averaging all monthly mean results together) and shown in Fig. 1-4. The maximum region in winter (see Fig. 1-4a) is located near the Pacific jet core and definitely is upstream of storm tracks maximum. It seems that storm tracks can't be contributed directly to the local waves development due to high baroclinicity. Pierrehumbert (1984) showed that the most unstable mode of perturbation has a spatial structure which reaches its maximum at the position downstream of the maximum of baroclinicity. Similar results can be found in model simulation study by Whitaker and Dole (1995) and Frederiksen and Frederiksen (1993). This gives some hints that baroclinicity can have, even not direct, but basic effect on the formation and variability of storm tracks. On the other hand, downstream development provides us an useful tool to understand this problem. In short, upper-level wave packets are seeded by low-level baroclinic developments and radiate energy to their downstream regions. Hence the band of high eddy activities (storm tracks) extend some distance into regions of low baroclinicity. We apply a technique based on tracking the most spatially coherent wave packets to obtain 12-hourly group velocity (see section 3.3). After that, growth and decay rate of wave packets ($\frac{dq}{dt}ve$) are calculated. Our results show a basic agreement with above mechanism, but some problems also exist and probably need to be explained from other views. More detail about this will be given in section 3.4.

Based on the theory of PV front wave propagation on $f-plane$, Chang and Yu suggested that the geographical distribution of high PCI is related to the sharp PV gradient in the upper troposphere because in that case group velocity is independent of wave number and dispersive effect is very weak. Theoretical interpretation of packet dispersion, spatial and temporal coherence of wave packets, will be left to sections 5.1 and 5.2. We shall show that PCI and WCI aren't direct and complete in depicting the spatial coherence of wave packets. This can also be seen from the fact that PCI is the collection of maximum timelag correlation of each base point and

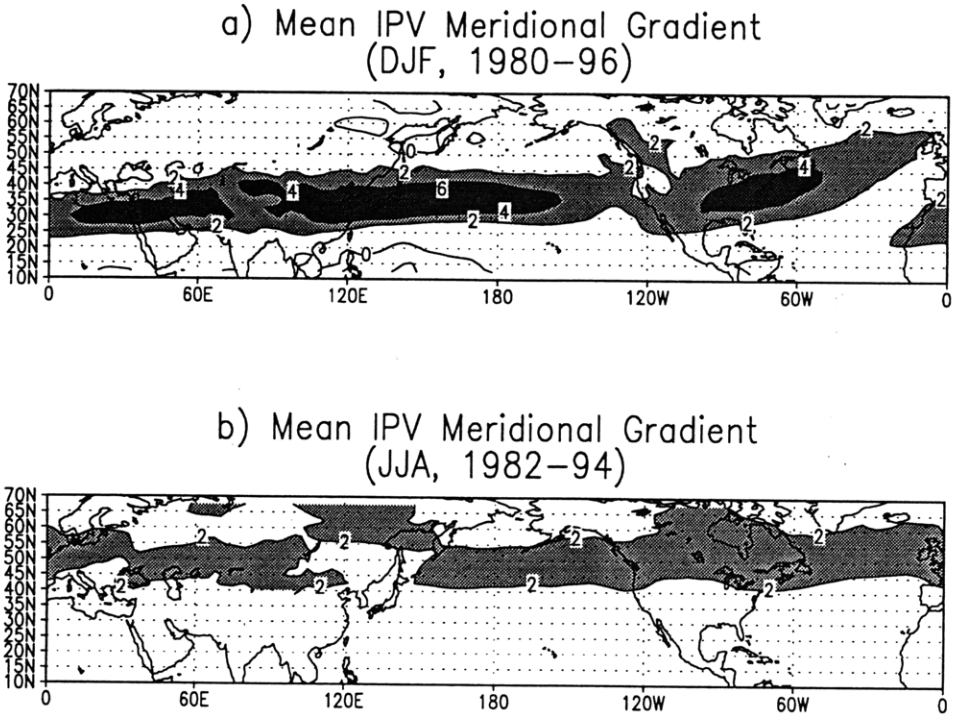

Figure 1-5: a) 16-winter mean of meridional gradient of IPV. b) 13-summer mean of meridioanl gradient of IPV. Contour interval $2 \times 10^{-14} ms^{-1} Kkg^{-1}$. The shades in a) represent values greater than 2 and 4, while in b) values greater than 2 are shaded.

timelag correlations are calculated using time series of ve, instead of spatial series of ve. And observationally, we shall show PCI pattern is in good agreement with relative growth (decay) of propagating wave packets. In addition, our calculation of spatial coherence index suggests that PV front theory isn't good at describing the spatial coherence of baroclinic wave packets.

In chapter 4, we shall define spatial coherence indices of baroclinic waves and wave packets as indications of how (spatially) coherent waves and wave packets remain after passing one region. The bands with higher spatial coherence index will be referred to as spatially coherent path (SCP hereafter) of baroclinic waves and wave packets respectively. We shall see SCP of wave packets in winter and summer definitely is located in the regions of lower IPV meridional gradient. In order to see the influence of baroclinicity on the spatial coherence, we examine the difference between spatial coherence (of waves and wave packets) in winter and that in summer. It seems baroclinicity projects an obvious influence on spatial coherence of waves, but not

on spatial coherence of wave packets. This is different with what Chang and Yu suggested based on the calculation of PCI and WCI. We also find spatial coherence of wave packets in mid-latitude regions is higher in summer than in winter.

Chapter 2

Storm Tracks and Interannual Variability

2.1 Interannual seesaws of storm tracks, mid-latitude westerlies and baroclinicity in winter

2.1.1 Storm tracks

The storm tracks in each winter season are referred to the mid-latitude band with higher seasonal RMS(v'). Seasonal RMS(v') is calculated as before, except in a shorter time period of only one winter. In order to investigate the interannual variation of storm tarcks in winter, we average 23 seasonal RMS(v') fields at first and the interannual anomalies are obtained by removing the 23-winter mean from each seasonal result. The principle modes of interannual variability of storm tracks are identified by applying empirical orthogonal function analysis to above 23 anomalies. Four leading modes (EOF1, EOF2, EOF3, EOF4 hereafter) with the highest percentage of variance explained by them are shown in Fig. 2-1. The percentage is shown at the end of title in each panel. It is seen that these four leading modes collectively account for over 45% of the total variance. Inspection of four patterns in Fig. 2-1 reveals following types of interannual variability of storm tracks.

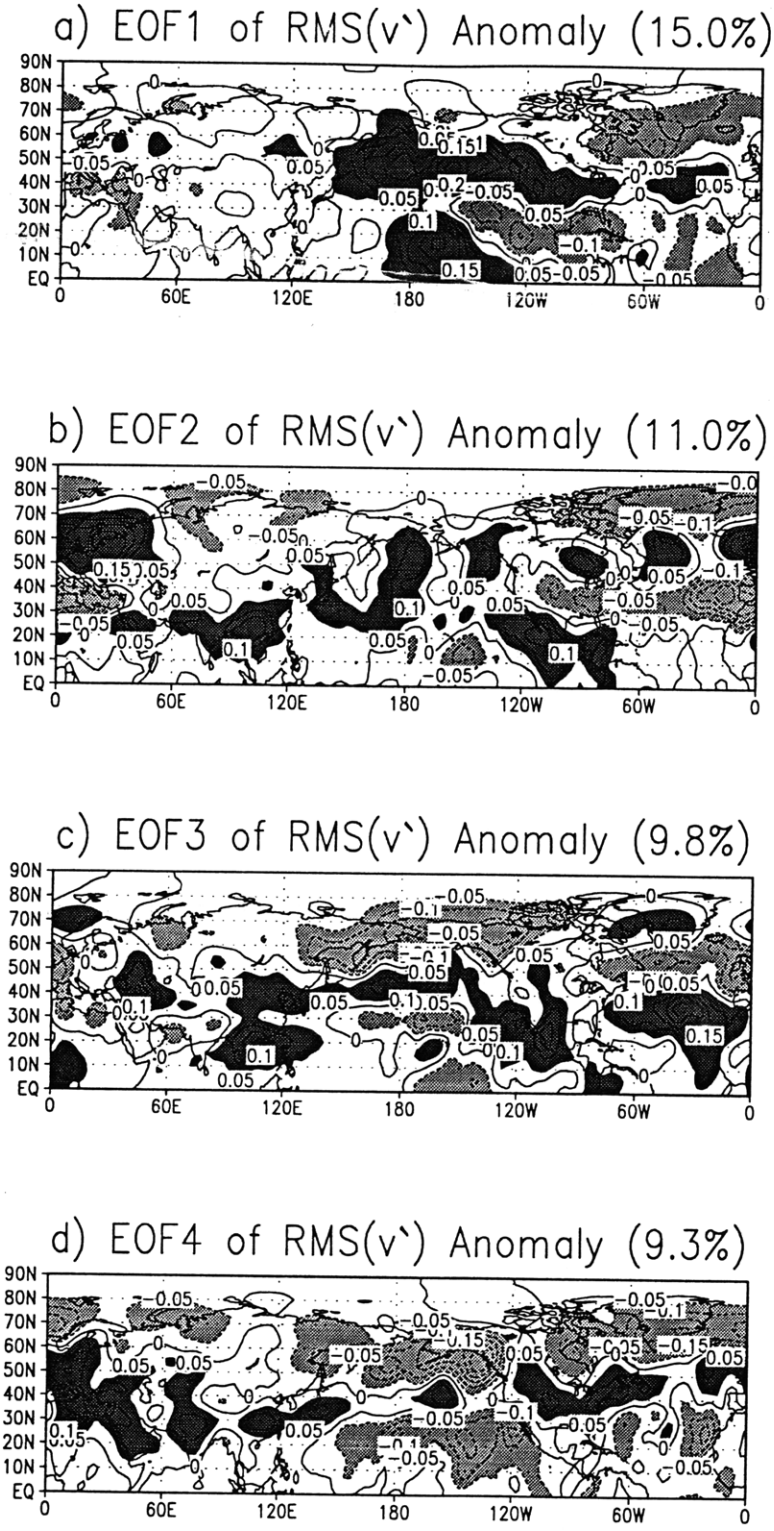

Figure 2-1: a) EOF1 of RMS(v') anomaly. b) Same as a) except for EOF2. c)Same as a) except for EOF3. d)Same as a) except for EOF4. The dark and light shades represent positive and negative values respectively. The percentage explained by each EOF mode is shown at the end of title in the corresponding panel. Contour interval 0.05.

a) EOF1 (Fig. 2-1a): The prominent feature of EOF1 mode is the intensification (weakening) of eddy activities in the main body of storm tracks accompanys the weakening (intensification) of ambient eddies, while bears variation of eddy activities in the middle of low-latitude Pacific. As will be demonstrated in the section 3.6, this mode is mainly controlled by the variations of basic state flow and baroclinicity.

b) EOF2 (Fig. 2-1b): This mode seems to bear variability occurring near the baroclinic wave guide. Hence the first guess is it could have relation with WCI or PCI. In section 3.6, we shall compute the spatial correlation between EOF2 pattern of RMS(v') and the correlation pattern of Fig. 3-13b. The spatial correlation is found to be high (0.72). Also, we carry out similar calculation for PCI and find its EOF1 mode has high correlation with EOF2 of RMS(v').

c) EOF3 (Fig. 2-1c): A dipole structure in the Atlantic and meridional displacements of the position of Pacific storm track are the main characteristics of this mode. What causes the variation of EOF3 isn't clear to us yet.

d) EOF4 (Fig. 2-1d): This mode is characterized by the variation of eddy activities which oscillates between the main body of baroclinic wave guide and ambient regions. As for EOF2 mode mentioned above, we shall compute the spatial correlation (in section 3.6) between EOF4 pattern of RMS(v') and the correlation pattern of Fig. 3-13a and find it's even higher (0.77).

2.1.2 Westerlies

The interannual variabilities of Pacific and Atlantic westerlies can be shown by applying EOF's analysis to the interannual anomalies of Ubar and by calculating simultaneous one-point correlation of Ubar. In Fig. 2-2, we display the four leading EOF modes of Ubar anomalies which depict below characteristics of Ubar variations.

a) EOF1, EOF2 and EOF4 (Figs. 2-2a, b and d): Each mode is characterized by a dipole structure in the mid-latitude Pacific and Atlantic. The dipole seems to be one part of the wave structure which extends northward from the tropical ocean. This probably has relation with planetary stationary wave forced by tropical sea surface temperature (SST) anomalies (Hoskins and Karoly, 1981). All these modes don't

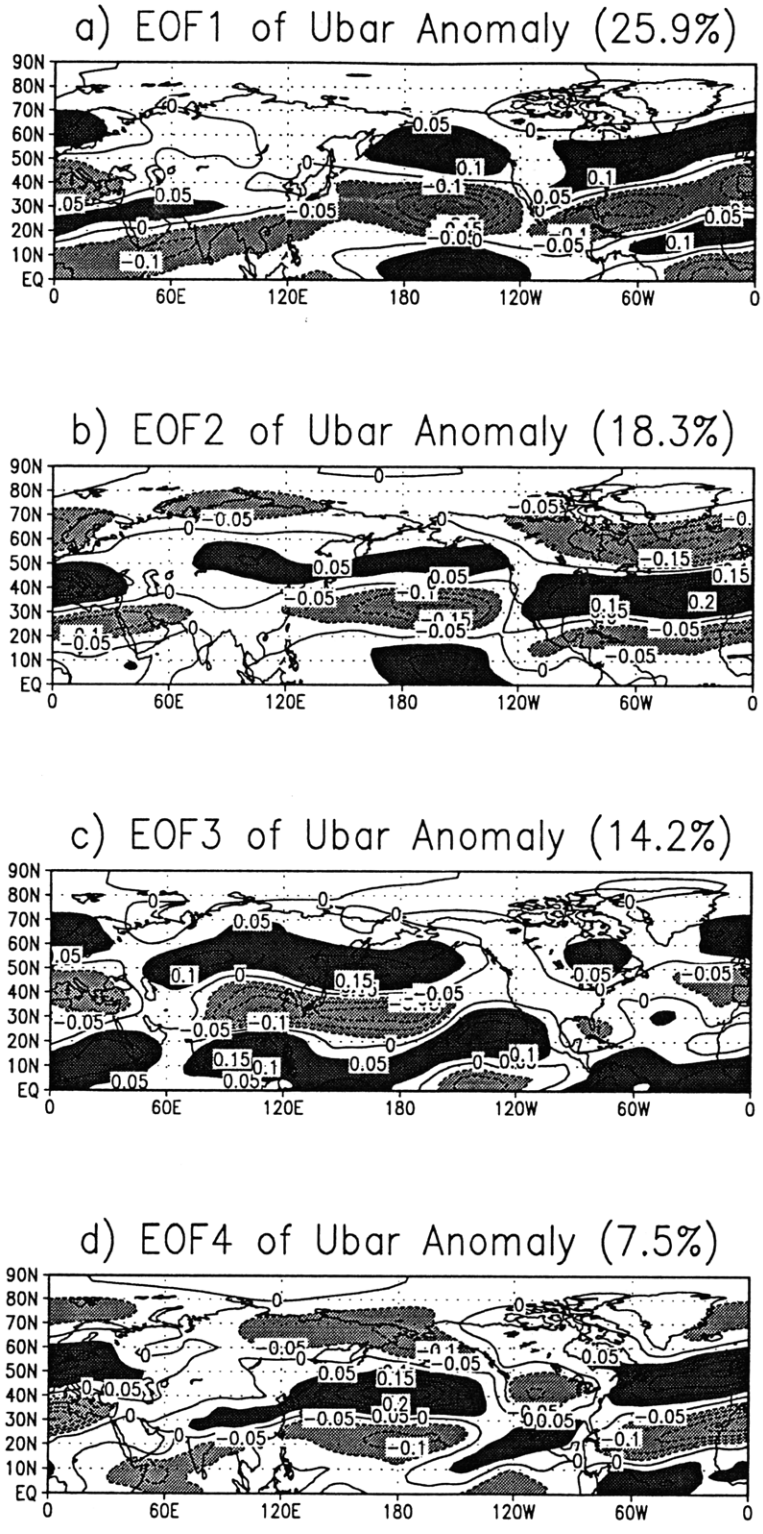

Figure 2-2: Same as Fig. 2-1 except for basic state flow Ubar.

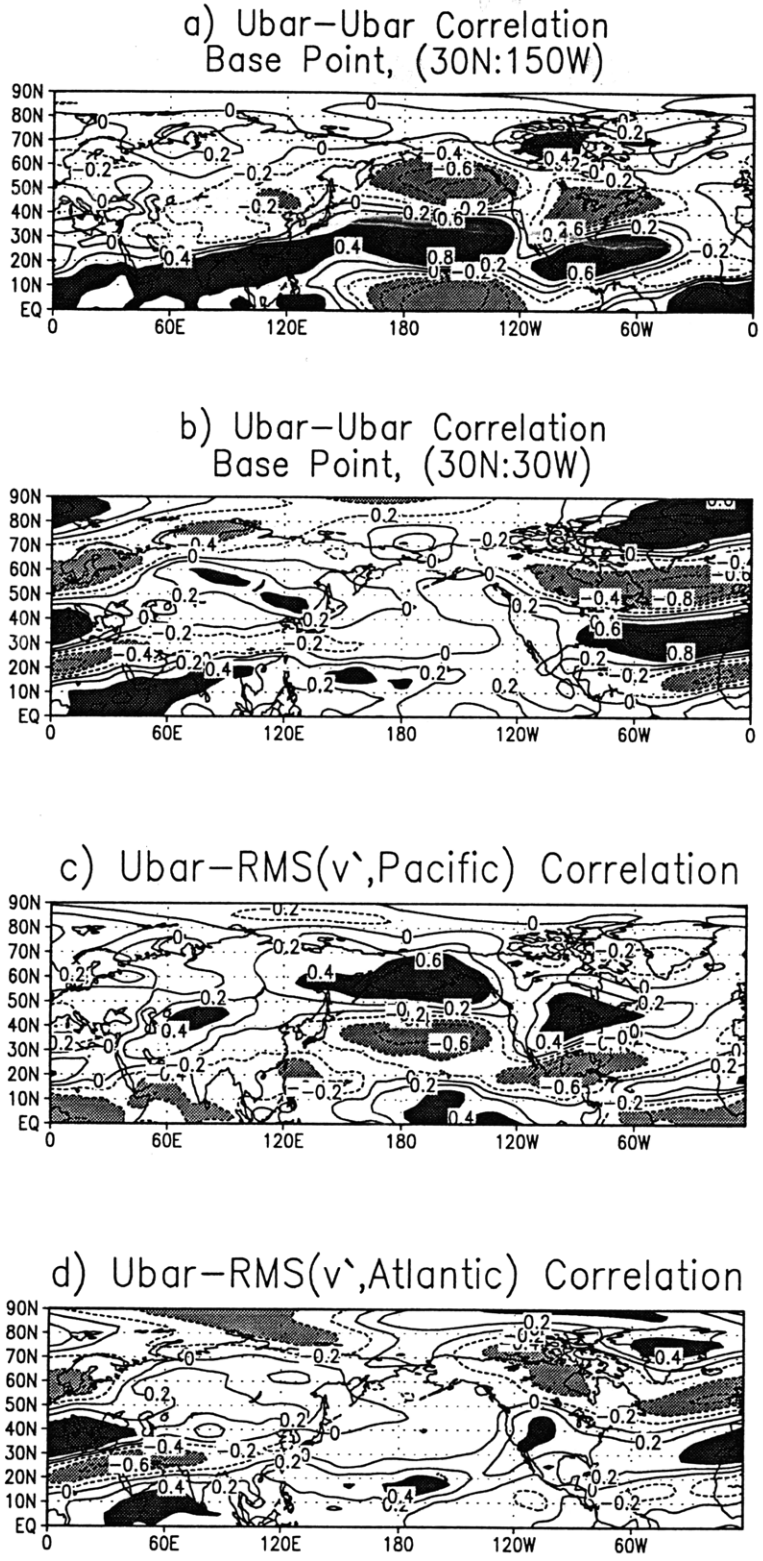

Figure 2-3: a) One-point simultaneous correlation of Ubar, base point (30N:150W). b) Same as a) except for base point (30N:30W). c) Correlation between Ubar and the intensity index of Pacific storm track. d) Correlation between Ubar and the intensity index of Atlantic storm track. The dark and light shades represent positive and negative values. Contour interval 0.2.

cover the Pacific jet region, while cover the jet exit in the Pacific.

b) EOF3 (Fig. 2-2c): The variation of this mode is mainly located in the East Asia and West Pacific, which covers some parts of the Pacific jet.

To construct the one-point correlation maps, we choose 30N:150W and 30N:30W as the base points and compute the correlations between Ubar at each base point and other points, using their 23 seasonal-mean values. Results are shown in Figs. 2-3a and 2-3b. An obvious north-south seesaw can be seen to oscillate around the mid-latitude in the Pacific and Atlantic regions.

For a sample size of 23 seasons, the 90% significance level corresponds to a critical correlation value of 0.36, assuming that 22 anomalies are independent (sum of 23 anomalies is zero). It's difficult to assess the effective number of independent samples which definitely is smaller than 23. In Fig 2-3a, we can see the largest correlation of negative phase is almost the same as the correlation of positive phase around base point, which is higher than 0.8 and suggests the correlation is highly significant. Compare the EOF1 mode (2-2a) and one-point correlation map in the Pacific (2-3a), it's easy to see their patterns are very close. The spatial correlation between them reaches -0.85. In Fig. 2-3b, it's seen that correlations are also very high near the Atlantic. The spatial correlations between Fig. 2-3b and Figs. 2-2b, 2-2d are 0.61 and -0.35 respectively, which suggests that Ubar oscillation in the Atlantic reflects some properties of EOF2 mode. Since upper-level westerlies have a close relation with low-level baroclinicity, we shall turn to see the interannual seesaw of baroclinicity.

2.1.3 Baroclinicity

We apply EOF's to interannual baroclinicity anomalies and get four leading EOF modes as before. Results are shown in Fig. 2-4. In order to see if there exist some relations between the EOF modes of Ubar and baroclinicity, we calculate the spatial correlation between their EOF patterns. It's found the spatial correlation bweteen EOF1 patterns of Ubar and baroclinicity is -0.51 and the correlation between their EOF2 patterns is -0.58. Even these correlation are not very high, it still tends to support our expectation in last subsection. From thermal wind relation, zonal

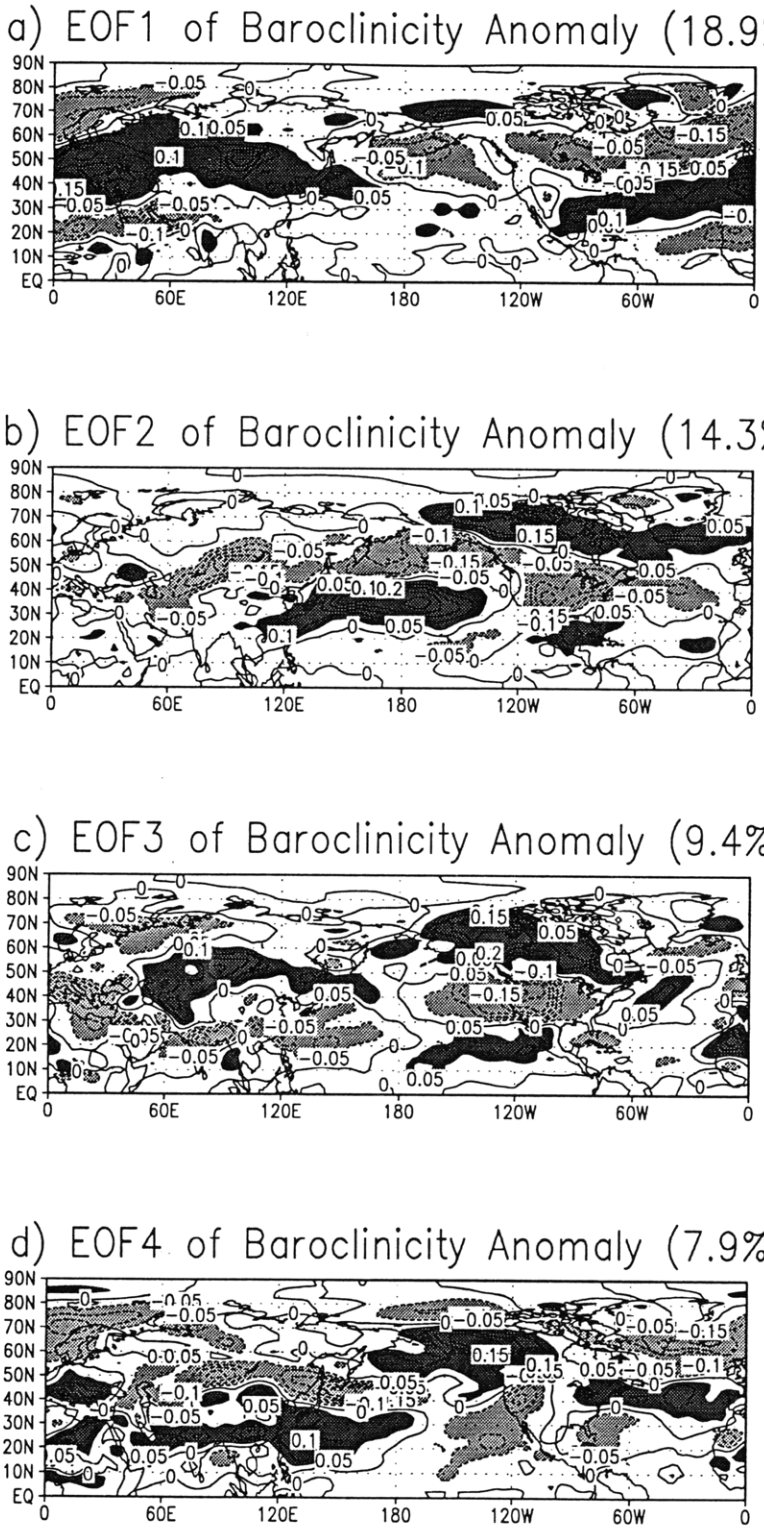

Figure 2-4: Same as Fig. 2-1 except for baroclinicity.

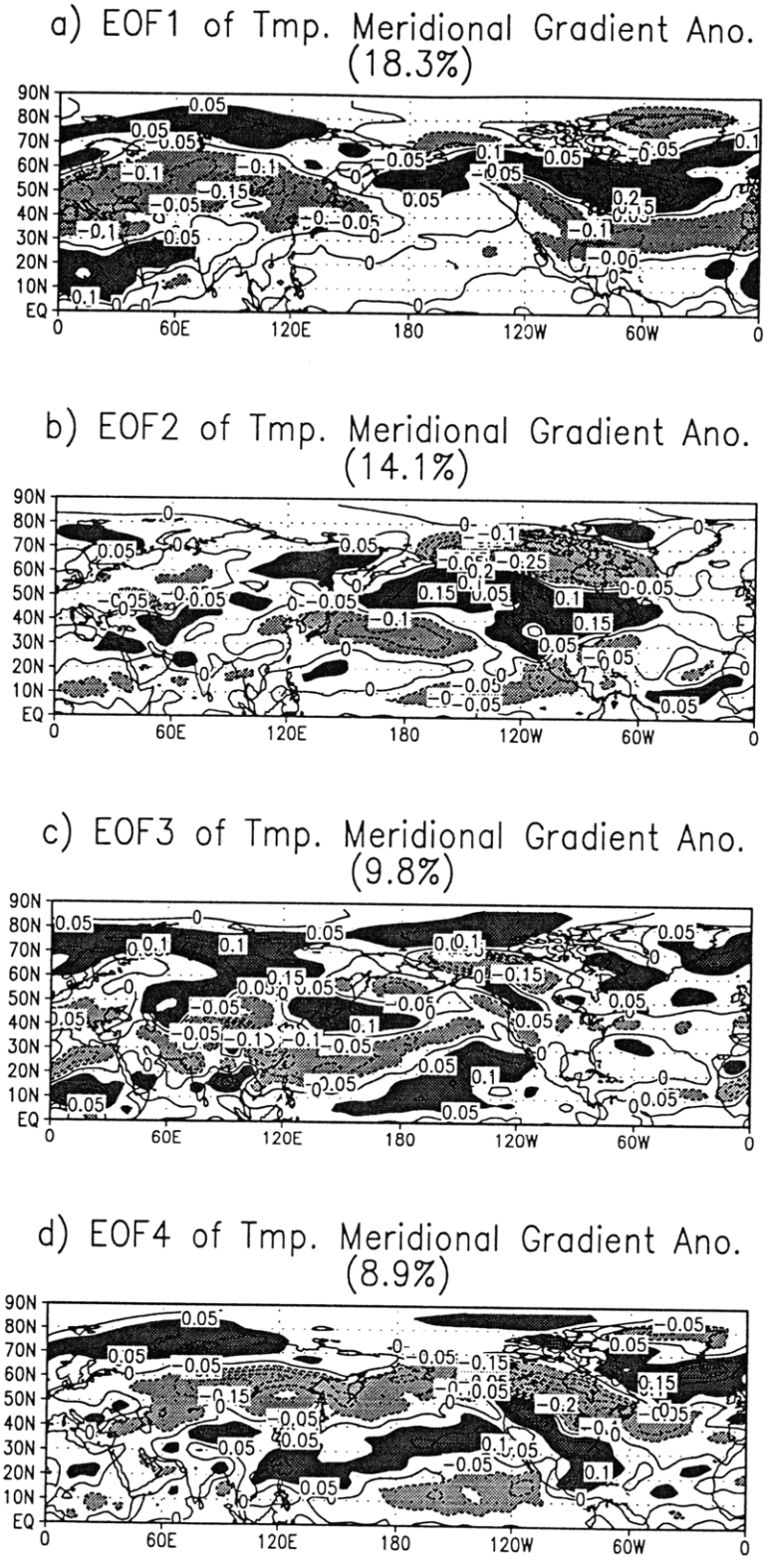

Figure 2-5: Same as Fig. 2-1 except for meridional gradient of temperature

wind shear is determined by the meridional temperature gradient. Hence we also calculate four EOF modes of meridional temperature gradient anomalies at 850 mb and results are shown in Fig. 2-5. Similar patterns can be found there, especially for EOF1 and EOF2. The spatial correlation between EOF1 patterns of baroclinicity and meridional temperature gradient can reach -0.79, and the correlation between their EOF2 patterns is also as high as -0.68. This strongly supports our guess that variation of low-level meridional temperature gradient is the main mechanism accounting for the variation of baroclinicity.

2.2 Pacific storm track

In order to investigate the interannual variability of Pacific storm track, we need to define an index to show its seasonal intensity. From Fig. 1-3, we can see the major part of Pacific storm track is located in the region from 30N to 70N in latitude and 180 to 120W in longitude. The area-averaged value of seasonal RMS(v') in above region will be taken as this index.

Lau (1988) found there is a close relation between storm tracks and monthly circulation pattern. He also pointed out the westerlies flow should contribute to the change of storm tracks. Suppression of the mid-winter Pacific storm track has been well documented by Nakamura (1992). The quick-shift effect of baroclinic eddies by basic flow is suggested to be one possible mechanism for this suppression. Since the time for waves to stay in the strong baroclinic areas will be shorter if they are shifted downstream faster, waves can't have enough time to grow. Thus he argued that quick shift by stronger basic flow could cancel the effect of higher baroclinicity. However, it's not clear if we can also contribute the interannual variability of Pacific storm track to the variation of basic flow.

To show this, we simply correlate the intensity index of Pacific storm track in 23 winters to Ubar in the corresponding winters. Result is shown in Fig. 2-3c and basically it suggests above hypothesis could be true. We can see Ubar-Ubar correlation pattern in Fig. 2-3a has opposite phase to the Ubar-RMS(v', $Pacific$) pattern in Fig.

2-3c which resembles the EOF1 pattern of Ubar (Fig. 2-2a). The spatial correlation between Fig. 2-3c and Fig. 2-2a is as high as 0.79. The correlation between intensity index of Pacific storm track and the temporal coefficients of EOF1 mode of Ubar is 0.58 (>0.36), which suggests that EOF1 mode of Ubar may control the intensity of Pacific storm track. The largest correlations of positive and negative phases in Fig. 2-3c are higher than 0.6 (>0.36) which shows that the correlation is highly significant. It's straight forward to conclude that the Pacific storm track is negatively correlated to the southern side of Ubar seesaw but positively correlated to the northern side of seesaw. Obviously, the Pacific storm track taken into account covers both sides of Ubar seesaw (Fig. 2-3c). The rising question is why the intensity of Pacific storm track is in the same phase with the oscillation of Ubar on the northern side of seesaw while in the opposite phase to the oscillation on the southern side.

2.3 Atlantic storm track

The seasonal intensity indices of the Atlantic storm track are defined to be the area-averaged value of seasonal RMS(v') in the band from 30N to 70N in latitude and 60W to 0 in longitude in 23 winters (1973-1996). The same steps as in last section are taken to correlate above 23 seasonal indices to Ubar in the corresponding winters. Results are shown in Fig. 2-3d. As in the Pacific storm track, the one-point correlation of Ubar-Ubar (Fig. 2-3b) in the Atlantic storm track bears some similarity to the pattern of Ubar-RMS(v', *Atlantic*) correlation, also resembles the patterns of Ubar EOF2 and EOF4 modes. Fig. 2-3d has spatial correlations of 0.54 with Fig. 2-2b and -0.44 with Fig. 2-2d. The correlation between the intensity indices of Atlantic storm track and the temporal coefficients of Ubar EOF2 mode is 0.39, while the correlation between intensity indices and EOF4 mode is -0.43. Both of them are not so high as similar correlations of Pacific storm track. One possible reason for this difference is nonlinear stage of the life cycles of baroclinic waves often occurs in the Atlantic storm track, which thus makes the variation of intensity of Atlantic storm track much more complex than that of Pacific storm track. As in the Pacific storm track, it's not

clear about why the intensity of the Atlantic storm track is in the same phase with the oscillation of Ubar on the southern side of Atlantic seesaw while in the opposite phase to the oscillation on the northern side (see Fig. 2-3d).

Chapter 3

Baroclinic Waves Propagation and Interannual Variability

3.1 Geographical distribution of coherence index

3.1.1 Packet coherence index

We plot packet coherence index (PCI) in Fig. 1-2c and it's seen that the maximum is located in South Asia and North Africa. Other higher values of PCI are distributed in a narrow band around middle latitude. Compared with WCI we will show next, PCI in general describes the schematic wave guide given in CY better. Regions with higher PCI are dedicated by dark colors in Fig. 1-2c and referred to as baroclinic wave guides. Apparently, baroclinic wave guides are different with the band of storm tracks. One important feature is the wave guides are divided into two branches near Asia. They merge together when propagating into the Pacific. This character has been well described in CY, and our 16-winter mean result shows it more clearly.

3.1.2 Wave coherence index

The wave coherence index (WCI), plotted in Fig. 1-1c, reveals two branches of wave guides more clearly than PCI. However, it doesn't show the extension of wave guides across the Atlantic. The difference between PCI and WCI has been discussed in much

detail in CY and won't be repeated here.

3.2 Coherence index change in propagation

3.2.1 Case of packet coherence index

Lee and Held (1993) suggested that coherence of wave packets is inversely related to the baroclinicity of the basic state flow, probably due to the active chaotic baroclinic eddies. Berberry and Vera (1996) also gave such a suggestion in their paper. It was not until recently that wave packets datas are available (in CY) and above hypothesis can be tested. Chang and Yu found the correlation between baroclinicity index and PCI is not negative. In order to investigate how wave packets coherence changes in propagation, we define the relative change of packet coherence index by:

$$[PCI(+2) - PCI(-2)]/[PCI(+2) + PCI(-2)] \tag{3.1}$$

where PCI(+2) is the +2 days downstream packet coherence index and PCI(-2) is the -2 days upstream packet coherence index. This is another index to give the relative change of packet coherence when propagating from upstream region of one certain point to its downstream region. It shows how wave packet coherence changes after passing one position. Thus from Figs. 1-2d and 1-4a we can see the regions where passing wave packets decrease their coherence are located near the areas with high baroclinicity and vice versa. We calculate the spatial correlation between Fig. 1-2d and Fig. 1-4a. The values is -0.2, which is not high but definitely is negative. Basically, this suggests high baroclinicity can reduce coherence of wave packets.

3.2.2 Case of wave coherence index

The relative change of wave coherence index is defined by:

$$[WCI(+2) - WCI(-2)]/[WCI(+2) + WCI(-2)] \tag{3.2}$$

where WCI(+2) is the +2 days downstream wave coherence index and WCI(-2) is the -2 days upstream wave coherence index. Result is plotted in Fig. 1-1d. In the Pacific, Europe, and Asia, it looks similar to the relative change of packet coherence index. But such a similarity isn't obvious in the America and Atlantic. The spatial correlation between Fig. 1-1d and Fig. 1-4a is -0.16 , which also gives hints that high local baroclinicity probably can reduce the coherence of passing waves.

3.3 Group velocity and phase velocity

Statistical group velocity, which is estimated by Chang (1997) by following the movement of timelag correlation center of *ve* from negative lag to positive lag, however, provide no daily information of wave groups propagation. It's of much value both in theory and observation to compute daily group velocity from the original meaning of wave group. The fundamental physics involved in tracking wave groups (deformation allowed) at different time basically depends on the concept of spatial coherence. In other words, if we find a spatial wave packet (around the original wave packet) some time later has a maximum spatial correlation with the original one, then we expect this wave packet must develop from the original packet. The distance between these two wave packets can be determined and used to compute group velocity.

Next we shall apply a technique based on tracking the most spatially coherent *ve* in 12-hour time interval to compute 12-hourly group velocity. First, we construct a base box around each base point. The base box has longitudinal extension of 63 degrees and latitudinal extension of 18 degrees in winter. The size of box is smaller than the size of a typical wave packet so that deformation of wave packets [1] can be captured. Considering the scale of wave packets is a bit smaller in summer than in winter, we choose the longitudinal and latitudinal extensions of base box to be 53 degrees and 18 degrees in summer. These parameters are chosen according to the comparison

[1]The deformation of wave packets obviously is caused by the different group velocities in different parts of wave packets. Take this fact into account, it's reasonable to use a smaller (than the typical scale of wave packets) box so that different group velocities within wave packets can be depicted.

between our calculation (16-season mean of group velocity) and the calculation in CY (statistical group velocity obtained from timelag correlations of ve). We have tried to adjust the parameters to be physically reasonable and make the difference between two calculations to be less. For each base point we construct other reference boxes with the same size around the base box 12 hours later, and then calculate the spatial correlation between the wave packets in base box and that in reference boxes. The zonal and meridional distances between base point and the center of reference box with the highest correlation then can be determined. Divide both distances by the time interval (12 hours) then we get 12-hourly zonal and meridional group velocities. The searching ranges (maximum distance between base box and reference boxes taken into account) in winter and summer are chosen to be different so that group velocities thus abtained are confined to certain realistic values. For example, we don't allow zonal group velocity to be larger than about 120 m/s in winter and 40 m/s in summer. In order to see if this technique works well, the 16-winter mean and 16-summer mean group velocity thus obtained are shown in Figs. 3-1 and 3-2, as well as their streamlines and divergences. Compare them with statistical group velocity obtained using timelag statistics by Chang (1997), we find they are in good agreement except that our zonal group velocities are a bit smaller in jet core regions. The availability of 12-hourly group velocity allows us to give exact calculation of mean growth and decay rate of ve following group velocity.

Similar procedure is taken to compute 12-hourly phase velocity. Here, we use v' data and the size of box (18 longitudinal degrees and 13 latitudinal degrees in both winter and summer) is chosen to be smaller than a typical mid-latitude baroclinic eddy, which allows us to pick up the deformation of synoptic eddies. In Fig. 3-3, zonal and meridional components of phase velocity in winter and summer respectively are shown. Compare them with zonal phase speeds estimated by Chang (1997), we can see they are very close.

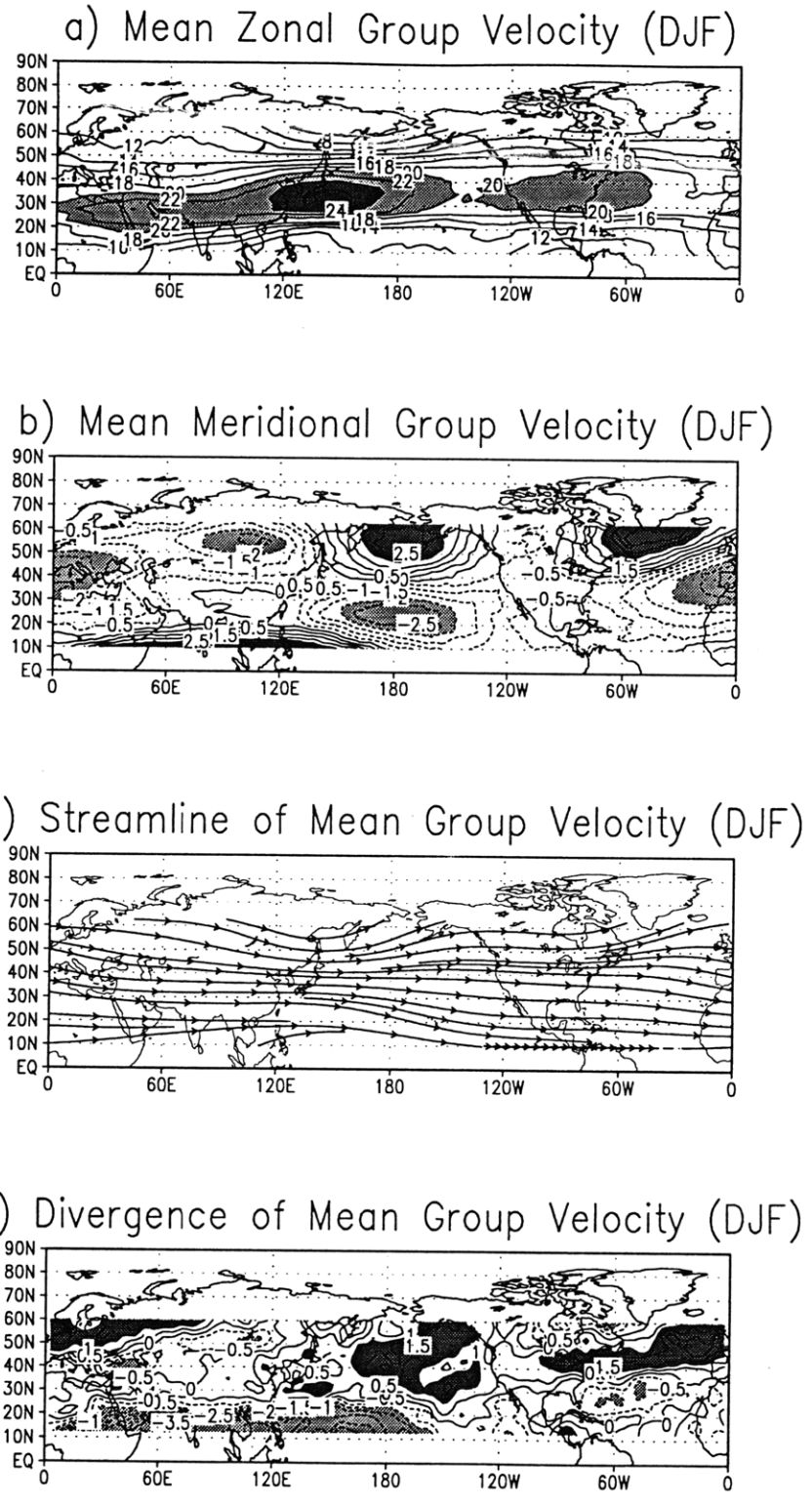

Figure 3-1: a) Mean zonal group velocity, averaged over winters of 1980-1996. b) Mean meridional group velocity in winter. c) Streamline of mean group velocity in winter. d) Divergence of mean group velocity in winter. Contour intervals are 2 ms^{-1} in a), 0.5 ms^{-1} in b), and 0.5 $\times 10^{-6} s^{-1}$ in d). In a), the shades represent values greater than 20 and 24. In b) and d), the shades represent positive and negative values respectively.

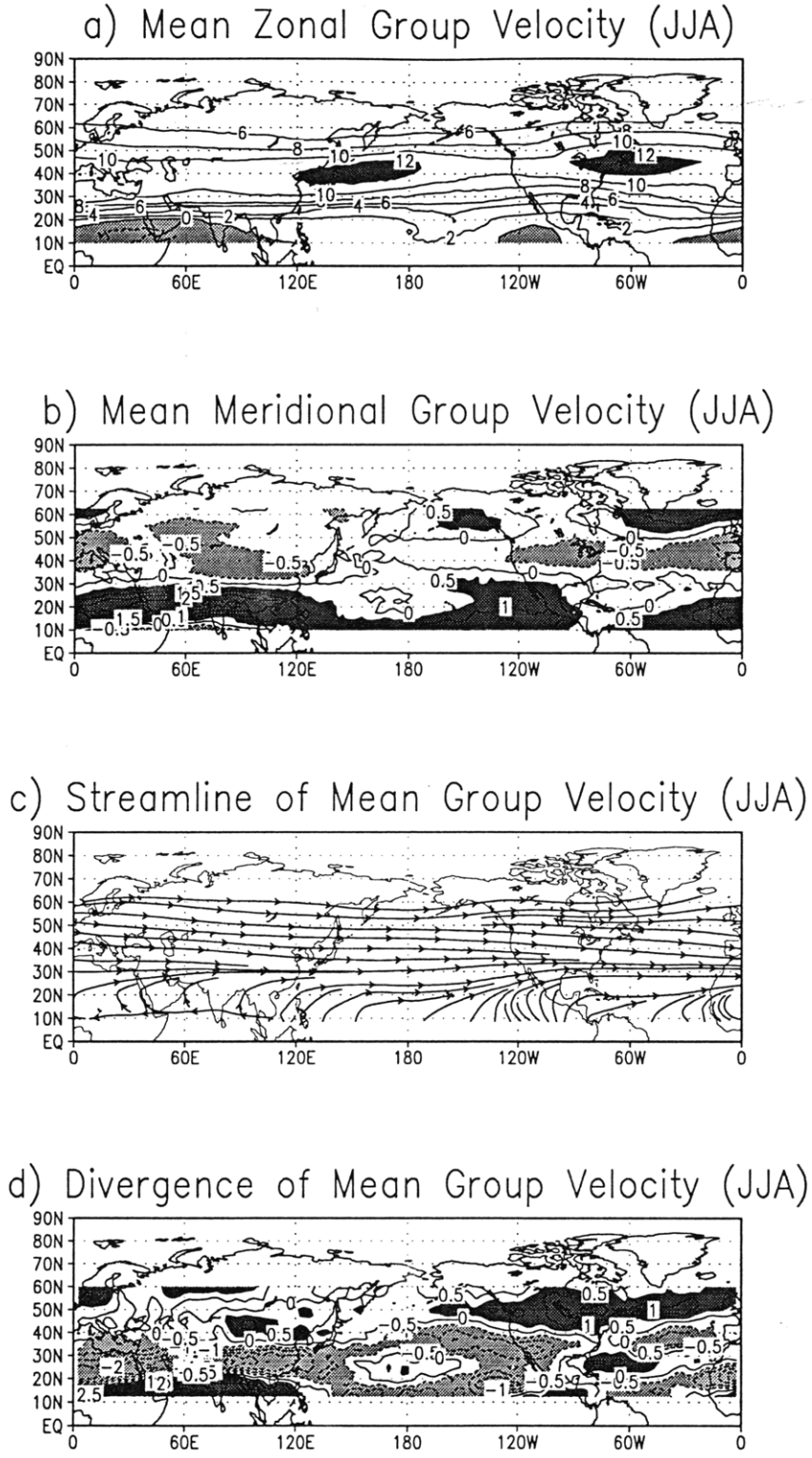

Figure 3-2: a) Mean zonal group velocity, averaged over summers of 1980-1995. b) Mean meridional group velocity in summer. c) Streamline of mean group velocity in summer. d) Divergence of mean group velocity in summer. Contour intervals are 2 ms^{-1} in a), 0.5 ms^{-1} in b), and 0.5 $\times 10^{-6} s^{-1}$ in d). In a), the shades represent values greater than 12 and less than than 0. In b) and d), the shades represent positive and negative values respectively.

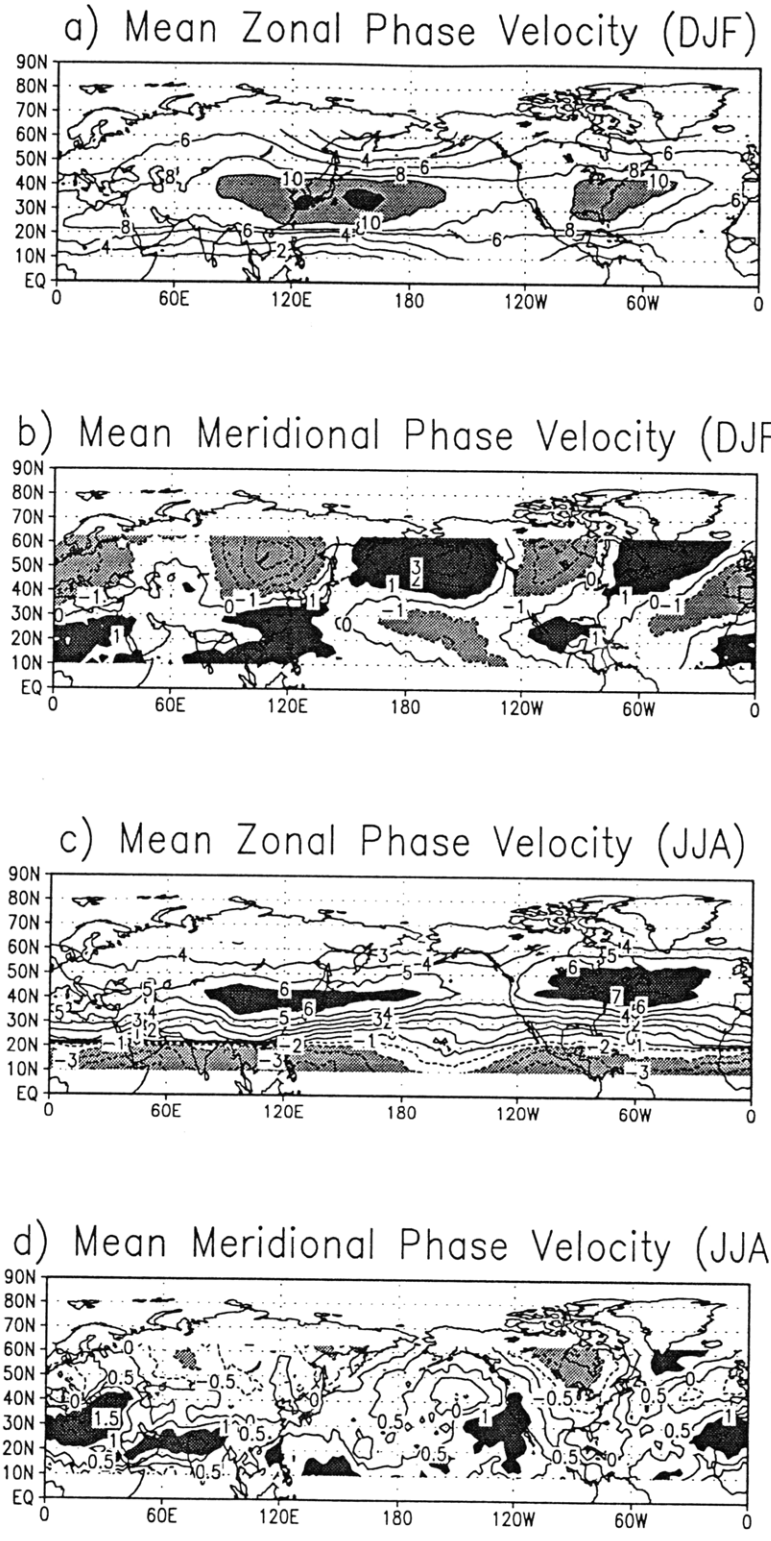

Figure 3-3: a) Mean zonal phase velocity, averaged over winters of 1980-1996. b) Mean meridional phase velocity in winter. c) Mean zonal phase velocity, averaged over summers of 1980-1995. d) Mean meridional phase velocity in summer. Contour intervals are 2 ms^{-1} in a), 1 ms^{-1} in b) and c), and 0.5 ms^{-1} in d). In a), the shades represent values greater than 10 and 12. In b), c) and d), the shades represent positive and negative values.

3.4 Growth and decay rate of amplitude of packets following group velocity

In order to document the geographical distribution of growth and decay rate of ve at 300 mb following $\vec{Cg}$, we use 12-hourly group velocity previously obtained and compute growth (decay) rate according to below formulas:

$$\frac{d_g ve}{dt} = \frac{\partial ve}{\partial t} + Cgx\frac{\partial ve}{\partial x} + Cgy\frac{\partial ve}{\partial y} \tag{3.3}$$

and

$$\overline{\frac{d_g ve}{dt}} = \overline{\frac{\partial ve}{\partial t}} + \overline{Cgx\frac{\partial ve}{\partial x}} + \overline{Cgy\frac{\partial ve}{\partial y}} = \overline{Cgx\frac{\partial ve}{\partial x}} + \overline{Cgy\frac{\partial ve}{\partial y}} \tag{3.4}$$

where bar represents time mean. Obviously, the time mean of $\frac{\partial ve}{\partial t}$ is zero.

3.4.1 Northern Hemisphere winter

The 16-winter mean growth and decay rate of ve following $\vec{Cg}$ is shown in Fig. 3-4a. The most prominent feature is the region of high growth rate in the Northeastern Asia and West Pacific. This is what we expect since it's close to the region of the highest baroclinicity (see Fig. 1-4a). Compare Figs. 1-4a and 3-4a, we find that the West Pacific of high baroclinicity can be divided into two parts along latitude 30. The northern part corresponds to strong growth and the southern part corresponds to decay. What causes this difference isn't clear to us. Complete answer to this question need to consider the vertically-integrated wave energy and find if it's also true for the whole layer of atmosphere, provided that calculation of only one level could miss the energy transfer between different levels. By tracking the upstream and downstream center on the -1 day and +1 day 500 hpa lag-correlation maps, Wallace et al. computed the difference between downstream and upstream regression coefficients, which provides a measure of growth and decay rates following phase velocity (see their Fig. 10). We can see the growth regions in their figure are mainly located in the East Asia, North America and the European part of former Soviet

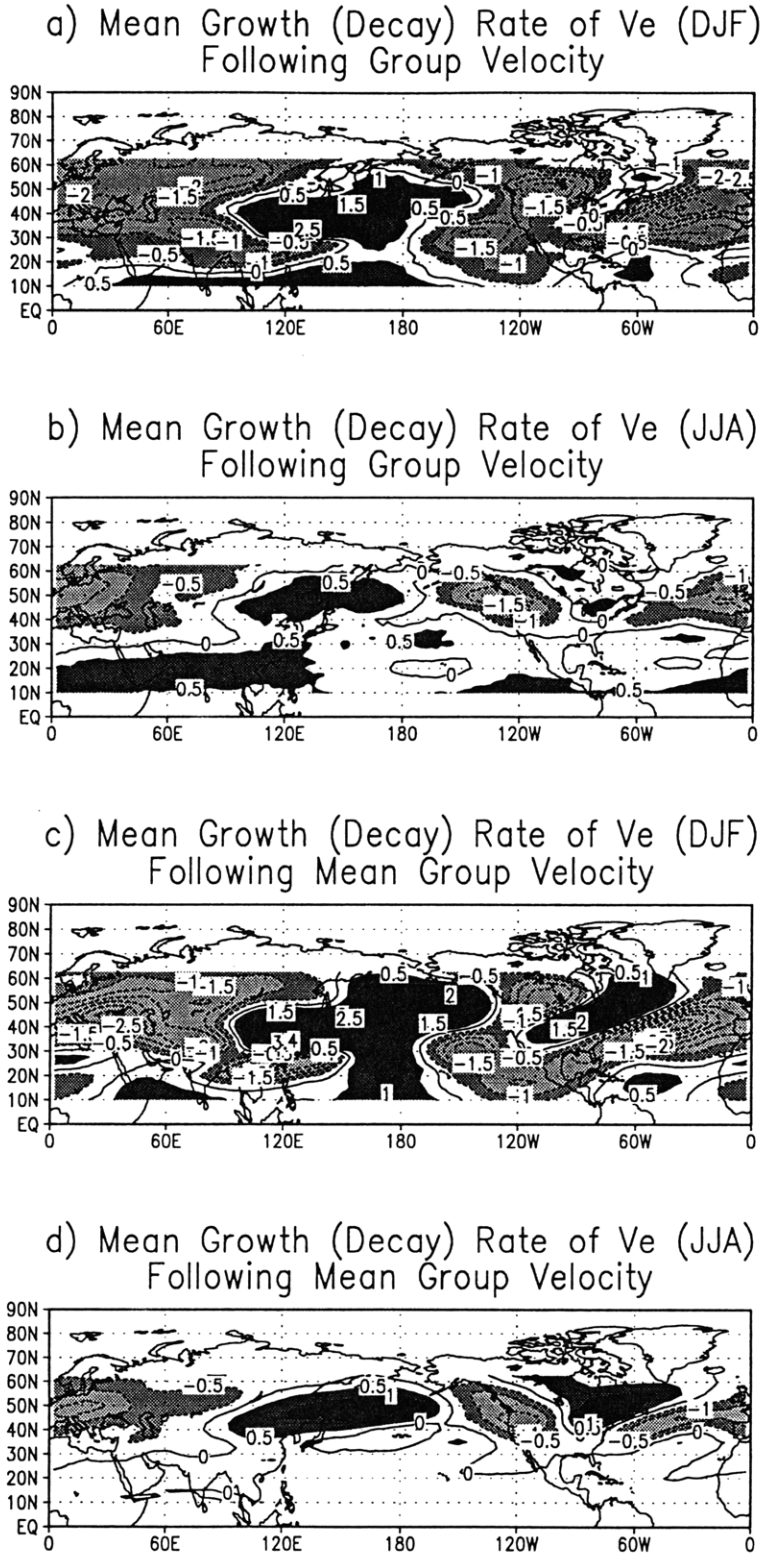

Figure 3-4: a) Mean growth (decay) rate of *ve* following group velocity, averaged over winters of 1980-1996. b) Same as a) except averaged over summers of 1980-1995. c) Same as a) except for following mean group velocity. d) Same as b) except for following mean group velocity. Contour interval 0.5 $\times 10^{-5} ms^{-2}$. The dark shades represent values greater than 0.5 and 1, while light shades represent values less than -0.5 and -1.

Union. In the North Pacific and North Atlantic, their result shows a prominent decay. Obviously, daily information of waves propagation isn't involved in their estimation which thus is fairly rough. As will be demonstrated next, growth and decay rates following group velocity and mean group velocity are impressive different. Compared with their calculation, out result depicts the growth of wave packets following group velocity in the Northeastern Pacific and decay in the Europe and main parts of North America.

The other phenomenon of interest is the observed growth rate in the Northeastern Pacific with fairly low baroclinicity. Even we need to consider the interaction between different levels, it still seems reasonable to relate it with the oceanic cyclones which basically are found to depend on the latent heat, rather than dry baroclinicity.

The oceanic explosive cyclones have been well documented in the recent 20 years by, e.g., Sanders and Gyakum (1980), Roebber (1984) and Murty et al (1983). This kind of explosive cyclones often occur in the Northeastern Pacific and Western Atlantic and are called bombs. Chang et al (1982) and Gall (1976) showed that released latent heat contribute more to the development of bombs compared with the effect of pure baroclinic instability. Hence we believe storm tracks in Northern Hemisphere winter partly are due to the latent heat released in the Northeastern Pacific.

We also plot:

$$\overline{\overline{Cgx}\frac{\partial ve}{\partial x} + \overline{Cgy}\frac{\partial ve}{\partial y}} = \overline{\overline{Cgx}\frac{\overline{\partial ve}}{\partial x} + \overline{Cgy}\frac{\overline{\partial ve}}{\partial y}}$$

in winter in Fig. 3-4c. The differences between Figs. 3-4a and 3-4c are shown below.

a) The growth rate in Fig. 3-4c is much larger than that in Fig. 3-4a. However, the difference between their decay rates is small.

b) The growth of eddies in the baroclinic regions of West America and North Atlantic is very impressive in Fig. 3-4c, while not in Fig. 3-4a.

c) The growth regions in Fig. 3-4c extend from the middle Pacific to the tropics without break, while there is an obvious break between the growth region near jet core and the growth region in the tropics.

3.4.2 Northern Hemisphere summer

The 16-summer mean growth and decay rate of *ve* following $\vec{Cg}$ is plotted in Fig. 3-4b. The main growth regions which are located in the Northeastern Asia and the subtropics between Asia and Africa, are downstream of baroclinic areas (see Fig. 1-4b). And the obvious decay in the Northeastern Pacific and Northwestern America seems to be due to low baroclinicity there. The growth and decay rate of *ve* following mean group velocity is displayed in Fig. 3-4d for comparison. The growth in Fig. 3-4d is stronger than in Fig. 3-4b. However, Fig. 3-4d fails to pick up the growth in the subtropics of Asia and Africa. Thus we can see the 12-hourly group velocity does provide some information which is missed in the calculation of growth and decay rate of *ve* using mean group velocity.

3.5 Interannual variability of baroclinic waves propagation

3.5.1 EOF analysis and composite charts constructed according to EOF modes

Next we shall examine the variability of baroclinic waves propagation. The seasonal downstream, upstream indexes and PCI (not shown here) are noisy except that a maximum in South Asia is always observed. And similar noise can be found in the interannual variation of WCI. The question is whether the interannual variability of baroclinic waves propagation has certain relations with the variations of storm tracks and basic states. In order to investigate these possibilities, we shall apply EOF's as before to the 23 interannual anomalies of PCI and WCI. First, four EOF leading modes of PCI interannual anomalies are given in Fig. 3-5, which occupy about 42% of the total variance. Then the typical scenarios for EOF modes of PCI described above are depicted using composite charts. In constructing composite charts for the positive phase of a given EOF mode, the time series of coefficients were ranked according to

the magnitudes. Those four years with the largest positive temporal coefficients were then identified , and the PCI was averaged over these years to form a composite field, hereafter referred to as high composite. Conversely, the negative phase of EOF mode is portrayed by averaging over those years with the largest negative coefficients, and referred to as low composite. The high and low composite charts for four leading EOF modes of PCI are shown in Figs. 3-6 and 3-7, which reveals below characteristics:

a) EOF1 (Fig. 3-5a) shows a prominent variability in the whole body of baroclinic wave guides. High composite chart plotted in Fig. 3-6a depicts the higher coherence in the whole baroclinic wave guides and Alaska. Low composite chart plotted in Fig. 3-6b reveals the decrease of PCI in above regions and increase in eastern tropical Pacific.

b) EOF2 (Fig. 3-5b) mainly depicts the interannual oscillation between southern branch and northern branch , as well as the variation in low-latitude Pacific. From Fig. 3-6c, we can see high composite chart reveals the intensification of southern branch while the collapse of northern branch. The low composite chart plotted in Fig. 3-6d, reveals the opposite tendency and an impressive coherent band in the tropical Pacific.

c) In high composite chart of EOF3 (Fig. 3-7a), we can't distinguish two branches of wave guides. Contrary to this, low composite chart of EOF3 (Fig. 3-7b) shows the two-branch structure clearly. Furthermore, the whole wave guides in high composite chart shift toward the low-latitude regions.

d) EOF4 mode (Figs. 3-5d, 3-7c and 3-7d) portrays a much more uniform zonal extension of PCI along the middle latitude. The difference between PCI in the most coherent region and that in other coherent regions is lower compared with other modes.

Secondly, we display four leading EOF modes of WCI in Fig. 3-8 and composite charts in Figs. 3-9 and 3-10. Below characteristics are revealed.

a) EOF1 (Fig. 3-8a) of WCI is similar to EOF1 of PCI, which shows an interannual variation occurring in the whole body of baroclinic wave guides. Composite charts in Fig. 3-9 tell us about this more clearly. High composite chart represents a more

prominent two-branch structure and vice versa for low composite chart.

b) EOF2 (Fig. 3-8b) of WCI depicts the oscillation between two branches. In addition, it describes an oscillation of wave guides from middle latitudes near the Atlantic to ambient latitudes.

c) EOF3 (Fig. 3-8c) of WCI reveals the variation mainly occurring in low and high latitude.

d) EOF4 (Fig. 3-8d) of WCI shows there is another oscillation between two branches in Asia.

Also, we display four leading EOF modes of IPV meridional gradient anomalies in Fig. 3-11. It seems none of them has similar pattern to the EOF modes of PCI and WCI shown above. As we have analyzed in last chapter, the interannual variability of storm tracks could be controlled by the basic state flow and baroclinicity. On the other hand, downstream development has been shown to be important in the extension of storm tracks by Chang and Orlanski (1993). Thus it is of great interest to investigate the role of WCI and PCI on the intensity variations of storm tracks, especially for comparison with the role of basic state flow and baroclinic instability.

To show this, we simply correlate temporal coefficients of first two leading EOF modes of interannual anomalies of Ubar, baroclinicity, WCI and PCI to 23 seasonal RMS(v') fields. Results are shown in Figs. 3-12 and 3-13. In Figs. 3-12a and 3-12d, we can see the correlations between Ubar EOF1, baroclinicity EOF2 and RMS(v') resemble the EOF1 mode of RMS(v') anomalies (Fig. 2-1a). The spatial correlations between Figs. 3-12a, d and Fig. 2-1a are 0.83 and -0.78 respectively. The correlation between temporal coefficients of Ubar EOF1 and RMS(v') EOF1 is as high as 0.81, and similar correlation between EOF2 of baroclinicity and EOF1 of RMS(v') is -0.69. Basically this suggests that Ubar and baroclinicity may have high relation with the most important mode of interannual variability of storm tracks. We also compute correlations between all patterns in Fig. 3-13 and that in Fig. 2-1 and find below correlations are fairly high.

a) Spatial correlation between Fig. 3-13a and Fig. 2-1d: 0.77. Correlation between temporal coefficients of WCI EOF1 and RMS(v') EOF4: 0.66.

a) Temporal Coefficients of EOF1 of PCI, Winters (1973-96)

Winter	7374	7475	7576	7677	7778	7879	7980	8081
Coefficient	-4.13	3.47	-0.53	-4.14	1.03	-1.30	-0.84	4.20
Winter	8182	8283	8384	8485	8586	8687	8788	8889
Coefficient	0.42	1.92	-2.75	-2.85	0.50	0.76	2.87	5.24
Winter	8990	9091	9192	9293	9394	9495	9596	
Coefficient	0.38	-2.67	3.06	-1.39	-0.79	-0.52	-1.93	

b) Temporal Coefficients of EOF2 of PCI, Winters (1973-96)

Winter	7374	7475	7576	7677	7778	7879	7980	8081
Coefficient	-0.67	-3.16	1.96	2.73	-1.81	0.99	-6.73	2.03
Winter	8182	8283	8384	8485	8586	8687	8788	8889
Coefficient	-0.04	1.01	1.14	1.07	0.44	-0.45	-1.30	0.91
Winter	8990	9091	9192	9293	9394	9495	9596	
Coefficient	-4.47	-2.31	4.11	0.83	2.10	1.24	0.38	

c) Temporal Coefficients of EOF3 of PCI, Winters (1973-96)

Winter	7374	7475	7576	7677	7778	7879	7980	8081
Coefficient	1.14	4.18	-3.96	1.05	-1.03	1.16	0.06	-1.01
Winter	8182	8283	8384	8485	8586	8687	8788	8889
Coefficient	4.60	-0.21	1.10	-0.73	0.86	1.37	0.61	-1.97
Winter	8990	9091	9192	9293	9394	9495	9596	
Coefficient	-4.39	0.32	0.56	1.00	1.52	-2.06	-4.19	

d) Temporal Coefficients of EOF4 of PCI, Winters (1973-96)

Winter	7374	7475	7576	7677	7778	7879	7980	8081
Coefficient	1.76	0.54	1.42	-1.29	-1.21	-1.98	-1.84	-1.94
Winter	8182	8283	8384	8485	8586	8687	8788	8889
Coefficient	2.30	1.01	-0.58	2.03	-3.04	-1.08	-0.10	1.61
Winter	8990	9091	9192	9293	9394	9495	9596	
Coefficient	2.22	-1.04	-0.81	4.21	-1.26	2.50	-3.43	

Table 3.1: a) Temporal Coefficients of EOF1 of PCI. b) Same as a) except for EOF2 of PCI. c) Same as a) except for EOF3 of PCI. d) Same as a) except for EOF4 of PCI.

a) Temporal Coefficients of EOF1 of WCI, Winters (1973-96)

Winter	7374	7475	7576	7677	7778	7879	7980	8081
Coefficient	1.84	-1.51	-1.29	-0.78	2.00	-2.55	-2.15	1.66
Winter	8182	8283	8384	8485	8586	8687	8788	8889
Coefficient	0.74	3.18	-1.56	-0.93	2.14	1.64	1.58	1.20
Winter	8990	9091	9192	9293	9394	9495	9596	
Coefficient	-2.86	-1.32	0.00	-1.03	6.67	-2.78	-3.90	

b) Temporal Coefficients of EOF2 of WCI, Winters (1973-96)

Winter	7374	7475	7576	7677	7778	7879	7980	8081
Coefficient	-0.50	-3.70	-0.39	-1.85	-0.43	-1.01	0.47	1.29
Winter	8182	8283	8384	8485	8586	8687	8788	8889
Coefficient	-2.43	4.53	1.25	-1.86	-0.54	-2.74	1.15	1.51
Winter	8990	9091	9192	9293	9394	9495	9596	
Coefficient	-0.36	1.68	1.46	4.21	-2.81	2.57	-2.51	

c) Temporal Coefficients of EOF3 of WCI, Winters (1973-96)

Winter	7374	7475	7576	7677	7778	7879	7980	8081
Coefficient	1.95	-2.70	-2.71	4.48	1.74	2.93	0.05	-1.48
Winter	8182	8283	8384	8485	8586	8687	8788	8889
Coefficient	-0.77	2.29	-0.86	-0.60	-0.59	-0.57	-3.24	-1.03
Winter	8990	9091	9192	9293	9394	9495	9596	
Coefficient	0.98	0.11	-1.09	0.54	0.56	-1.17	1.18	

d) Temporal Coefficients of EOF4 of WCI, Winters (1973-96)

Winter	7374	7475	7576	7677	7778	7879	7980	8081
Coefficient	0.14	0.29	3.34	-2.69	0.70	1.00	2.22	-0.44
Winter	8182	8283	8384	8485	8586	8687	8788	8889
Coefficient	-3.00	1.68	-1.14	-2.00	-1.69	0.50	0.12	1.42
Winter	8990	9091	9192	9293	9394	9495	9596	
Coefficient	1.85	-0.45	-3.23	-0.58	1.56	-1.36	1.76	

Table 3.2: a) Temporal Coefficients of EOF1 of WCI. b) Same as a) except for EOF2 of WCI. c) Same as a) except for EOF3 of WCI. d) Same as a) except for EOF4 of WCI.

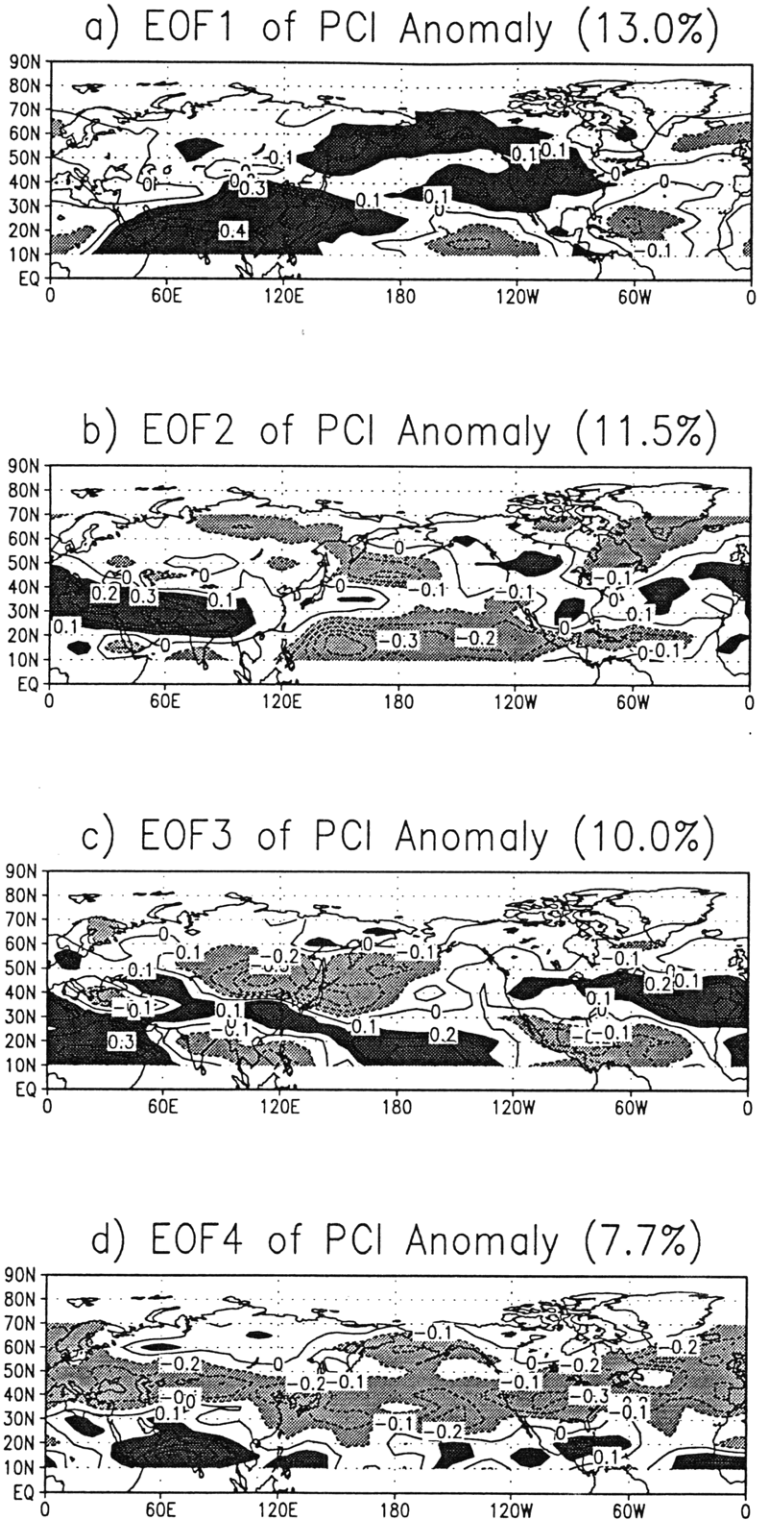

Figure 3-5: Same as Fig. 2-1 except for PCI

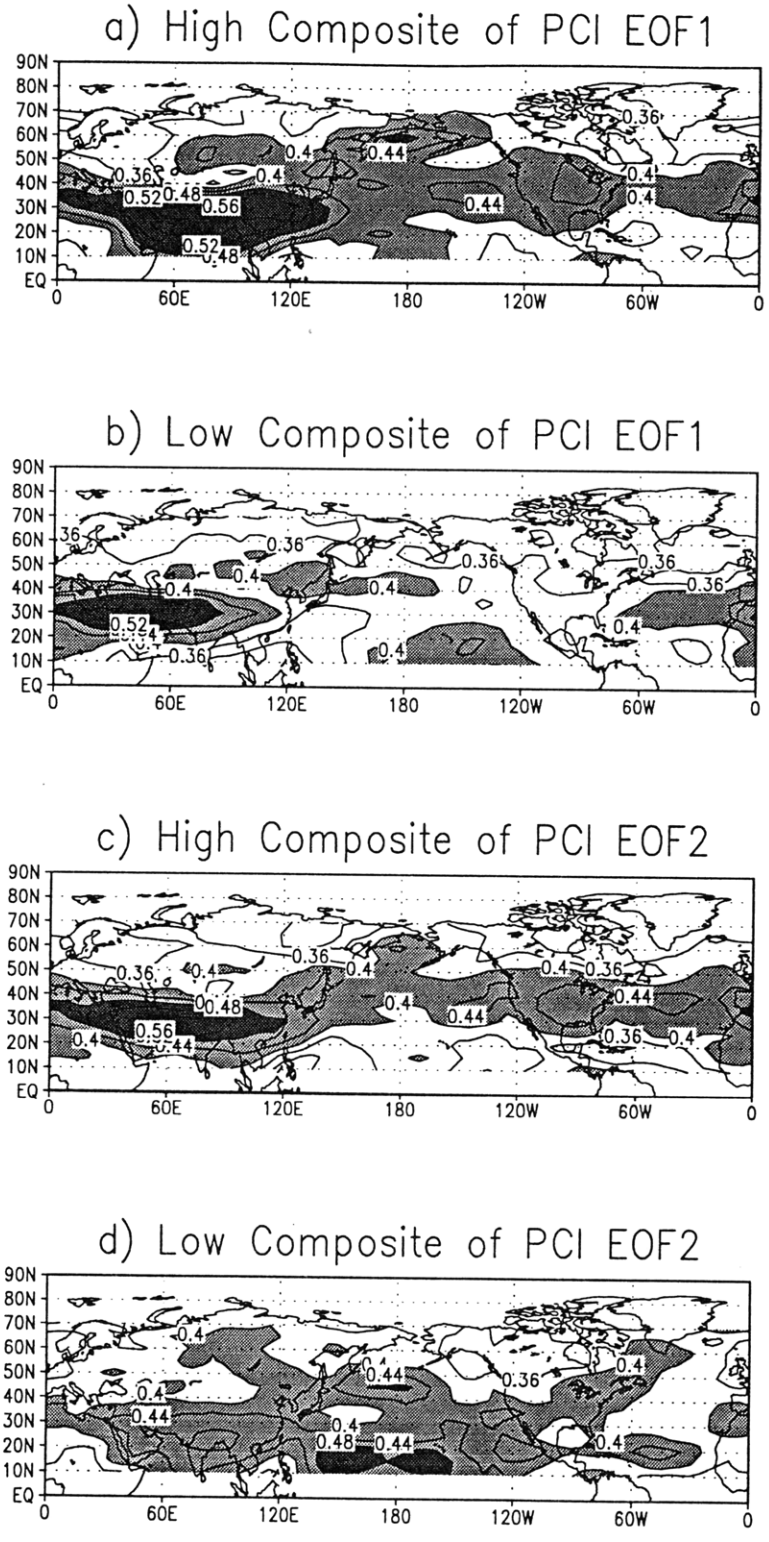

Figure 3-6: a) High composite of PCI EOF1. b) Low composite of PCI EOF1. c) High composite of PCI EOF2. d) Low composite of PCI EOF2. Contour interval 0.4. The different shades represent values greater than 0.4 and 0.48 respectively.

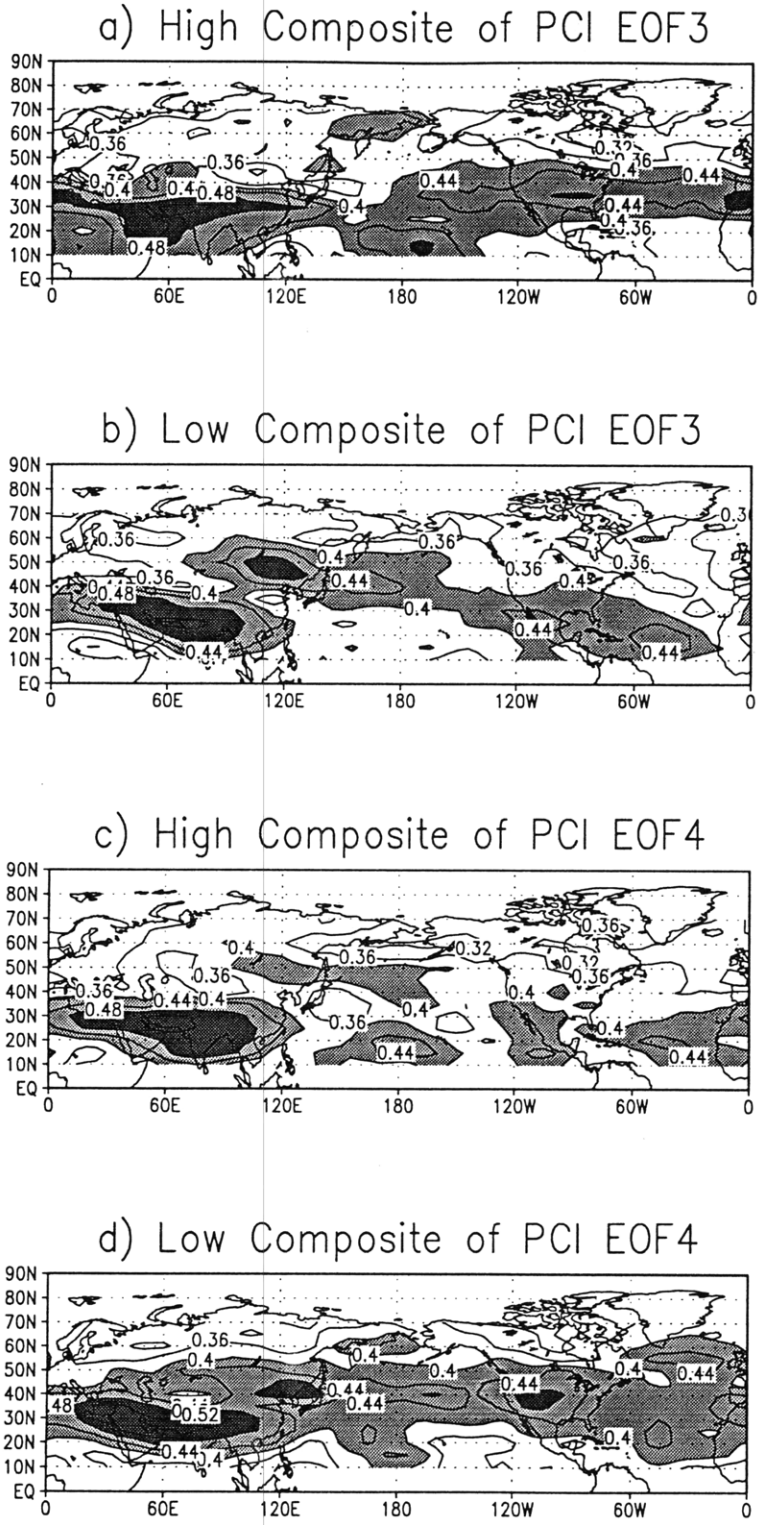

Figure 3-7: a) High composite of PCI EOF3. b) Low composite of PCI EOF3. c) High composite of PCI EOF4. d) Low composite of PCI EOF4. Contour interval 0.4. The different shades represent values greater than 0.4 and 0.48 respectively.

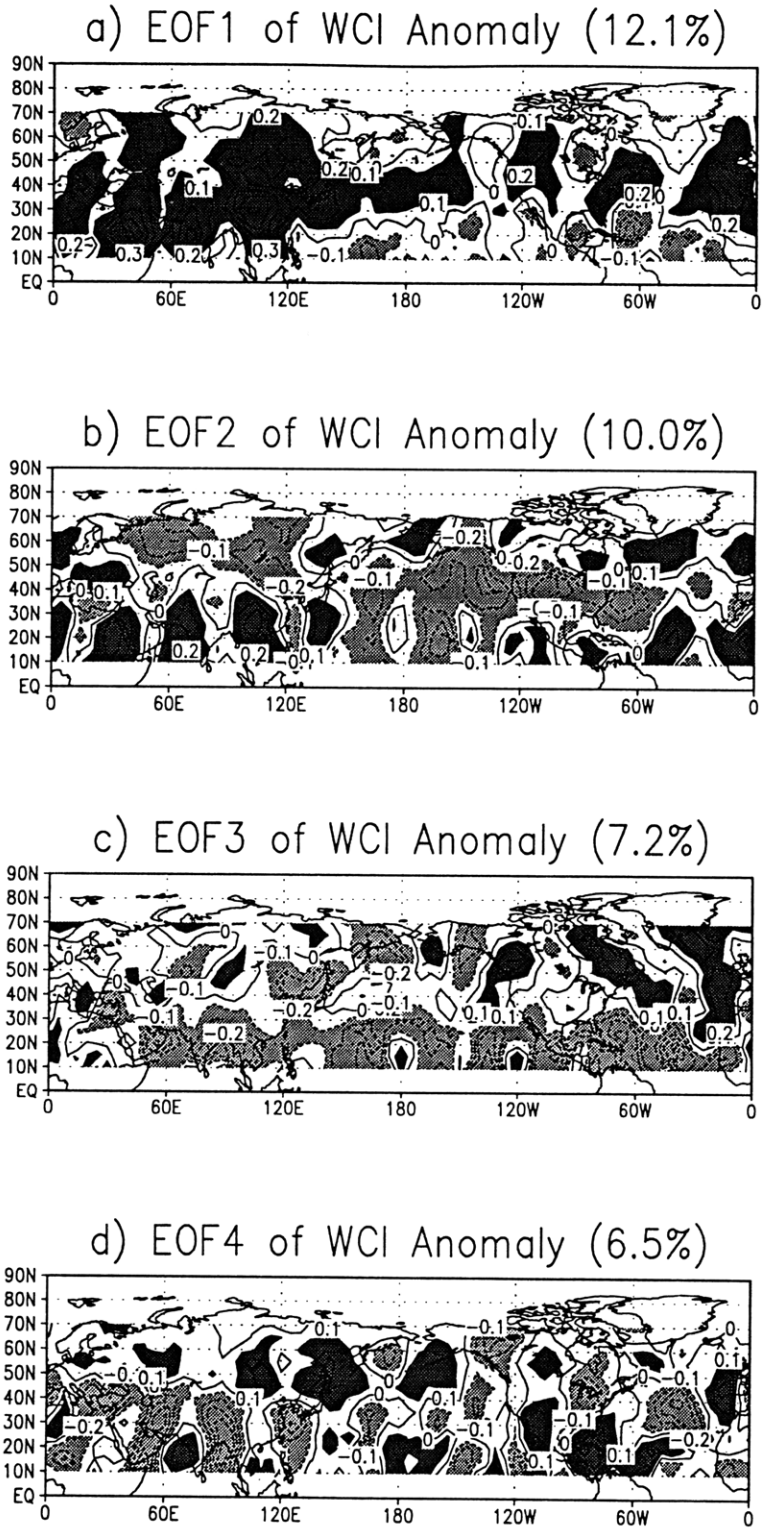

Figure 3-8: Same as Fig. 2-1 except for WCI

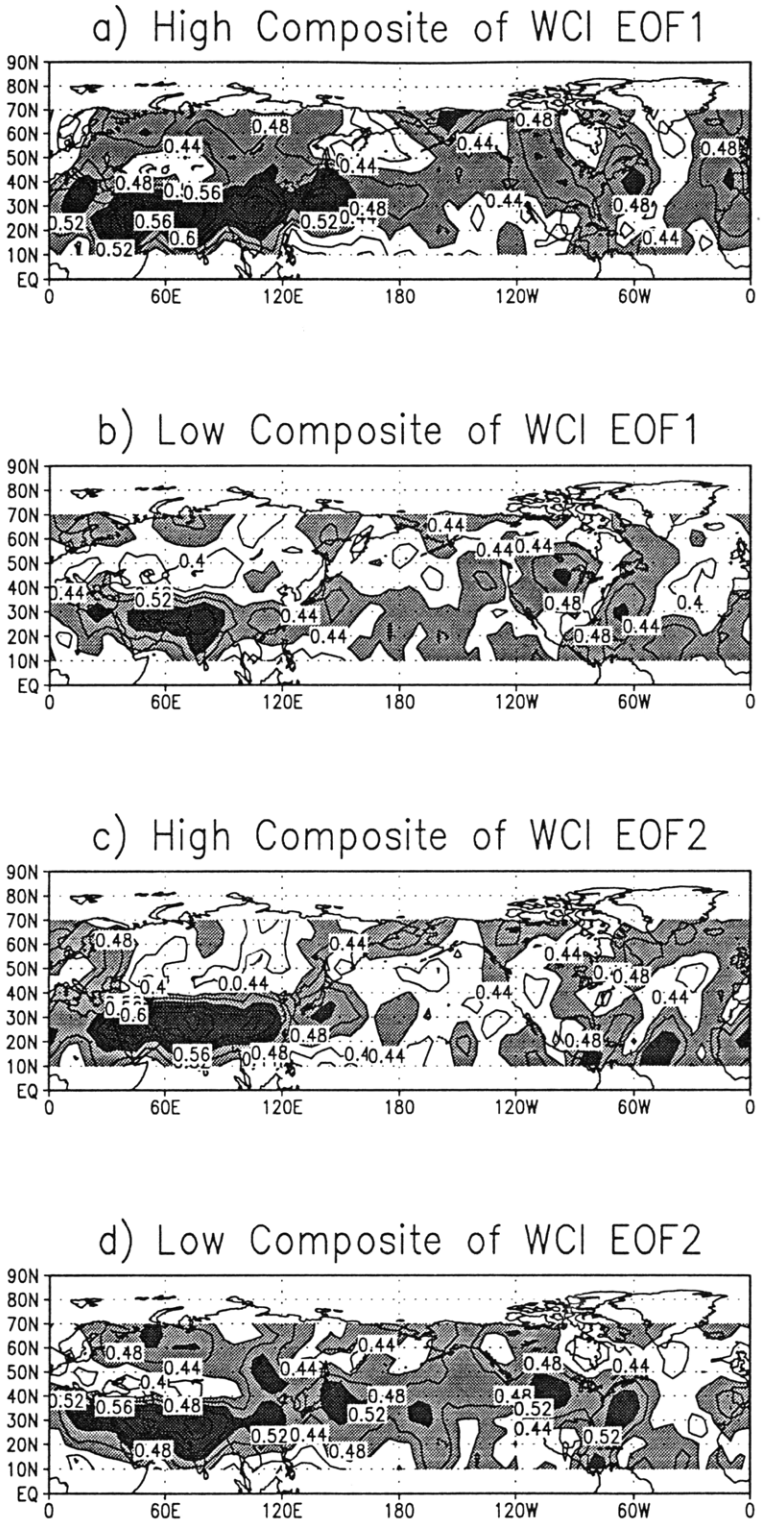

Figure 3-9: a) High composite of WCI EOF1. b) Low composite of WCI EOF1. c) High composite of WCI EOF2. d) Low composite of WCI EOF2. Contour interval 0.4. The different shades represent values greater than 0.44 and 0.52 respectively.

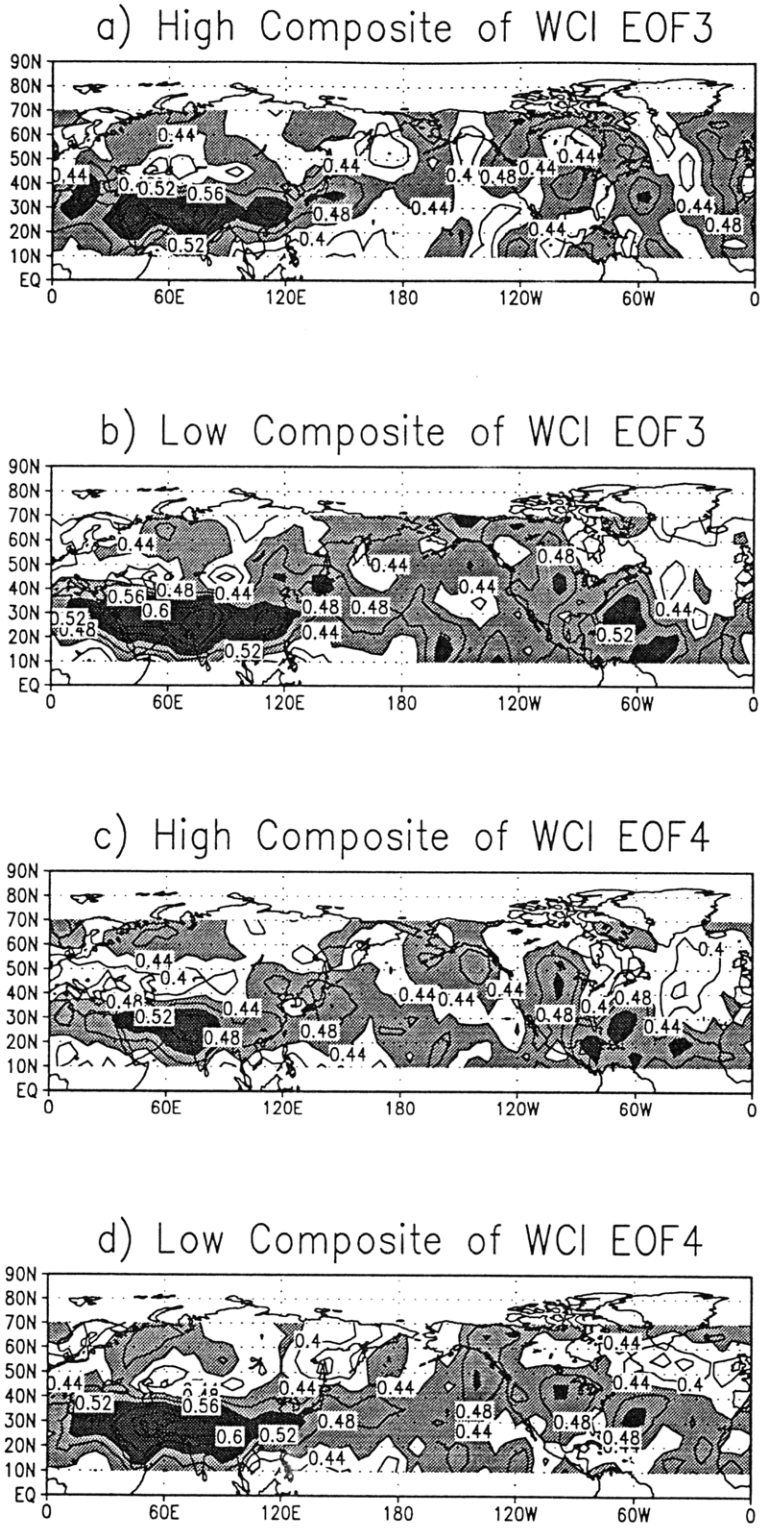

Figure 3-10: a) High composite of WCI EOF3. b) Low composite of WCI EOF3. c) High composite of WCI EOF4. d) Low composite of WCI EOF4. Contour interval 0.4. The different shades represent values greater than 0.44 and 0.52 respectively.

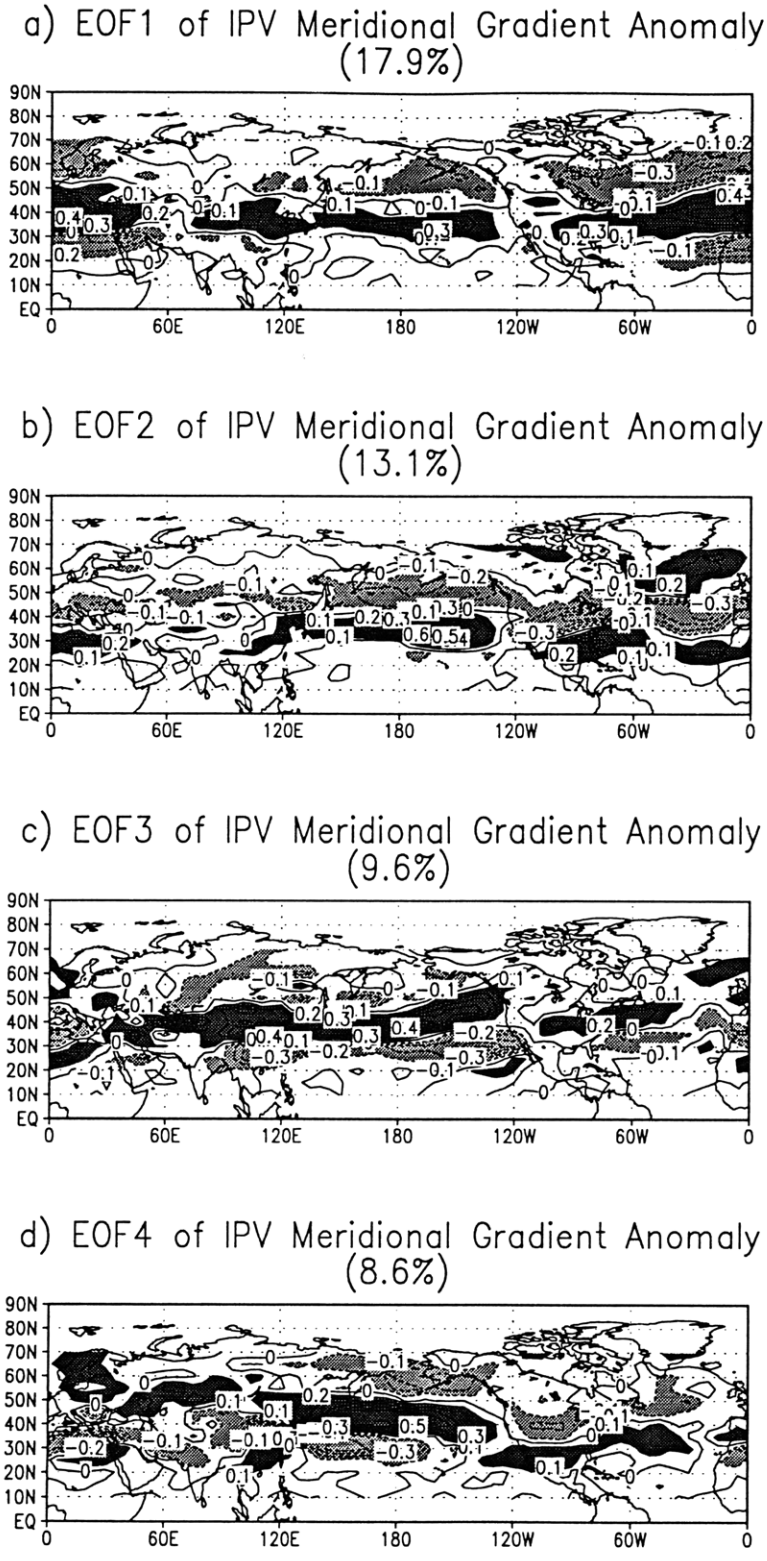

Figure 3-11: Same as Fig. 2-1 except for meridional gradient of IPV.

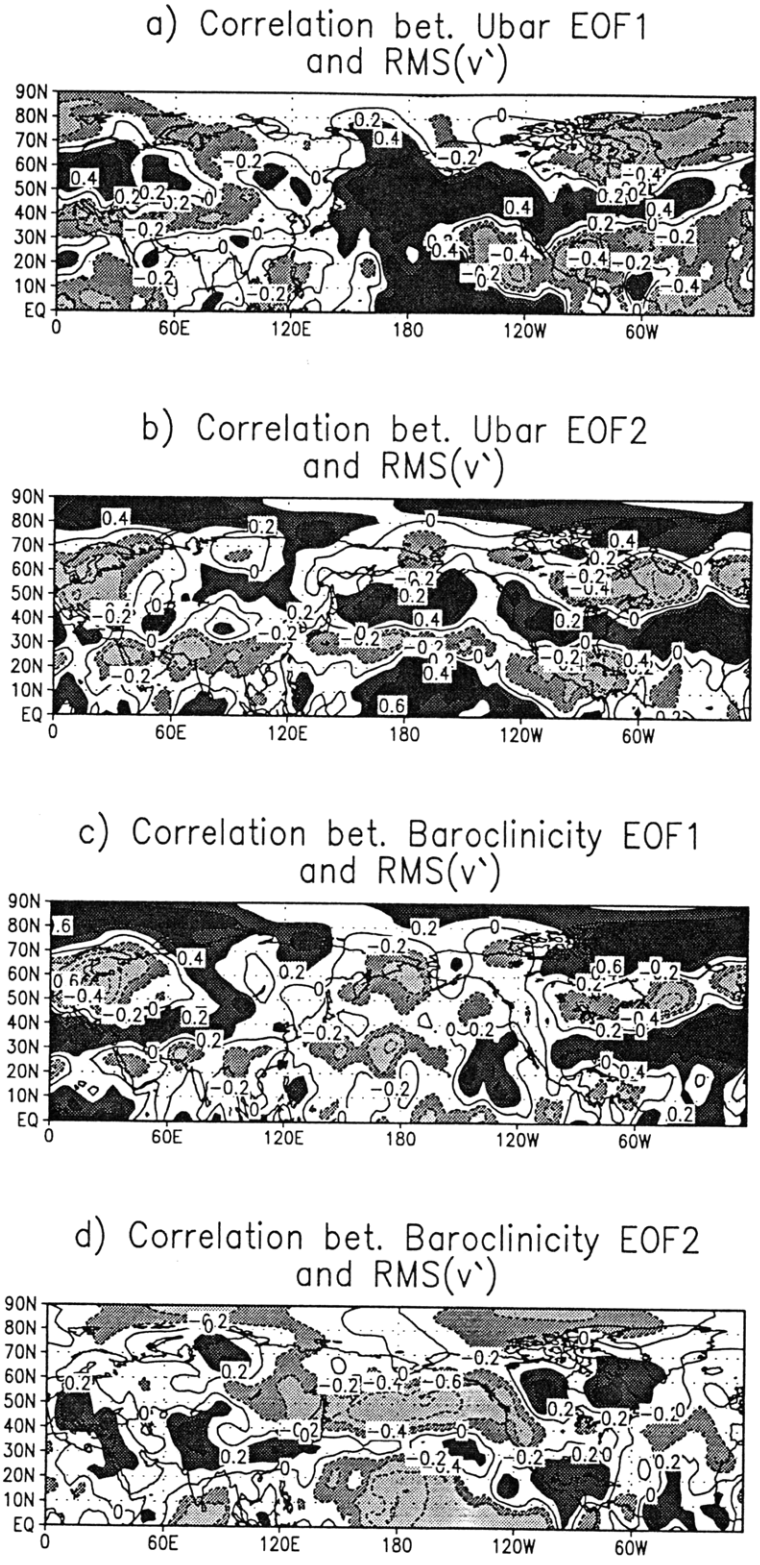

Figure 3-12: a) Correlation between temporal coefficients of Ubar EOF1 and RMS(v'). b) Same as a) except for temporal coefficients of Ubar EOF2. c) Same as a) except for temporal coefficients of baroclinicity EOF1. d) Same as a) except for temporal coefficients of baroclinicity EOF2. Contour interval 0.2. The different shades represent absolute values greater than 0.2 and 0.4.

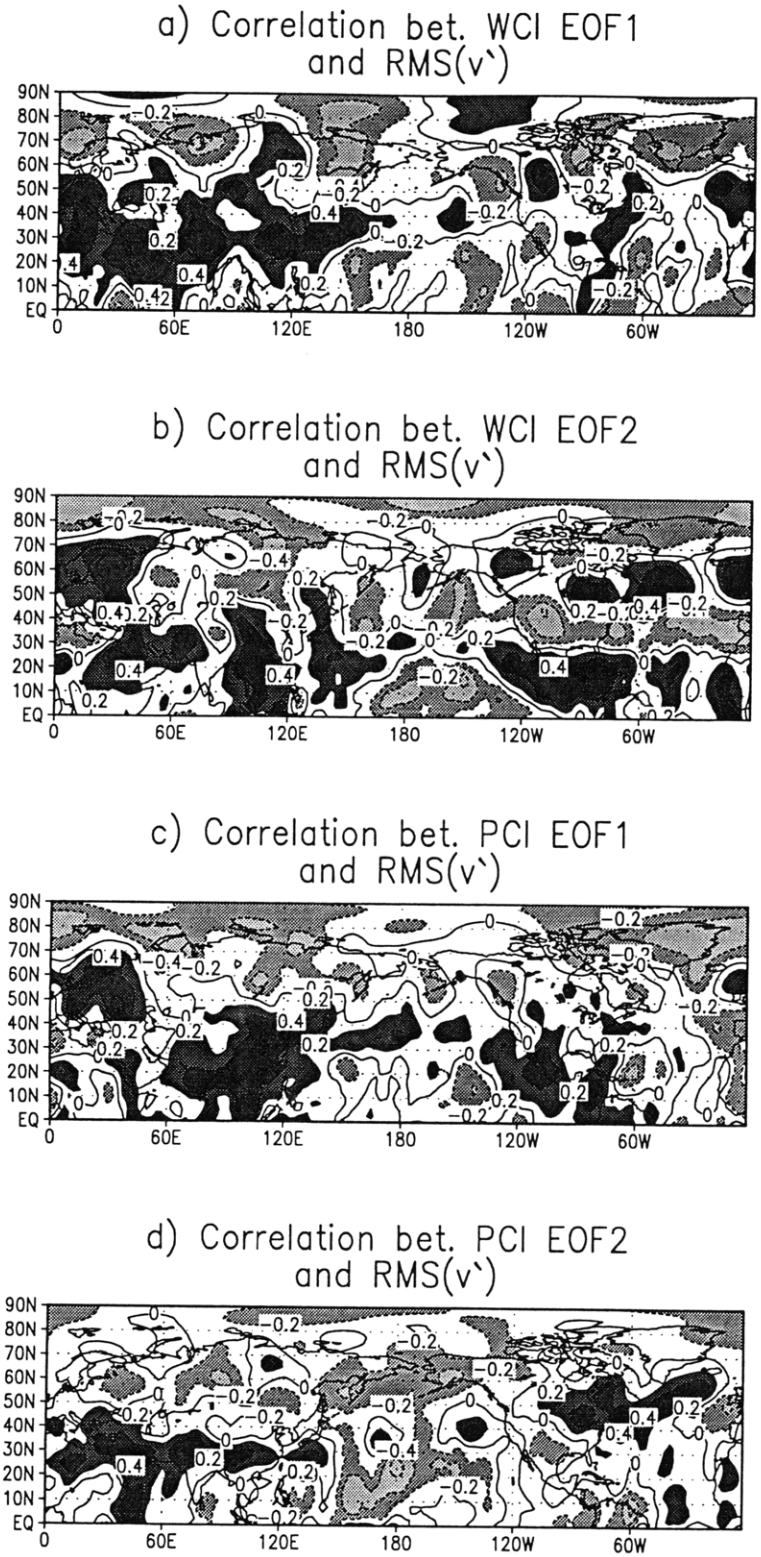

Figure 3-13: a) Correlation between temporal coefficients of WCI EOF1 and RMS(v'). b) Same as a) except for temporal coefficients of WCI EOF2. c) Same as a) except for temporal coefficients of PCI EOF1. d) Same as a) except for temporal coefficients of PCI EOF2. Contour interval 0.2. The different shades represent absolute values greater than 0.2 and 0.4.

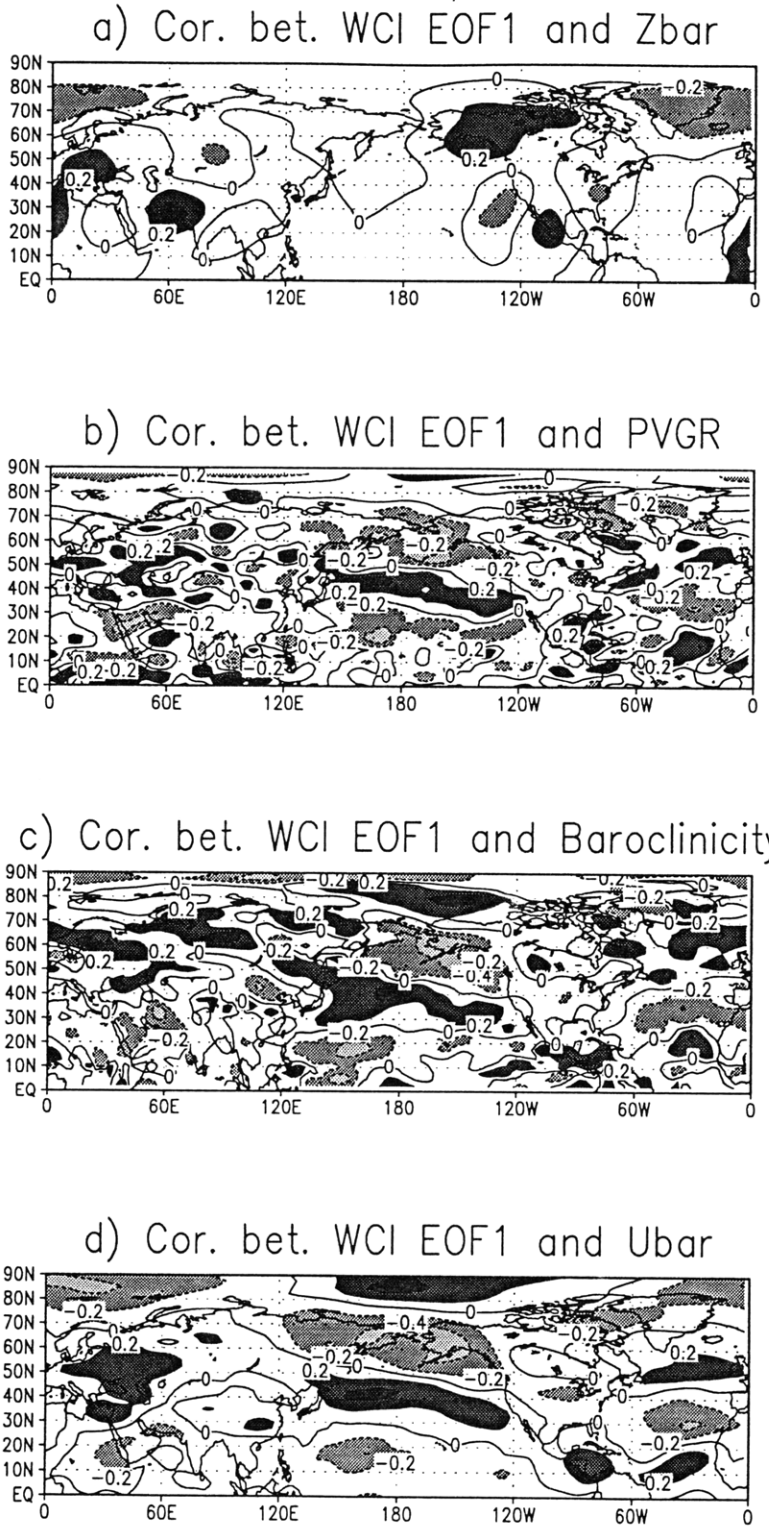

Figure 3-14: a) Correlation between temporal coefficients of WCI EOF1 and Zbar. b) Same as a) except between WCI EOF1 and PVGR. c) Same as a) except between WCI EOF1 and baroclinicity. d) Same as a) except between WCI EOF1 and Ubar. Contour interval 0.2. The different shades represent absolute values greater than 0.2 and 0.4.

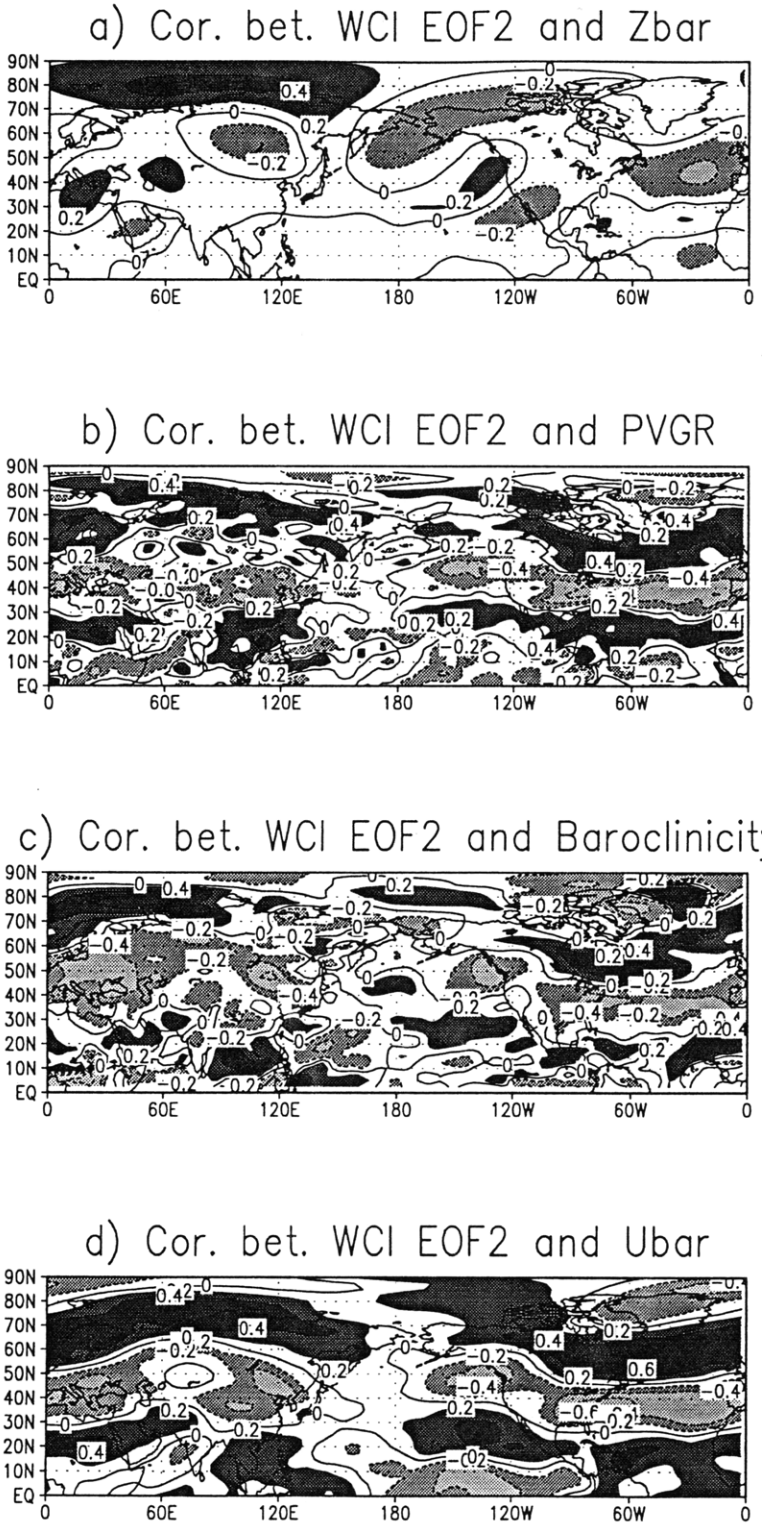

Figure 3-15: Same as Fig. 3-14 except for the correlation between WCI EOF2 and basic states.

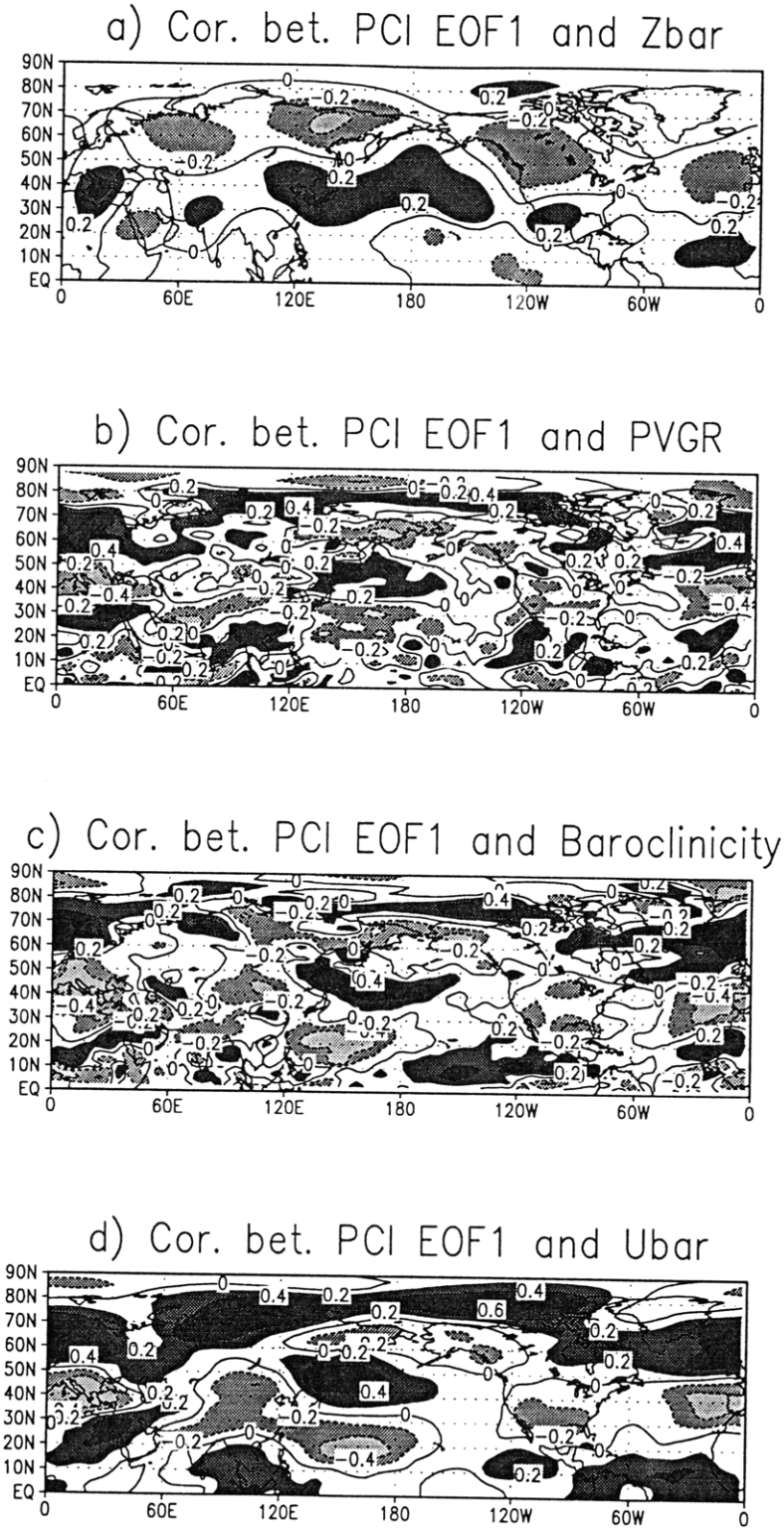

Figure 3-16: Same as Fig. 3-14 except for the correlation between PCI EOF1 and basic states.

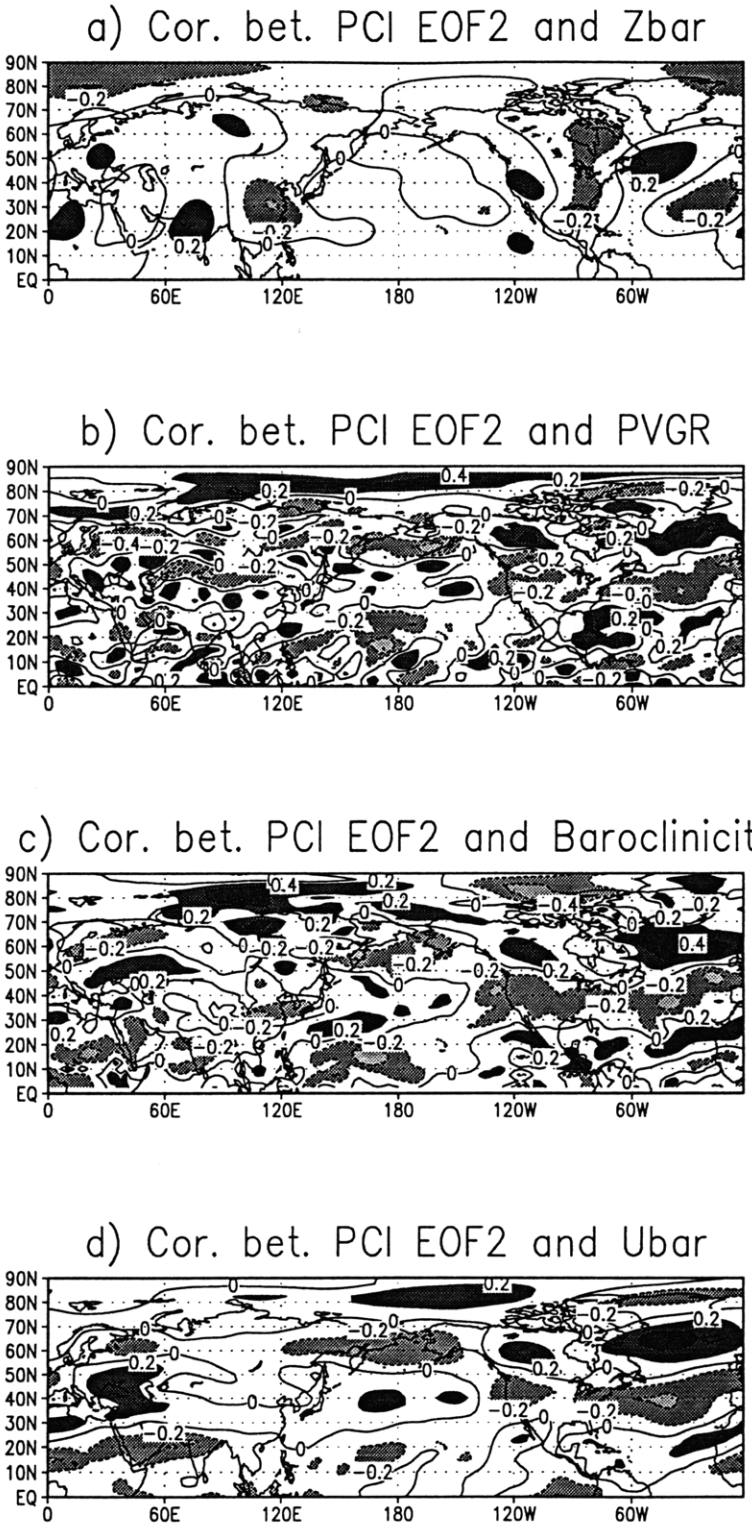

Figure 3-17: Same as Fig. 3-14 except for the correlation between PCI EOF2 and basic states.

b) Spatial correlation between Fig. 3-13b and Fig. 2-1b: 0.72. Correlation between temporal coefficients of WCI EOF2 and RMS(v') EOF2: 0.67.

c) Spatial correlation between Fig. 3-13c and Fig. 2-1b: 0.63. Correlation between temporal coefficients of PCI EOF1 and RMS(v') EOF2: 0.53.

d) Spatial correlation between Fig. 3-13d and Fig. 2-1d: 0.44. Correlation between temporal coefficients of PCI EOF2 and RMS(v') EOF4: 0.33.

Hence we can see that at least two leading modes of interannual variability of storm tracks are associated to the variations of WCI or PCI. This supports our expectation that propagation of baroclinic waves and wave packets can also influence the variation of storm tracks.

In order to further see what accounts for the interannual variability of WCI and PCI, we are going to correlate their temporal coefficients of EOF1 and EOF2 modes to four so-called basic states, e.g., baroclinicity, IPV gradient (PVGR), Ubar and unfiltered Zbar (seasonal mean geopotential height). Results are shown in Figs. 3-14 to 3-17. The noisier patterns are the correlations between EOF modes and baroclinicity , PVGR, which is natural since high-order derivative is involved in calculation of baroclinicity and PVGR. The correlations between EOF modes and Zbar, however, are smaller. It seems Ubar can have some possible relation with WCI (Fig. 3-15d). However, since most of the correlations are low (<0.36) except for Fig. 3-15d, it's difficult to contribute the principle modes of interannual variabilities of WCI and PCI to the basic states shown above. Further investigations about this will be carried out in the next subsection.

3.5.2 Composite charts constructed according to objective analysis

Besides the composite charts constructed according to the magnitudes of EOF modes of interannual variations, we also construct composite charts using other objective

analysis. First, we chose 6 areas of interest [2] along the baroclinic wave guides and calculate the area-averaged value of WCI in 23 winters. For each area, the 23 time series of WCI were ranked according to their values. Those 3 years with the largest and lowest WCI were then identified, and the one-point (located within the concerned area) timelag correlation of v' was averaged over these years to form high and low composite charts. In order to see their relations with basic state flow, storm tracks and timelag correlation of ve, we also display composite charts of Ubar, RMS(v') and timalg correlations of ve averaged over corresponding composite years. All results are shown in Figs. 3-18—3-35. Inspection of all figures reveals some characteristics listed below.

a.1) Upstream of 40N, 140E (Fig. 3-18): Both the southern and northern branches of wave path (referred to the upstream regions with higher coherence and showing wave structure) upstream of base ponit are much lower in low composite years than in high composite years. Ubar and RMS(v') in the southern branch is stronger in the high composite years, while contrary in the northern branch.

a.2) Downstream of 40N, 140E (Fig. 3-19): The wave path in the high composite years bears a bit higher coherence and the wave path in the low composite years split into two parts when waves propagate into the America. Both Ubar and RMS(v') in the high composite years increase along the central position of wave path.

b.1) Upstream of 40N, 170W (Fig. 3-20): The wave coherence, Ubar and RMS(v') increase along the wave path in the high composite years and vice versa.

b.2) Downstream of 40N, 170W (Fig. 3-21): When the timelag correlations increase along the wave path in America in the high composite years, Ubar decreases there. However, RMS(v') still shows a little intensification there. It seems possible that higher wave coherence cancels the effect of weaker Ubar on storm tracks.

c.1) Upstream of 40N, 120W (Fig. 3-22): Wave coherence increases in the central band of wave path (150E:120W, 40N:50N) in the high composite years. Ubar in this band in the corresponding years, however, doesn't show an uniform change. It seems

[2]The 6 areas are: (130E-145E, 30N-45N), (180-165W, 30N-45N), (125W-110W, 35N-50N), (70W-55W, 35N-50N), (5W-10E, 30N-45N), (60E-75E, 20N-35N).

to be stronger in northern band and weaker in the southern band. Compared with the change of Ubar, RMS(v') is found to be uniformly stronger in the whole band in the high composite years.

c.2) Downstream of 40N, 120W (Fig. 3-23): The wave coherence, Ubar and RMS(v') increase along the central wave path in the high composite years and vice versa.

d.1) Upstream of 40N, 60W (Fig. 3-24): When the timelag correlations increase along the wave path to the Northeast of America in the high composite years, Ubar decrease there. However, RMS(v') still shows a strong intensification there. In other parts of wave path, timelag correlation, Ubar and RMS(v') all increase in the high composite years.

d.2) Downstream of 40N, 60W (Fig. 3-25): In this case, Ubar remains fairly steady along the wave path in the different composite years. However, RMS(v') still increases along the wave path in the high composite years when timelag correlations are higher there.

e.1) Upstream of 40N, 0 (Fig. 3-26): Similar to the case d.1), Ubar decreases in most parts of wave path when wave coherence increases, while RMS(v') still becomes stronger.

e.2) Downstream of 40N, 0 (Fig. 3-27): Even we can see Ubar is intensified near wave path, but the shape and position of intensified band are not in good agreement with that of wave path. However, the change of RMS(v') along the wave path depicts a perfect agreement between them.

f.1) Upstream of 25N, 70E (Fig. 3-28): This case is similar to case e.2) and won't be repeated here.

f.2) Downstream of 25N, 70E (Fig. 3-29): Ubar decreases in South Asia and remains almost unchanged in East Asia when wave coherence increases in above regions. Compared with Ubar, the change of RMS(v') again is in better agreement with the change of wave path between different composite years.

In general, we find when the timelag correlations of v' are higher somewhere, local RMS(v') always increase too. Ubar seems to have some relation with the variation of

timelag correlation, but not so obvious as RMS(v'). Also, difference between RMS(v') over two composite years (compared with difference between Ubar over two composite years) is in better agreement with difference of timelag correlation of v' between high and low composite years, either in position or shape. Furthermore, from Figs. 3-30 to 3-35, we only find 2 cases (from total of 12 cases) that timelag correlation of ve is not higher in the years with higher timelag correlation of v' (see Figs. 3-31a, b and 3-33c, d). This suggests that certain relation exists between timelag correlations of ve and v'.

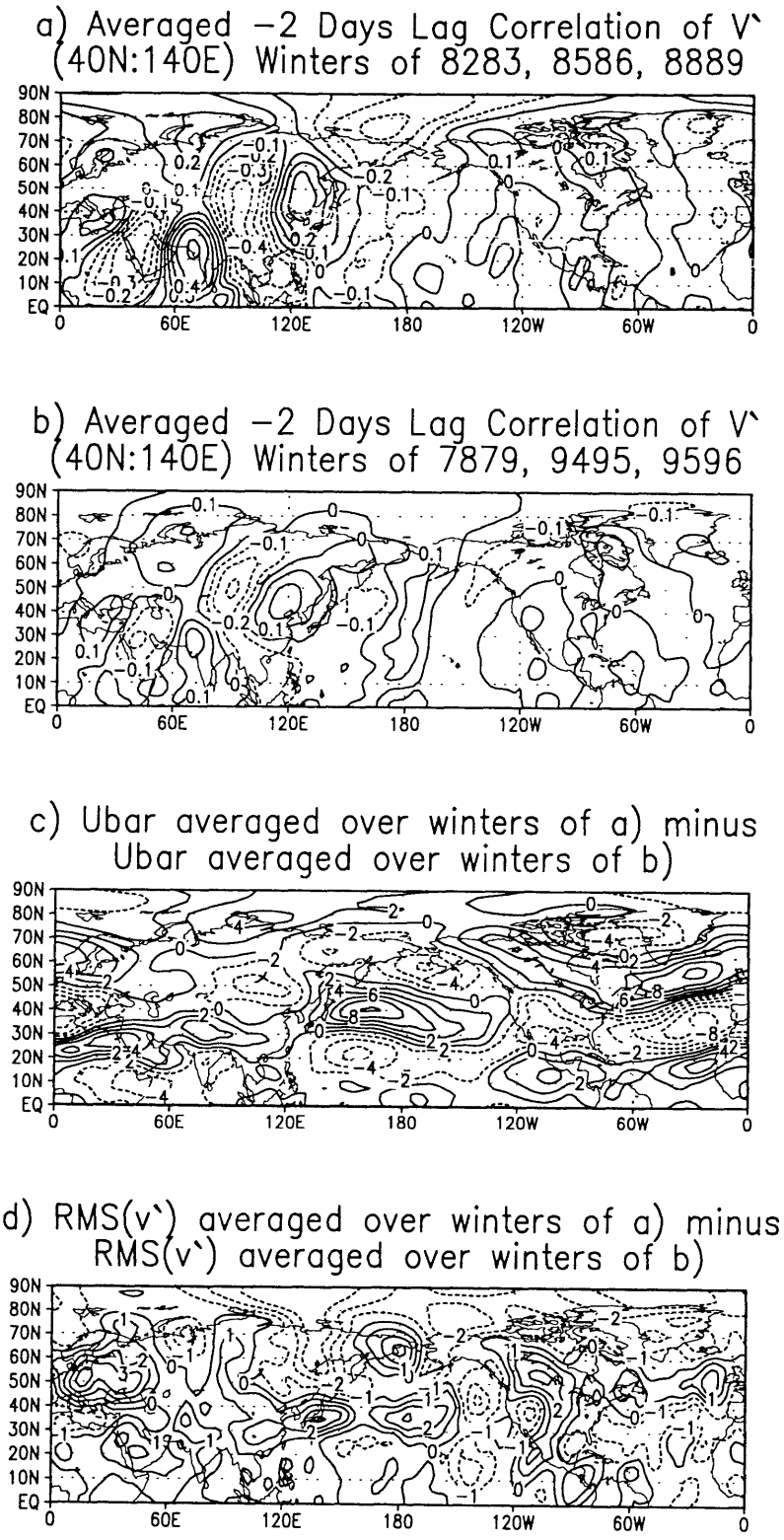

Figure 3-18: a) High composite of -2 days timelag correlation of v', base point (40N:140E). b) Low composite of timelag correlation of v', base point (40N:140E). c) Difference between Ubar averaged over high and low composite years. d) Difference between RMS(v') averaged over high and low composite years. Contour intervals are 0.1 in a) and b), $2ms^{-1}$ in c), and $1ms^{-1}$ in d).

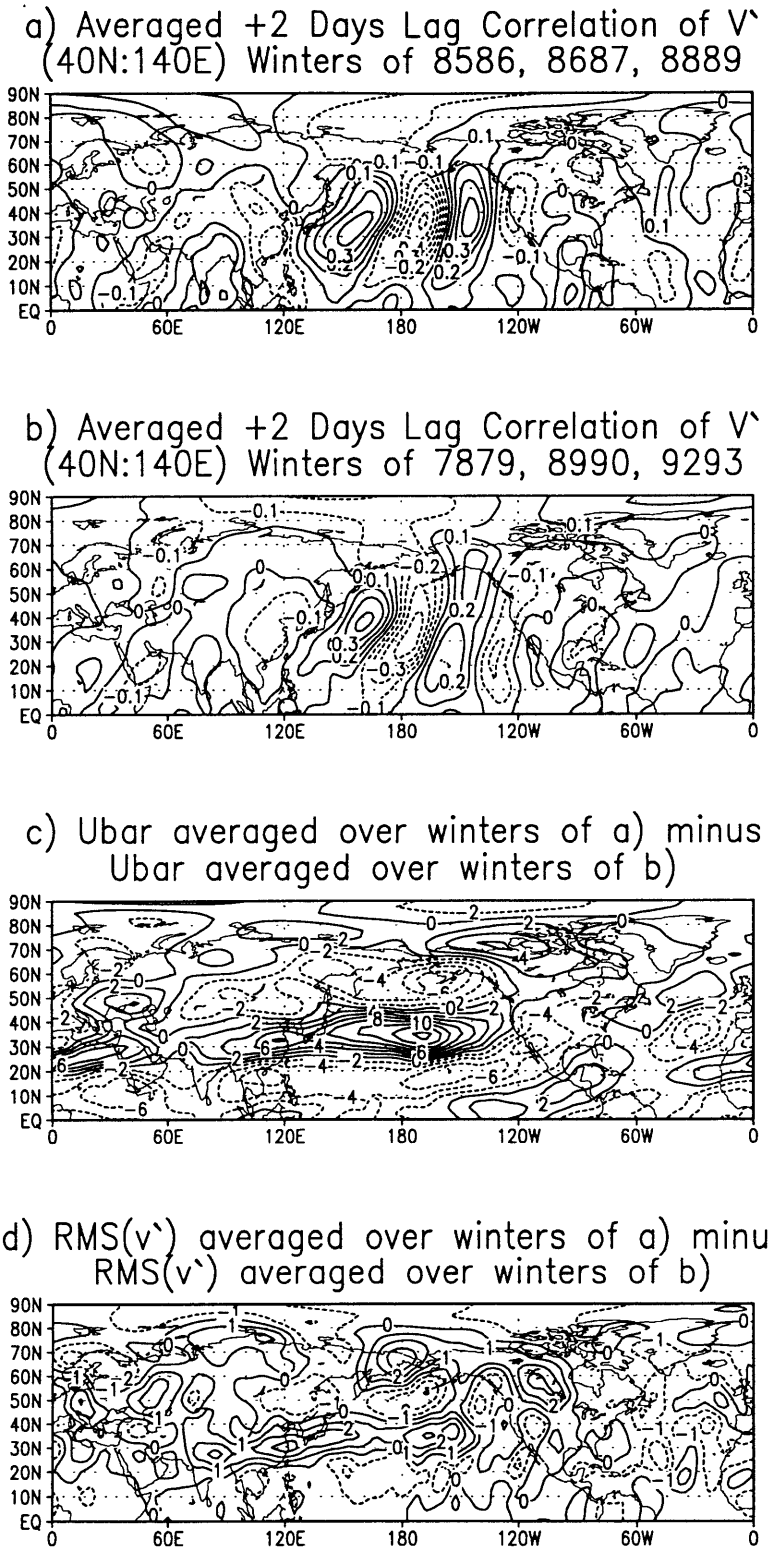

Figure 3-19: Same as Fig. 3-18 except for +2 days timelag correlation of v'

a) Averaged −2 Days Lag Correlation of V`
(40N:170W) Winters of 8586, 8889, 9394

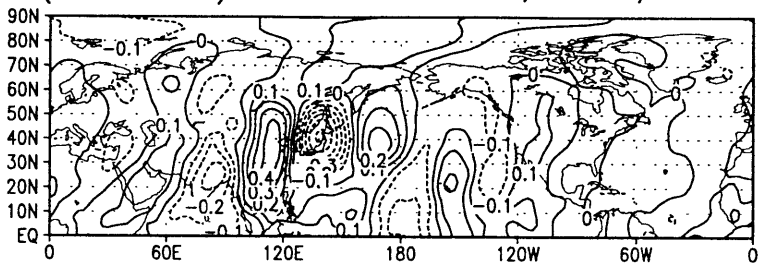

b) Averaged −2 Days Lag Correlation of V`
(40N:170W) Winters of 7879, 8081, 8990

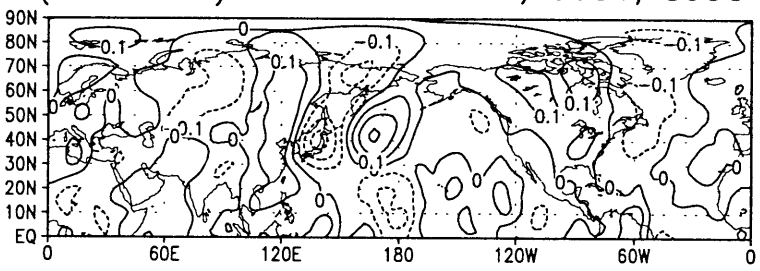

c) Ubar averaged over winters of a) minus
Ubar averaged over winters of b)

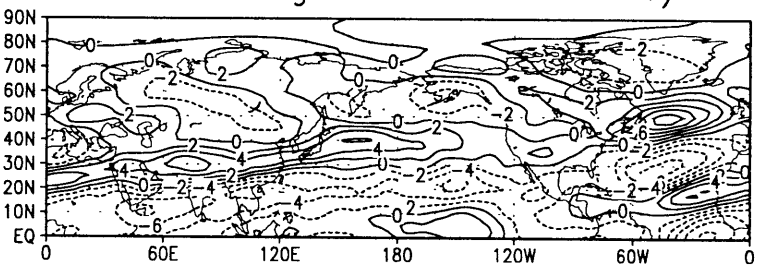

d) RMS(v`) averaged over winters of a) minus
RMS(v`) averaged over winters of b)

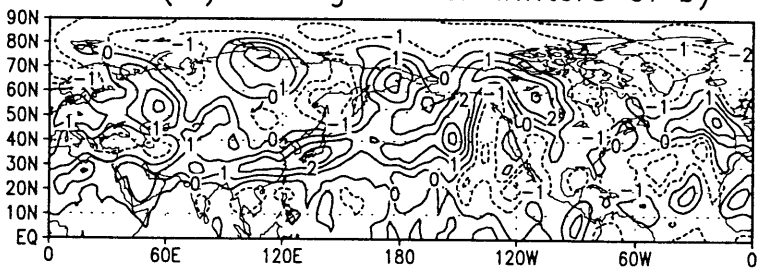

Figure 3-20: Same as Fig. 3-18 except for base point (40N:170W)

a) Averaged +2 Days Lag Correlation of V`
(40N:170W) Winters of 7677, 8687, 9394

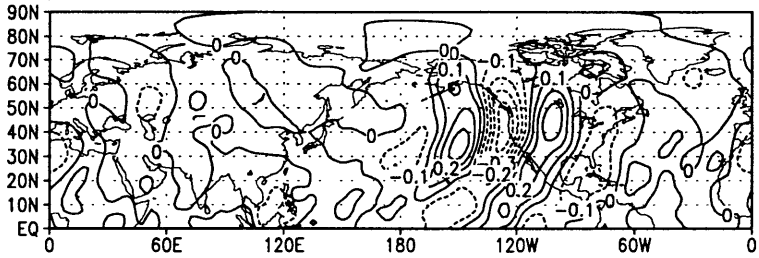

b) Averaged +2 Days Lag Correlation of V`
(40N:170W) Winters of 7980, 8586, 9091

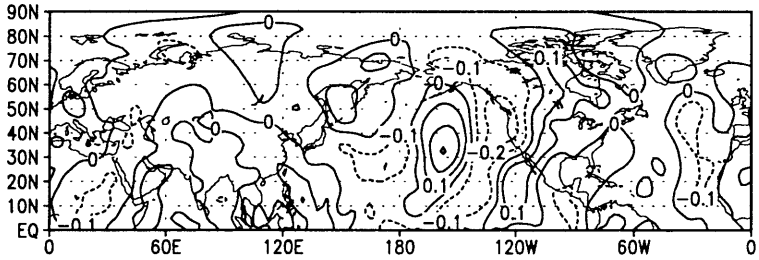

c) Ubar averaged over winters of a) minus
Ubar averaged over winters of b)

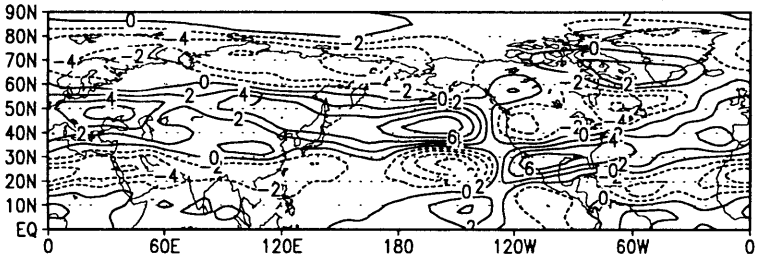

d) RMS(v`) averaged over winters of a) minus
RMS(v`) averaged over winters of b)

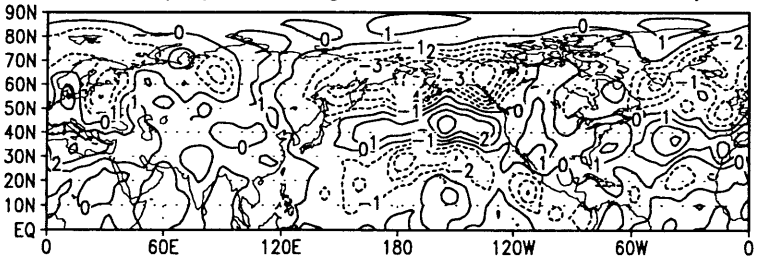

Figure 3-21: Same as Fig. 3-19 except for base point (40N:170W)

a) Averaged −2 Days Lag Correlation of V`
(40N:120W) Winters of 7374, 8182, 9394

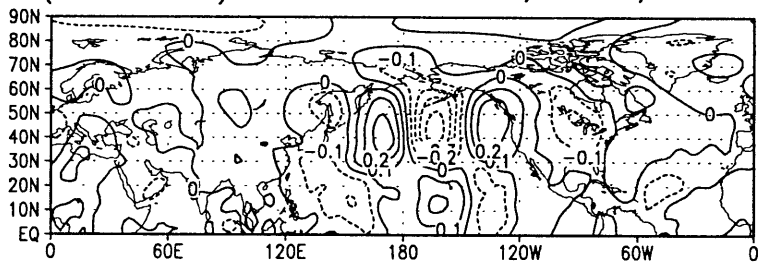

b) Averaged −2 Days Lag Correlation of V`
(40N:120W) Winters of 8283, 8384, 9495

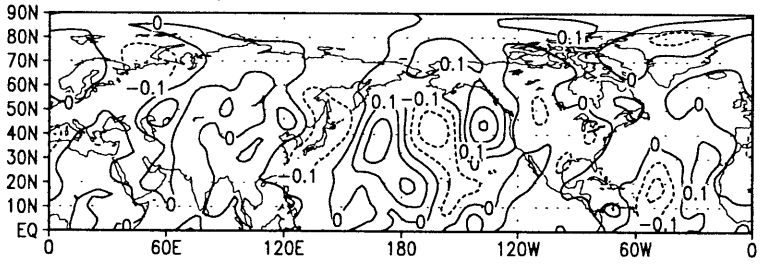

c) Ubar averaged over winters of a) minus
Ubar averaged over winters of b)

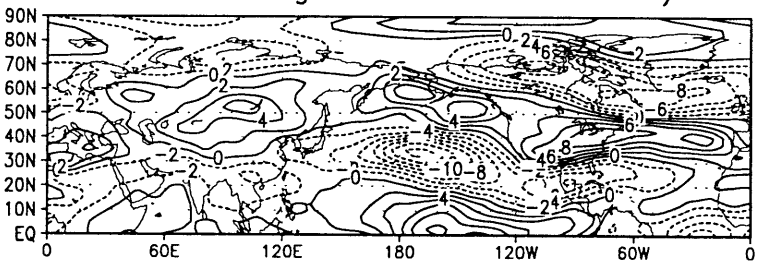

d) RMS(v`) averaged over winters of a) minus
RMS(v`) averaged over winters of b)

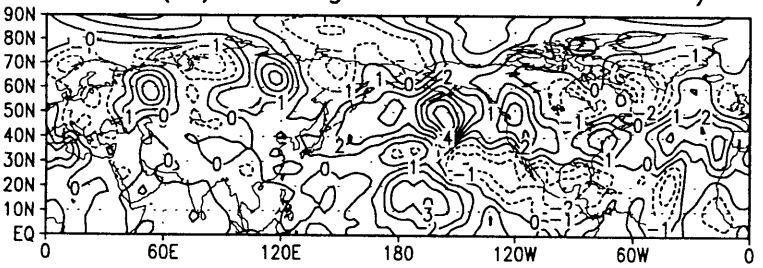

Figure 3-22: Same as Fig. 3-18 except for base point (40N:120W)

a) Averaged +2 Days Lag Correlation of V`
(40N:120W) Winters of 8182, 8788, 9394

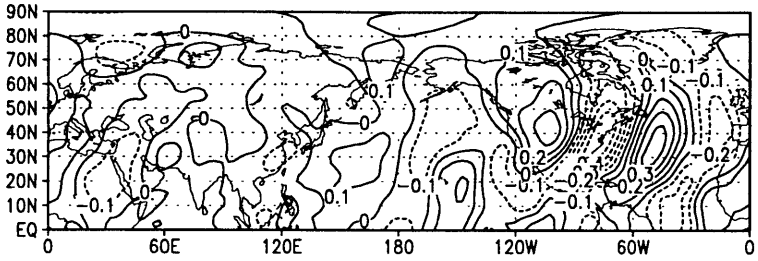

b) Averaged +2 Days Lag Correlation of V`
(40N:120W) Winters of 8384, 8889, 9293

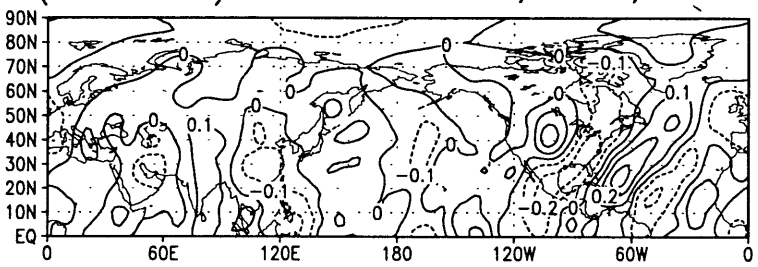

c) Ubar averaged over winters of a) minus
Ubar averaged over winters of b)

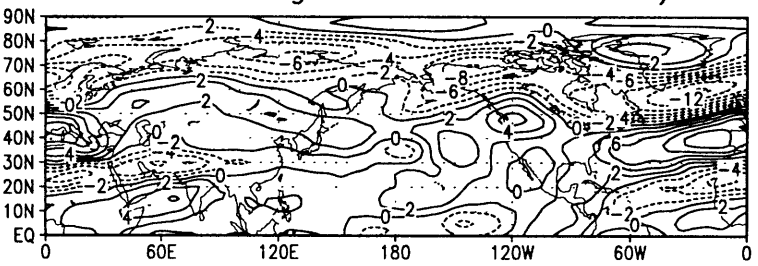

d) RMS(v`) averaged over winters of a) minus
RMS(v`) averaged over winters of b)

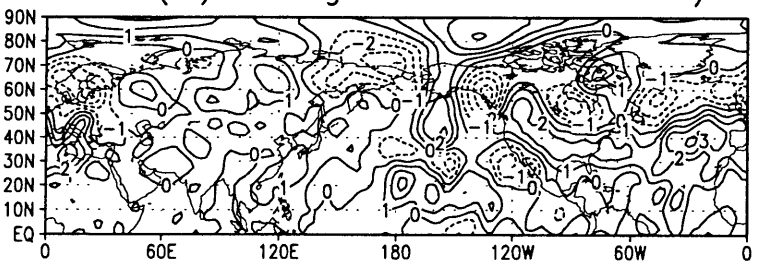

Figure 3-23: Same as Fig. 3-19 except for base point (40N:120W)

a) Averaged −2 Days Lag Correlation of V`
(40N:60W) Winters of 8081, 8182, 9394

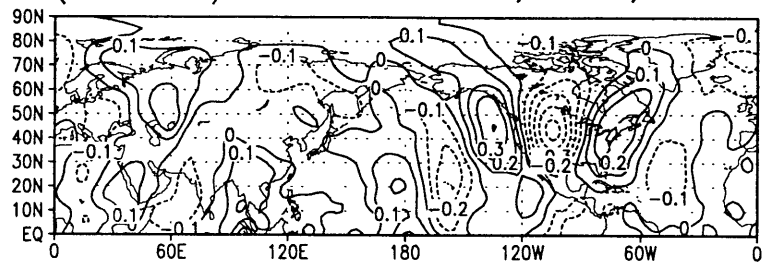

b) Averaged −2 Days Lag Correlation of V`
(40N:60W) Winters of 7980, 8889, 9091

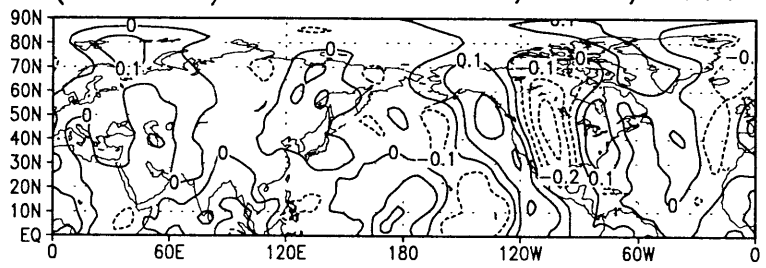

c) Ubar averaged over winters of a) minus
Ubar averaged over winters of b)

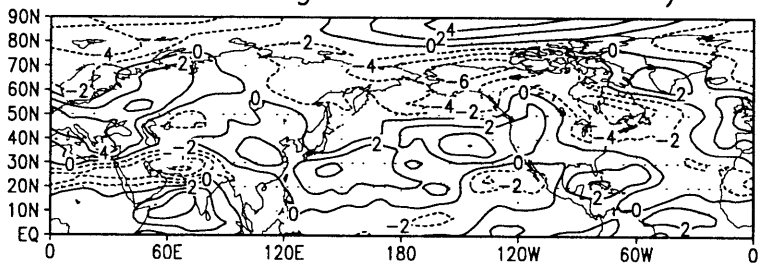

d) RMS(v`) averaged over winters of a) minus
RMS(v`) averaged over winters of b)

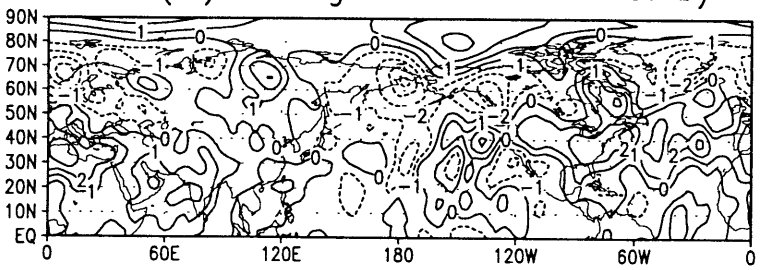

Figure 3-24: Same as Fig. 3-18 except for base point (40N:60W)

a) Averaged +2 Days Lag Correlation of V`
(40N:60W) Winters of 7374, 7778, 9394

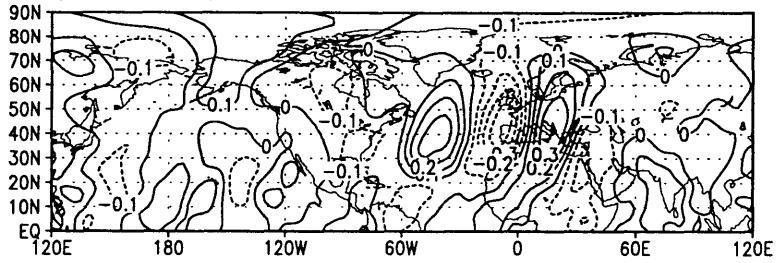

b) Averaged +2 Days Lag Correlation of V`
(40N:60W) Winters of 7980, 8384, 8687

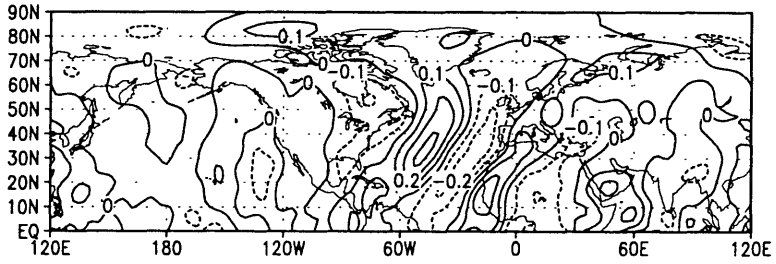

c) Ubar averaged over winters of a) minus
Ubar averaged over winters of b)

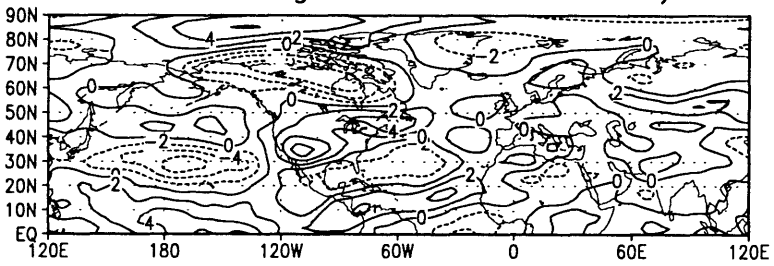

d) RMS(v`) averaged over winters of a) minus
RMS(v`) averaged over winters of b)

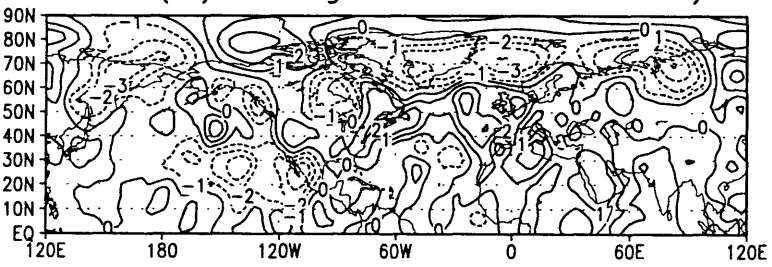

Figure 3-25: Same as Fig. 3-19 except for base point (40N:60W)

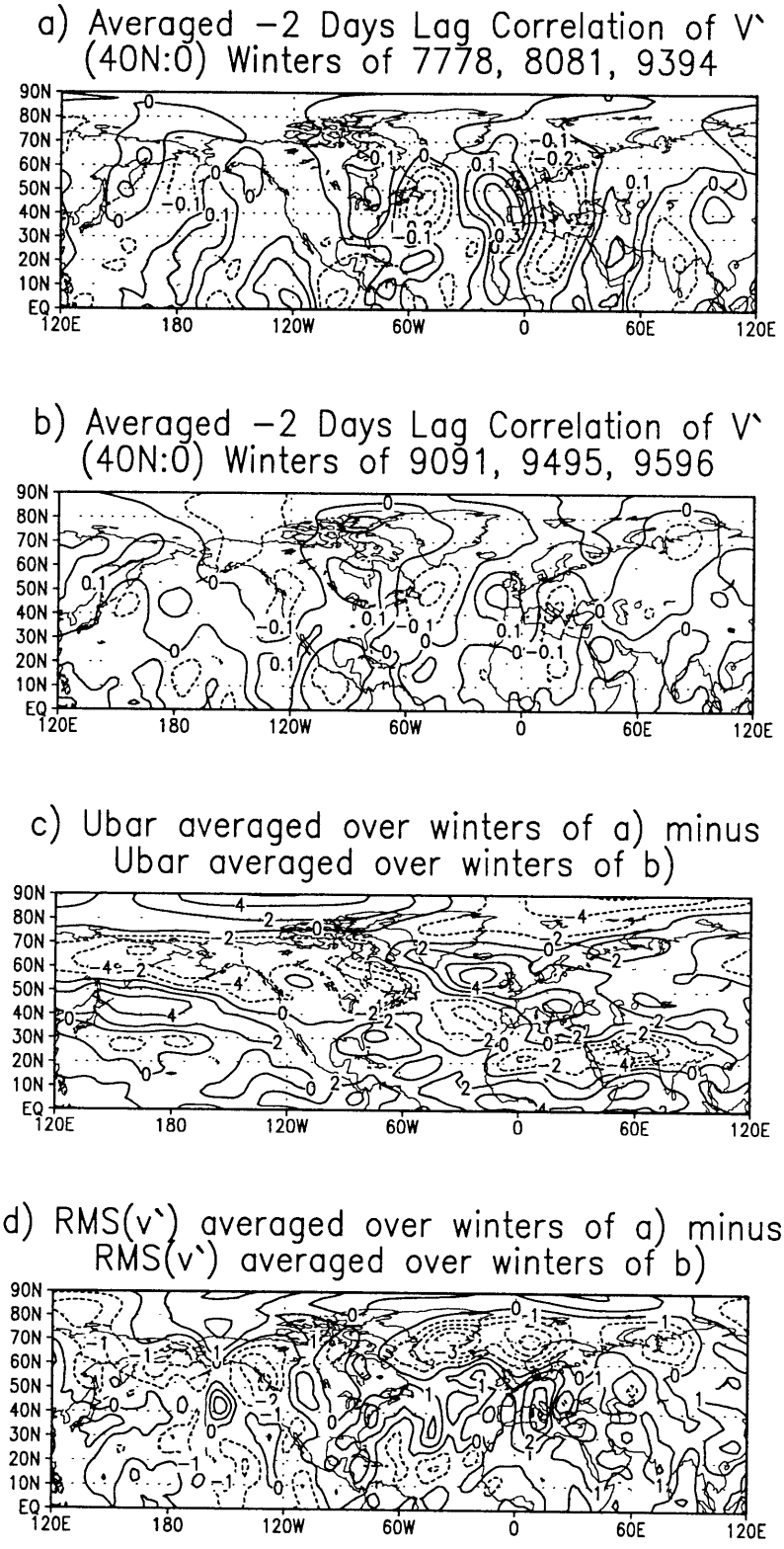

Figure 3-26: Same as Fig. 3-18 except for base point (40N:0)

a) Averaged +2 Days Lag Correlation of V`
(40N:0) Winters of 8081, 8384, 9293

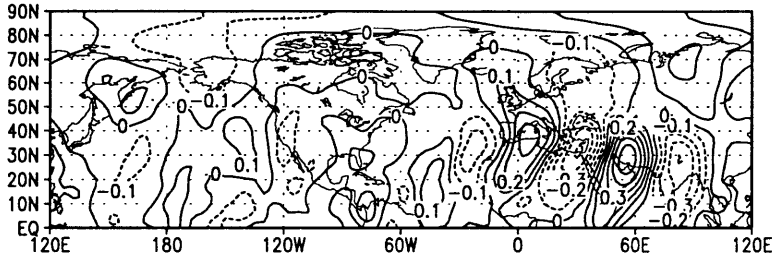

b) Averaged +2 Days Lag Correlation of V`
(40N:0) Winters of 8283, 8990, 9091

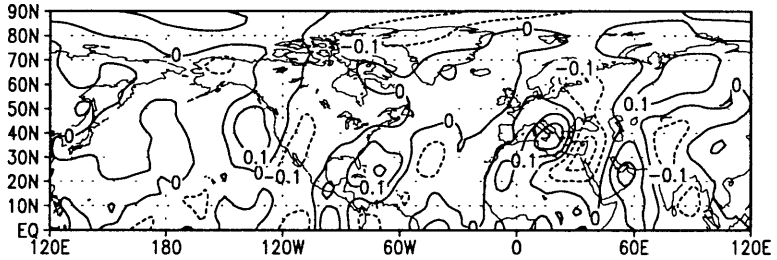

c) Ubar averaged over winters of a) minus
Ubar averaged over winters of b)

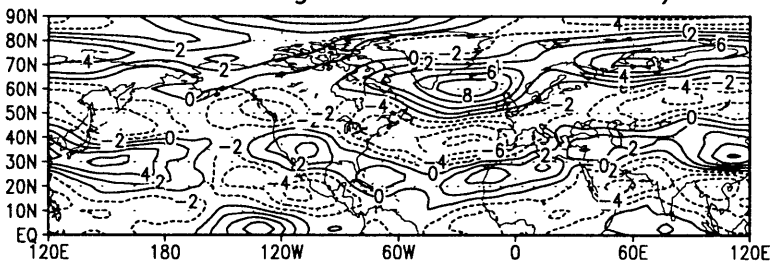

d) RMS(v`) averaged over winters of a) minus
RMS(v`) averaged over winters of b)

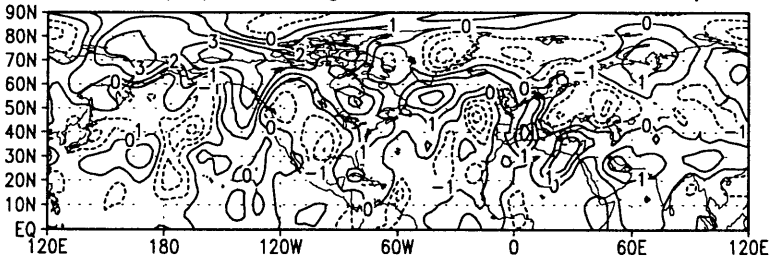

Figure 3-27: Same as Fig. 3-19 except for base point (40N:0)

a) Averaged −2 Days Lag Correlation of V`
(25N:70E) Winters of 8081, 8788, 9192

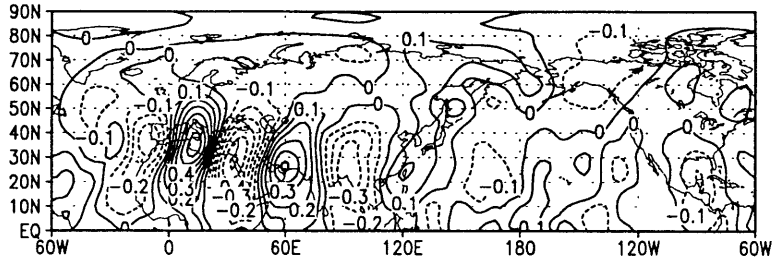

b) Averaged −2 Days Lag Correlation of V`
(25N:70E) Winters of 7879, 8586, 8990

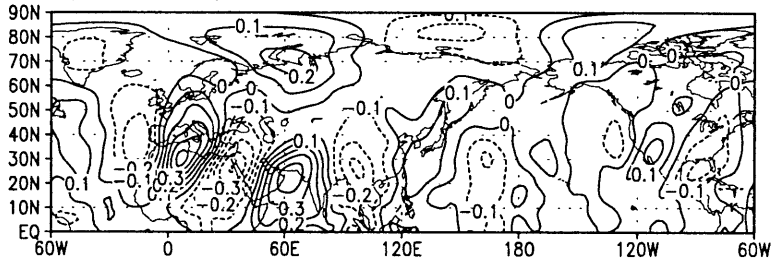

c) Ubar averaged over winters of a) minus
Ubar averaged over winters of b)

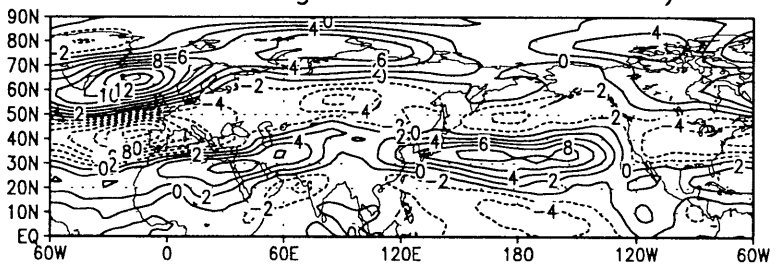

d) RMS(v`) averaged over winters of a) minus
RMS(v`) averaged over winters of b)

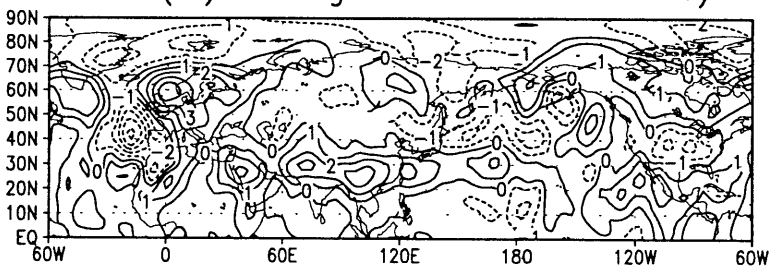

Figure 3-28: Same as Fig. 3-18 except for base point (25N:70E)

a) Averaged +2 Days Lag Correlation of V`
(25N:70E) Winters of 8182, 8788, 9394

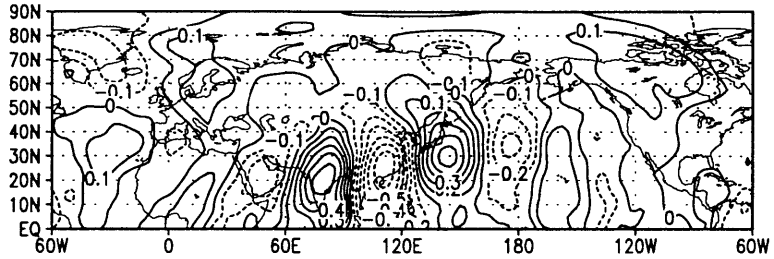

b) Averaged +2 Days Lag Correlation of V`
(25N:70E) Winters of 7475, 7879, 9596

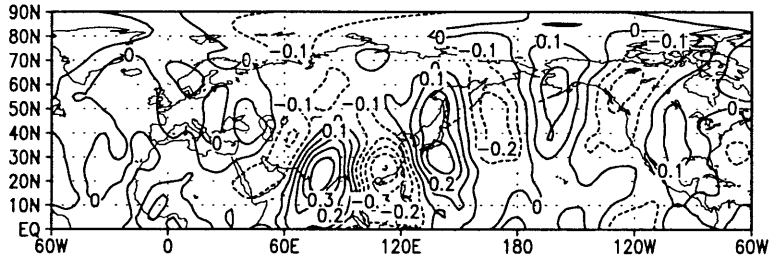

c) Ubar averaged over winters of a) minus
Ubar averaged over winters of b)

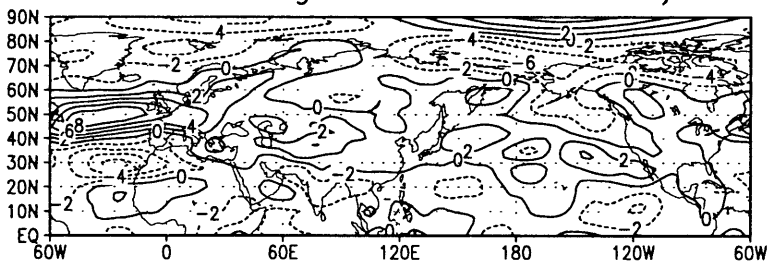

d) RMS(v`) averaged over winters of a) minus
RMS(v`) averaged over winters of b)

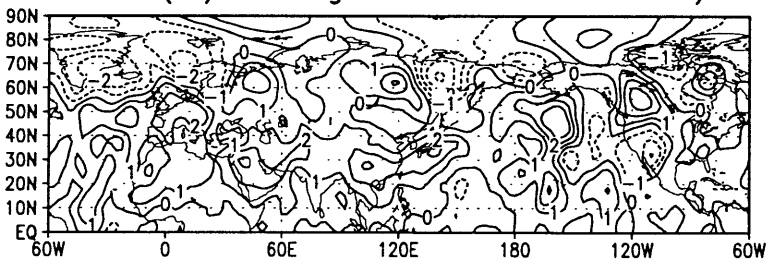

Figure 3-29: Same as Fig. 3-19 except for base point (25N:70E)

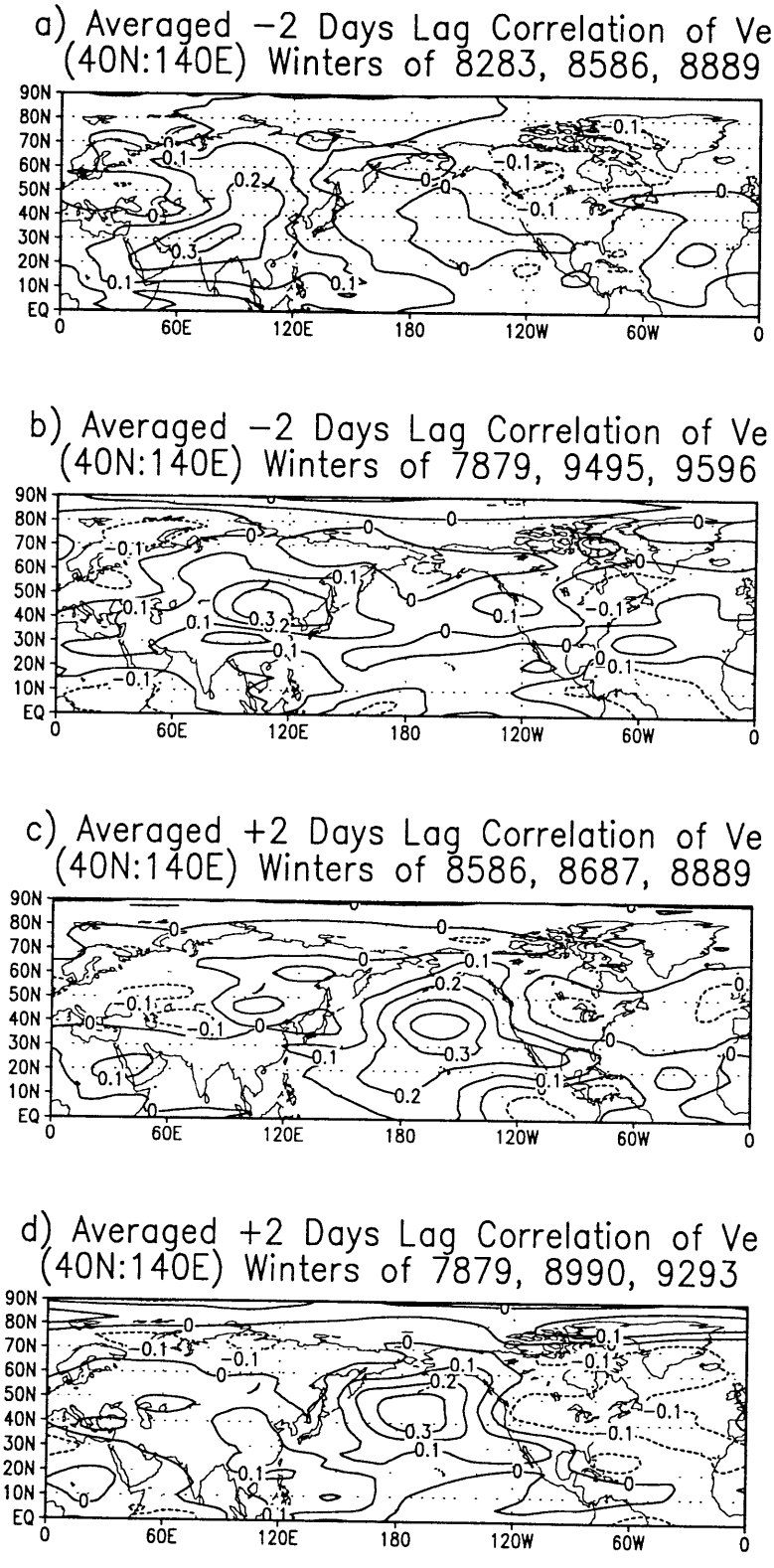

Figure 3-30: a) -2 Days timelag correlation of *ve* averaged over the high composite years in Fig. 3-18a). b) Same as a) except for the low composite years in Fig. 3-18b). c) +2 days timelag correlation of *ve* averaged over the high composite years in Fig. 3-19a). d) Same as c) except for the low composite years in Fig. 3-19b). Contour interval 0.1.

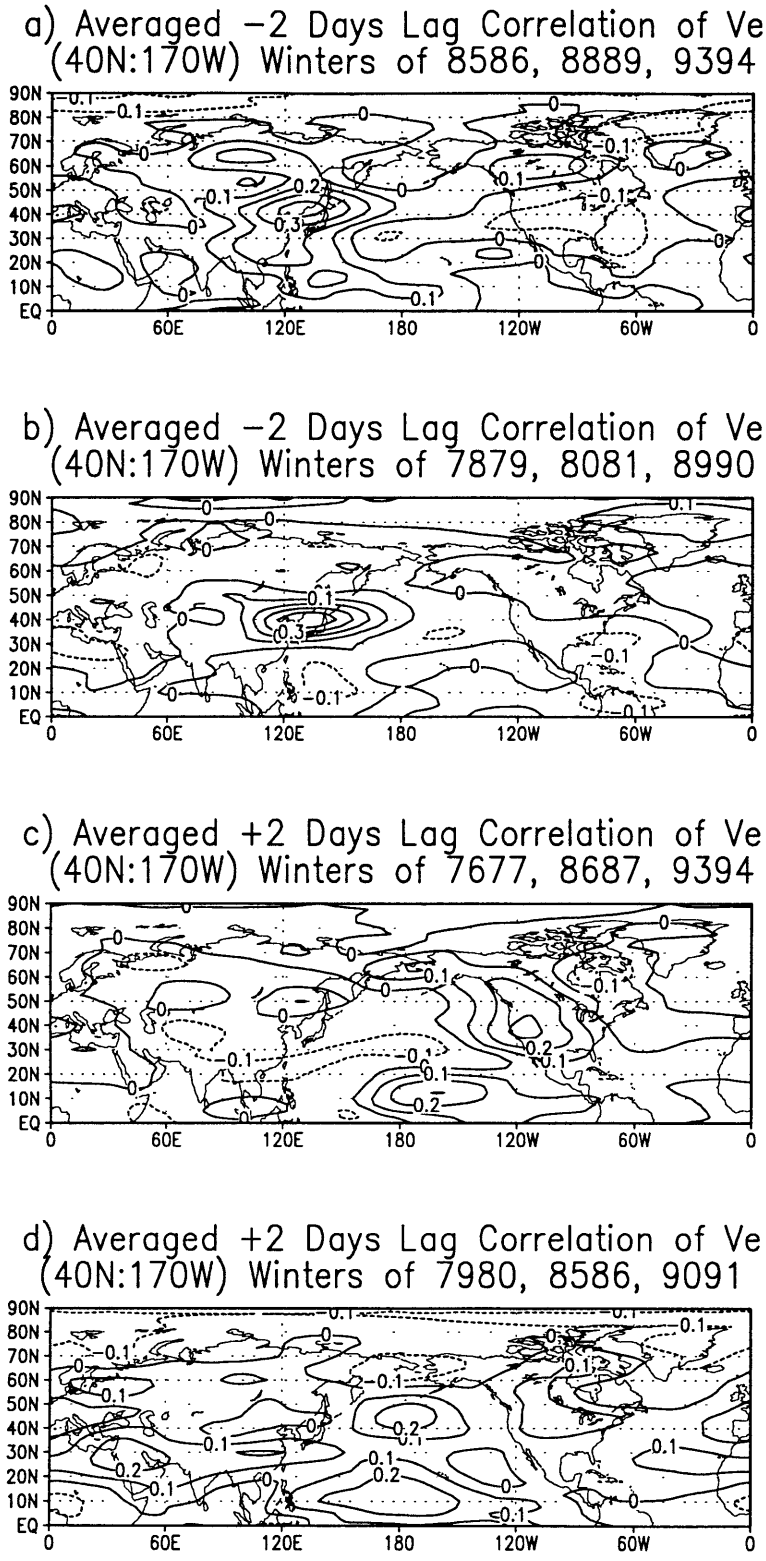

Figure 3-31: a) -2 Days timelag correlation of *ve* averaged over the high composite years in Fig. 3-20a). b) Same as a) except for the low composite years in Fig. 3-20b). c) +2 days timelag correlation of *ve* averaged over the high composite years in Fig. 3-21a). d) Same as c) except for the low composite years in Fig. 3-21b). Contour interval 0.1.

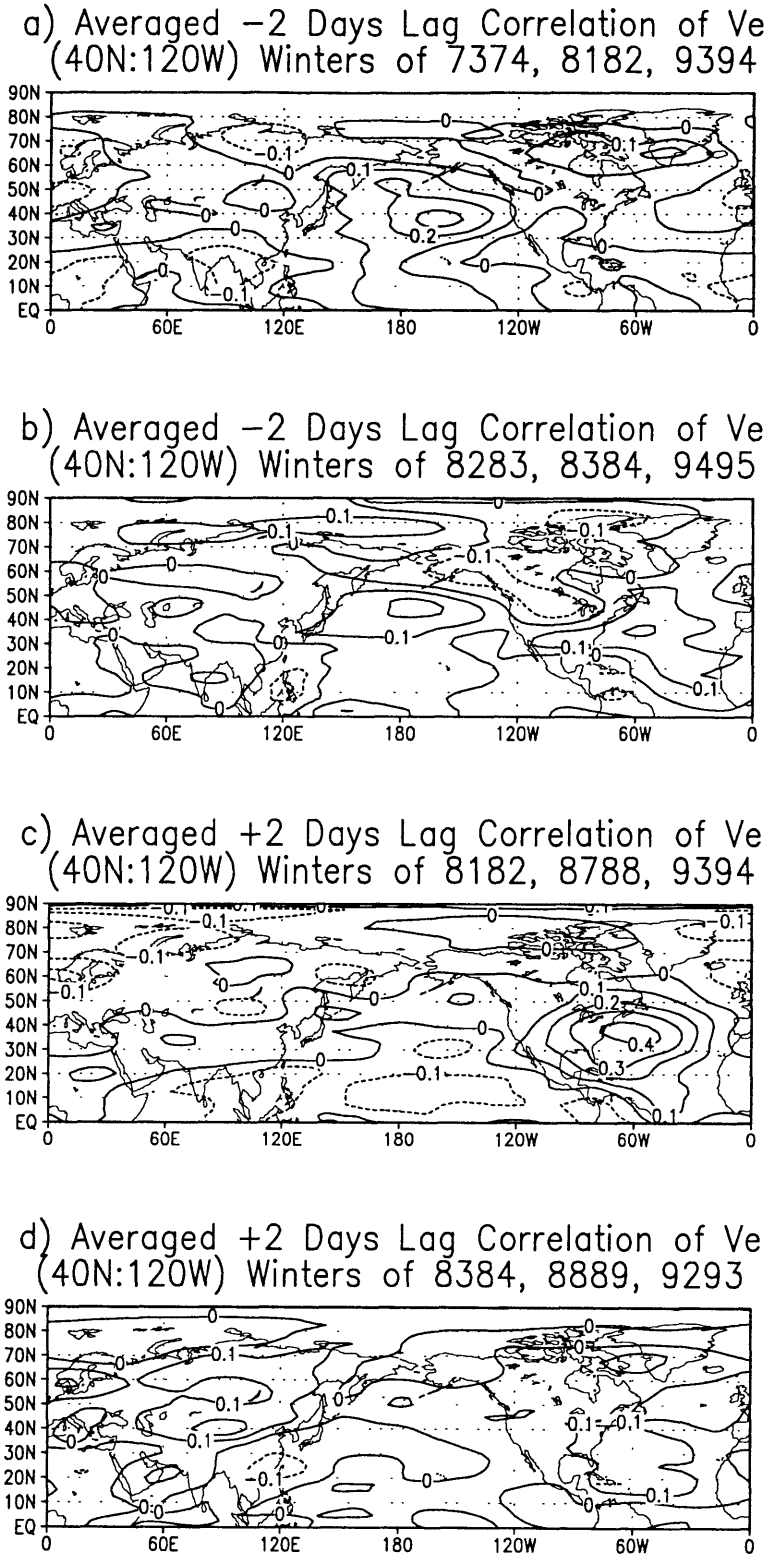

Figure 3-32: a) -2 Days timelag correlation of *ve* averaged over the high composite years in Fig. 3-22a). b) Same as a) except for the low composite years in Fig. 3-22b). c) +2 days timelag correlation of *ve* averaged over the high composite years in Fig. 3-23a). d) Same as c) except for the low composite years in Fig. 3-23b). Contour interval 0.1.

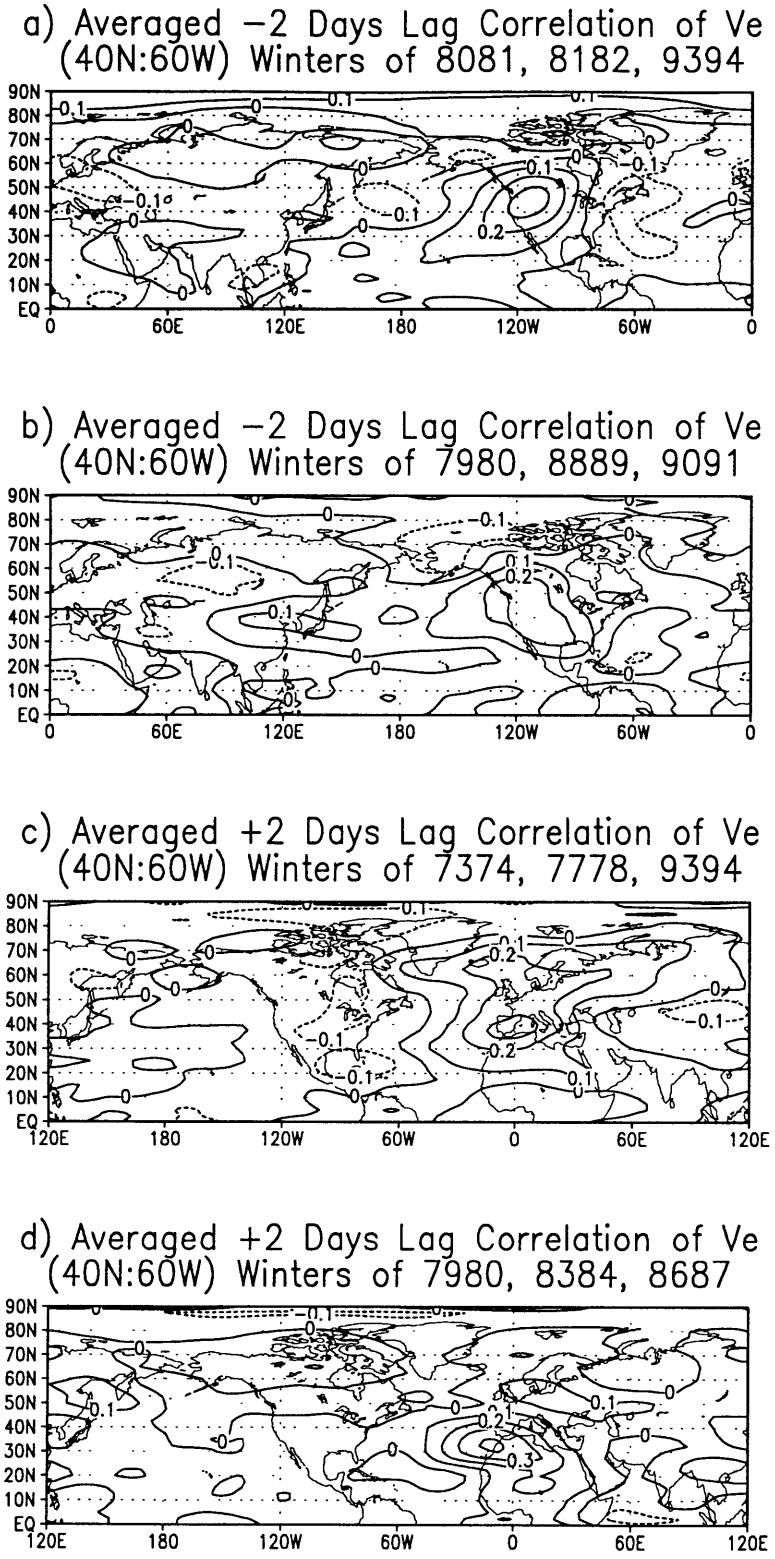

Figure 3-33: a) -2 Days timelag correlation of *ve* averaged over the high composite years in Fig. 3-24a). b) Same as a) except for the low composite years in Fig. 3-24b). c) +2 days timelag correlation of *ve* averaged over the high composite years in Fig. 3-25a). d) Same as c) except for the low composite years in Fig. 3-25b). Contour interval 0.1.

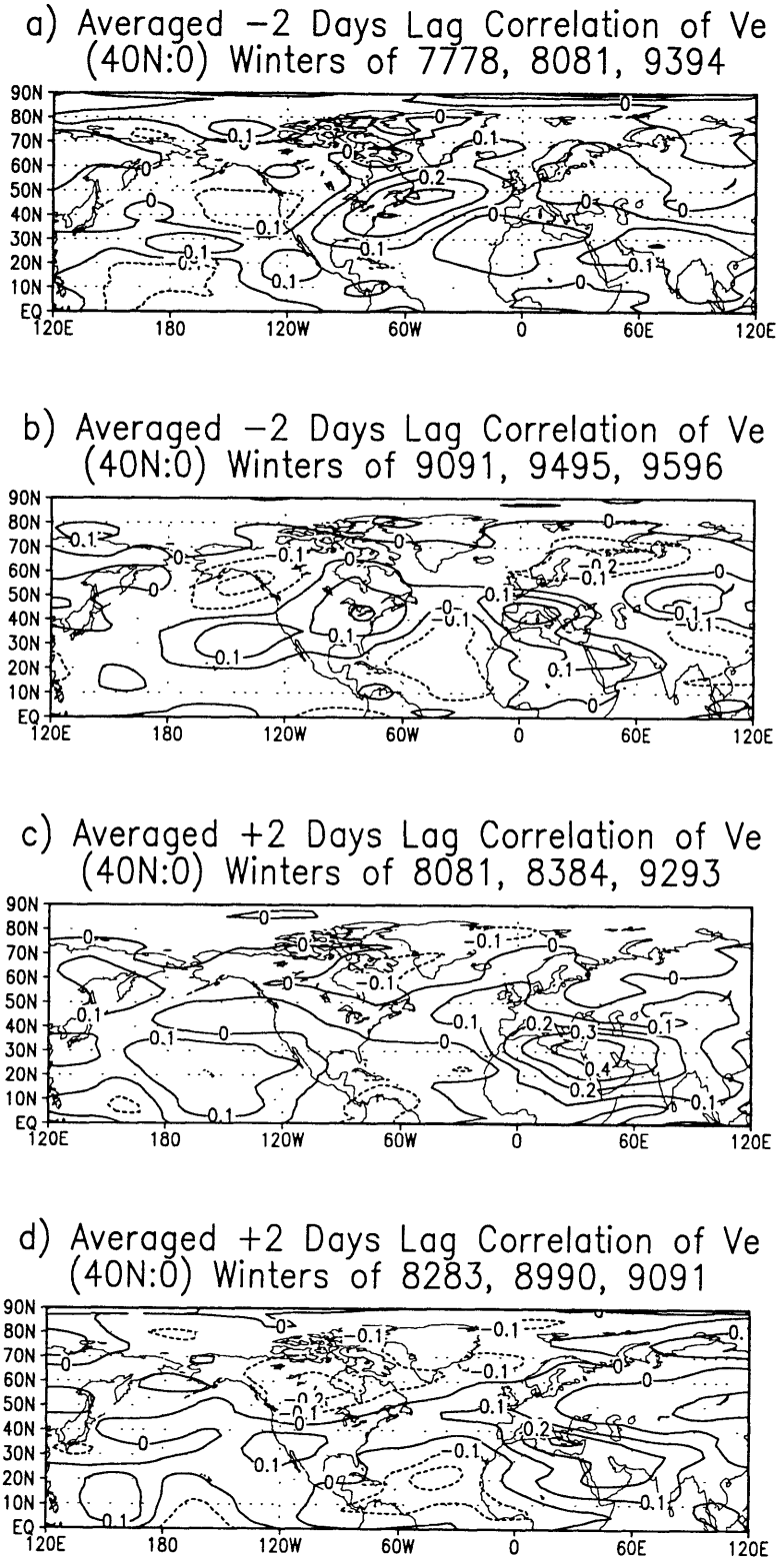

Figure 3-34: a) -2 Days timelag correlation of *ve* averaged over the high composite years in Fig. 3-26a). b) Same as a) except for the low composite years in Fig. 3-26b). c) +2 days timelag correlation of *ve* averaged over the high composite years in Fig. 3-27a). d) Same as c) except for the low composite years in Fig. 3-27b). Contour interval 0.1.

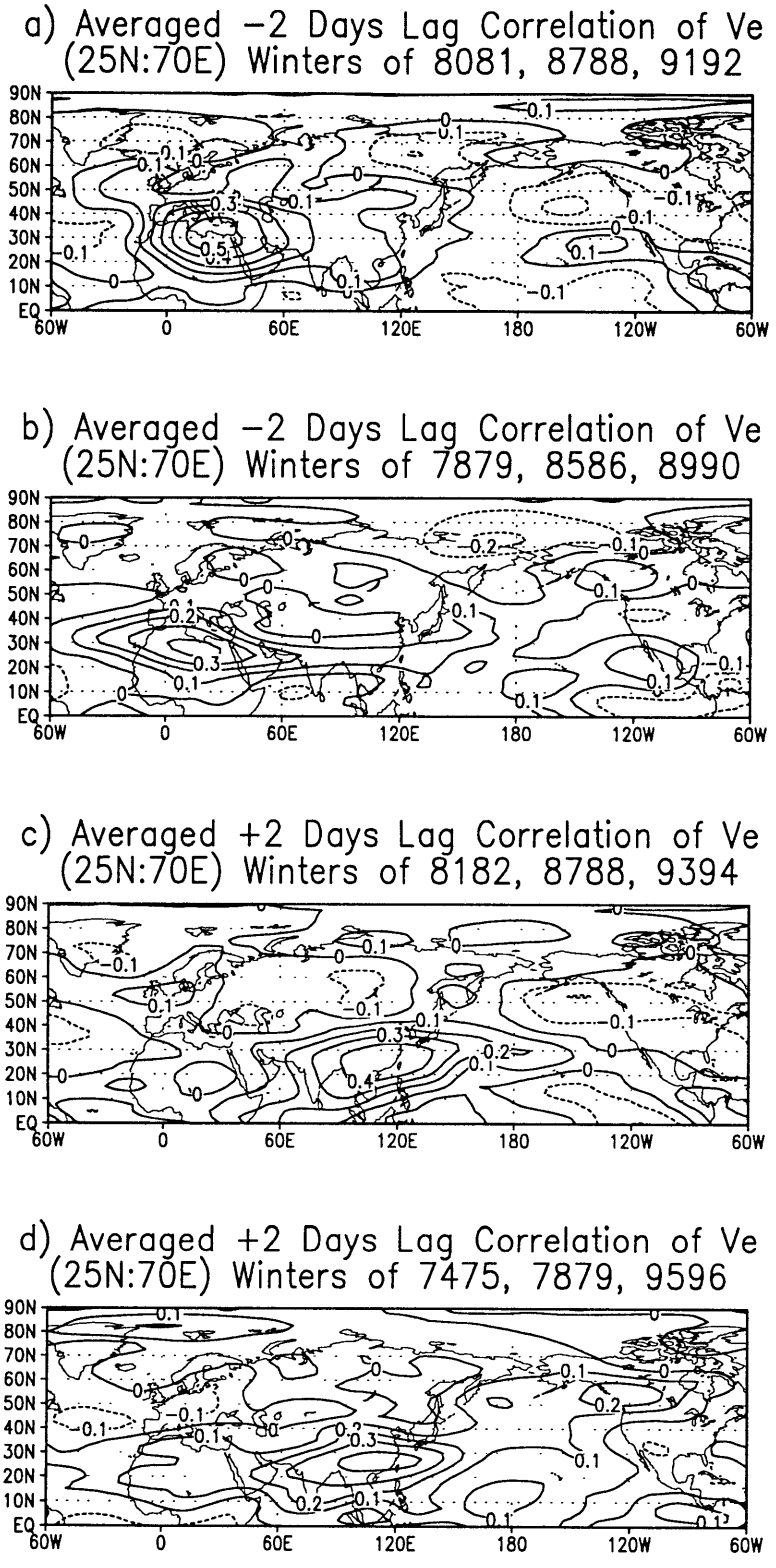

Figure 3-35: a) -2 Days timelag correlation of *ve* averaged over the high composite years in Fig. 3-27a). b) Same as a) except for the low composite years in Fig. 3-27b). c) +2 days timelag correlation of *ve* averaged over the high composite years in Fig. 3-28a). d) Same as c) except for the low composite years in Fig. 3-28b). Contour interval 0.1.

Chapter 4

Spatially Coherent Path

4.1 Geographical distribution of spatially coherent path of baroclinic waves

The concept of spatial coherence of baroclinic waves will be introduced next to describe the temporal evolution of spatial structure of baroclinic eddies. Similar to what we did in calculating 12-hourly phase velocity, we construct a base box around each base point at certain time and construct some reference boxes around base box 12 hours later. The only difference is the size of box is taken to be the typical scale of mid-latitude baroclinic eddies (43 longitudinal degrees and 28 latitudinal degrees in both winter and summer). Then the spatial correlations between v' in the base box and in the reference boxes are calculated. The maximum correlation thus can be determined and regarded as the indication of spatial coherence of passing waves at certain time. Based on the 16-season data (12-hourly, 1980-1996 for winter and 1980-1995 for summer), we calculate 12-hourly spatial coherence fields and average all 12-hourly maps together to get statistical result of spatial coherence which will be called as spatial coherence index (SCI hereafter) of baroclinic waves.

SCI patterns of baroclinic waves in winter and summer are shown in Figs. 4-1c and 4-1d respectively. Since the time interval we choose is only 12 hours, the spatial correlations of waves in such a short time interval remain fairly high. Even

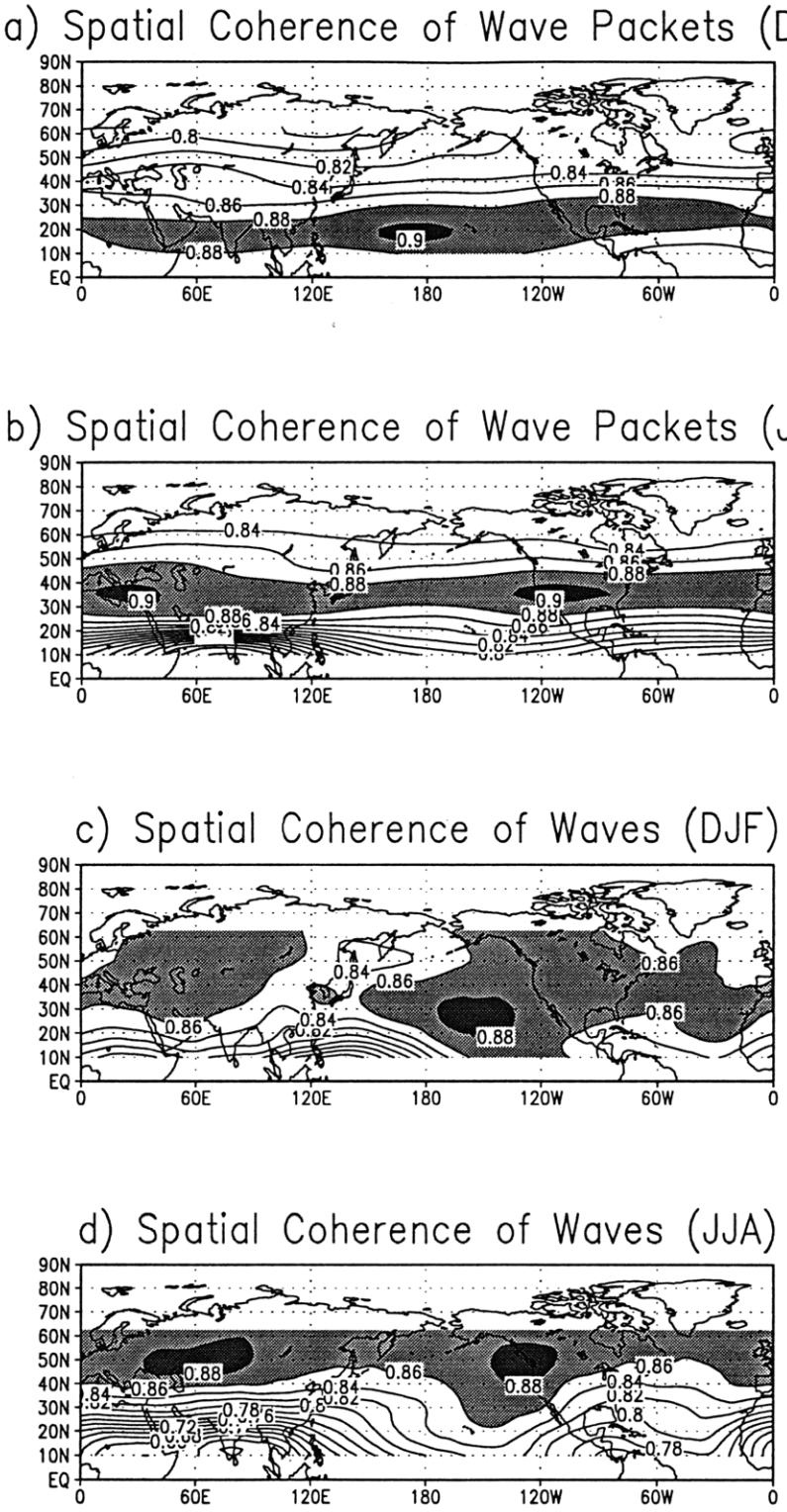

Figure 4-1: a) 16-winter mean of spatial coherence of wave packets. b) 16-summer mean of spatial coherence of wave packets. c) 16-winter mean of spatial coherence of waves. d) 16-summer mean of spatial coherence of waves. Contour interval 0.02. The different shades in a) and b) represent values greater than 0.88 and 0.9, while those in c) and d) represent values greater than 0.86 and 0.88.

the difference between higher coherence ($\sim$ 0.9) and lower coherence ($\sim$ 0.8) is not large, we still can expect such a small difference will develop and finally lead to large deviation of coherence in longer time interval. In winter, we can see the coherent band (dedicated by dark colors) covers the mid-high-latitude regions except that there is a break near the Pacific jet core where growth of baroclinic eddies is prominent (Fig. 3-4a). It gives hints that chaotic baroclinic developments in winter can reduce the spatial coherence of passing waves. Spatial coherence in low latitude, however, is weaker. In summer, the coherent band shifts to higher latitude, probably due to the growth of eddies in low latitude (Fig. 3-4b). SCI of baroclinic waves involves the spatial coherence of wave packets and carrier waves at the same time, and it's difficult to distinguish them only from above results.

4.2 Geographical distribution of spatially coherent path of baroclinic wave packets

Similar to what we did in last section, we compute the spatial coherence index of baroclinic wave packets. The difference is we use daily ve fields, rather than v', and the size of box [1] is larger (103 longitudinal degrees, 33 latitudinal degrees in winter and 93 longitudinal degrees, 28 latitudinal degrees in summer). In Figs. 4-1a and 4-1b, we show SCI patterns of baroclinic wave packets in winter and summer respectively. In both seasons, the mid-latitude SCI patterns are very continuous and systematic and show little influence of baroclinicity (as well as other basic states such as seasonal mean wind and meridional IPV gradient) because no corresponding zonal variations in SCI patterns can be found as in baroclinicity and other basic states distribution (For baroclinicity and IPV gradient, see Figs. 1-4 and 1-5. For Ubar, please see CY). Thus it's not evident to say that spatial coherence of baroclinic wave packets depends on baroclinicity. In other words, the observed break of mid-latitude coherent band

[1] The size of box is larger than the value we took before for group velocity because we are interested in the coherence of the whole spatial packet. We take it about the same size of a typical wave packet seen in 12-hourly ve fields. But actually our result doesn't depend on the exact size of box.

(shown in last section) in winter may come from carrier waves, i.e., phase parts of waves. From Figs. 4-1a and 4-1c, it's seen that spatial coherence of mid-latitude wave packets in winter is a bit lower than the coherence of waves, which suggests the way to forcast weather by exploring the evolution of wave packets may not work. Our calculation shows spatial coherence of mid-latitude wave packets in summer is higher than in winter (see Figs. 4-1a and 4-1b). Lee and Held suggested the much more confined meridional wave group path in summer could favor coherence. [2] We can see this may also be true for spatial coherence in Northern Hemisphere. The streamline patterns of group velocity indicate the meridional confinement of mid-latitude wave groups is stronger in summer than in winter (see Figs. 3-1c and 3-2c). However, the streamline in summer in low latitude reveals a stronger meridional propagation than in winter. From Figs. 1-5a, 1-5b, 4-1a and 4-1b, it's seen that spatially coherent path (dedicated by dark colors) are located in the regions of low IPV gradient, no matter in winter or summer. In addition, SCI of wave packets decreases with latitude from subtropics in winter. In summer, it reaches the peak in middle latitude. What accounts for this interseasonal shift of the position of spatially coherent path is also a question of interest.

[2]They didn't specify it for spatial coherence.

Chapter 5

Interpretation of Spatial Coherence, Temporal Coherence and Baroclinic Wave Guides

Let's consider a simple 2-D wave $\psi(x,t)$ as:

$$\psi(x,t) = \frac{1}{\sqrt{2\pi}} \int_{-\infty}^{+\infty} \phi(k) exp[i(kx - wt)]dk \tag{5.1}$$

where w and k are real and linear dispersion relation is $w = w(k)$. In the atmosphere, baroclinic waves grow mainly due to baroclinic instability and we need to consider the case of complex w. In spatial-temporal instability theory, both w and k are taken as complex and group velocity in usual meaning loses its mathematical base. Hence whether below analysis will be valid when complex w or k or both are involved remains open to discussion. However, if baroclinicity is weak (e.g., in Nothern Hemisphere summer) and w and k can be regarded as real, then we expect below analysis works well. Assuming wave numbers with the highest energy density concentrate near certain wave number k_0, we can Taylor expand $w(k)$ as:

$$w(k) = w(k_0) + (\frac{dw}{dk})_{k_0}(k - k_0) + \frac{1}{2}(\frac{d^2w}{dk^2})_{k_0}(k - k_0)^2 + \cdots$$

$$\approx w_0 + Cg(k - k_0) + \frac{B}{2}(k - k_0)^2 \tag{5.2}$$

where $Cg = (\frac{dw}{dk})_{k_0}$ is group velocity and $B = (\frac{d^2w}{dk^2})_{k_0}$. Substituting (5.2) into (5.1) yields:

$$\psi(x,t) \approx \frac{1}{\sqrt{2\pi}} exp[i(k_0 x - w_0 t)] \int_{-\infty}^{+\infty} \phi(k) exp\{i[P(x - Cgt) - \frac{B}{2}P^2 t]\} dP \tag{5.3}$$

Here, $P = k - k_0$. Assume $\phi(k)$ is Gaussian form:

$$\phi(k) = exp(-\frac{P^2}{2l^2})$$

and substitute $\phi(k)$ into (5.3) we have:

$$\psi(x,t) \approx \frac{1}{\sqrt{2\pi}} exp[i(k_0 x - w_0 t)] \int_{-\infty}^{+\infty} exp[iP(x - Cgt) - \frac{P^2}{2}(iBt + 1/l^2)] dP$$

$$= exp[i(k_0 x - w_0 t)] \frac{l}{\sqrt{1 + iBl^2 t}} exp[-\frac{(x - Cgt)^2 l^2}{2(1 + iBl^2 t)}]$$

The wave amplitude can be expressed as:

$$| \psi(x,t) |^2 = \frac{l^2}{\sqrt{1 + B^2 l^4 t^2}} exp[-\frac{l^2}{1 + B^2 l^4 t^2}(x - Cgt)^2] \tag{5.4}$$

5.1 Spatial coherence of wave packets

In general, spatial coherence of wave packets is referred to spatial correlation between the whole spatial packet (not packet value at one grid point) and the same packet (deformation allowed) some time later. Next, theoretical analysis of dispersion of spatial wave packet in the atmosphere will be given.

From equation (5.4), the length scale of spatial packet at any fixed time t is:

$$L = \frac{\sqrt{1 + B^2 l^4 t^2}}{l} \tag{5.5}$$

Obviously, the value of L at $t = 0$ is:

$$L_0 = 1/l$$

Hence L can be written as:

$$L = L_0\sqrt{1 + B^2t^2/L_0^4} \tag{5.6}$$

We can get following characteristics of wave packet:

a) When $t \ll |L_0^2/B|$, $L \approx L_0$ and wave packet is weak-dispersive.

b) When $t \gg |L_0^2/B|$, $L \gg L_0$ and the shape of wave packet changes much.

c) If

$$B = (\frac{d^2w}{dk^2})_{k_0} = (\frac{dCg}{dk})_{k_0} = 0$$

, wave packet is non-dispersive.

d) If the length scale of wave packet is longer, dispersion is weaker. This can be seen from (5.6):

$$L/L_0 = \sqrt{1 + \frac{B^2t^2}{L_0^4}}$$

Above analysis shows general nature of any kind of wave packet. Next we apply it to wave packets in the atmosphere for following cases.

5.1.1 Barotropic PV front

Recently, Morgan (1995) tried to figure out a basic state for the study of synoptic-scale waves, in which synoptic eddies and other transients have been removed, but dynamically important features (e.g., PV gradient) of the observed distribution have been retained. To describe how waves propagate in a basic state with strong merid-

ional PV gradient, he gave an ideal PV front theory. In the condition that there is a PV jump (δq) at some latitude y_0 in the barotropic atmosphere with $f-plane$ approximation, dispersion relation can be expressed as:

$$w = kU(y_0) - \frac{\delta q}{2} \tag{5.7}$$

Thus,

$$B = (\frac{d^2w}{dk^2})_{k_0} = 0$$

and

$$L/L_0 = 1$$

where $U(y_0)$ is the zonal wind velocity at y_0. We can see the wave packet is non-dispersive. Since this is an ideal condition with meridional PV gradient expressed by a delta function, we shall consider another case with, e.g., continuous PV gradient and $\beta-plane$ approximation.

5.1.2 Barotropic continuous PV gradient

The leading approximation of WKB solution to the linear QGPV equation on $\beta-plane$ gives the dispersion relation as:

$$w = k\overline{U} - k\frac{\overline{q}_y}{K^2} \tag{5.8}$$

Neglect meridional structure and assume $K^2 = k^2$ then we have:

$$w = k\overline{U} - \frac{\overline{q}_y}{k}$$

Thus,

$$B = (\frac{d^2w}{dk^2})_{k_0} = -2\overline{q}_y/k_0^3$$

Substituting above result to (5.6) yields:

$$L/L_0 = \sqrt{1 + t^2 \frac{4\overline{q}_y^2}{k_0^6 L_0^4}}$$

Hence we can see $\overline{q}_y = \beta - \frac{\partial^2 \overline{u}}{\partial y^2} = 0$ also leads to a weak dispersion of wave packets. In addition, for those waves with longer spatial packet (larger L_0) and shorter spatial carrier wave (larger k_0), dispersion is weaker and vice versa.

5.2 Temporal coherence of wave packets

The temporal coherence of wave packets is defined to be the correlation between the temporal packet in one position and that in other position. In mathematics, temporal coherence is closer to the timelag correlation. Hence the first guess is temporal coherence of wave packets could influence PCI distribution. Next we shall give theoretical analysis on temporal coherence.

From equation (5.4), we can see that for any fixed x, when

$$t_0 = x/Cg$$

$\mid \psi(x,t) \mid^2$ reaches its maximum. The e-folding time t_1 for the wave amplitude can be expressed in below form:

$$\frac{l^2(x - Cgt_1)^2}{1 + B^2 l^4 t_1^2} = 1$$

Above form can also be written as:

$$\frac{Cg^2 l^2 (t_1 - t_0)^2}{1 + B^2 l^4 t_1^2} = 1$$

The time scale of temporal packets is:

$$T = t_1 - t_0 = \frac{\sqrt{1 + B^2 l^4 t_1^2}}{Cgl} \tag{5.9}$$

Thus we can see the time scale of temporal packet is determined by l which has relation with the wave number spectrum (assumed to be a Gaussian form at the beginning of this chapter), group velocity and B. It's natural to expect that the temporal coherence of wave packet will depend on the relative change of T in fixed time interval (dt) following group velocity:

$$\mid \frac{d_g T}{T} \mid = \mid \frac{1}{T}\frac{d_g T}{dt}dt \mid = \mid \frac{1}{T}(\frac{\partial T}{\partial t} + Cg\frac{\partial T}{\partial x})dt \mid$$

Assuming l is constant and $1+B^2 l^4 t_1^2$ is slow varying and also can be taken as constant, we have:

$$\mid \frac{d_g T}{T} \mid \propto \mid \frac{1}{Cg}(\frac{\partial Cg}{\partial t} + Cg\frac{\partial Cg}{\partial x}) \mid \tag{5.10}$$

Since 12-hourly group velocity can be zero somewhere which will make $\frac{d_g T}{T}$ approach infinity, thus 12-hourly calculation of (5.10) is impossible. However, it's reasonable to expect

$$\overline{(\mid \frac{\partial Cg}{\partial t} + Cg\frac{\partial Cg}{\partial x} \mid)} / \overline{Cg} \tag{5.11}$$

which is plotted in Fig. 5-1a will depict main points in physics. Here, bar represents 16-winter mean. The lower value represents higher temporal coherence. We can see it is fairly similar to the observed PCI distribution. Hence we believe the temporal coherence of wave packet is important to understand the baroclinic wave guides, rather than spatial coherence of wave packet. From equation (5.10), it's straight forward to conclude that the change of group velocity will lead to change of temporal coherence. Since we don't demodulate v' in time, it is difficult to distinguish the effect of temporal coherence of packets from that of carrier waves in our calculation of timelag correlation. Considering the relation between upper-level basic state flow and group velocity and the possible linkage between temporal coherence and timelag

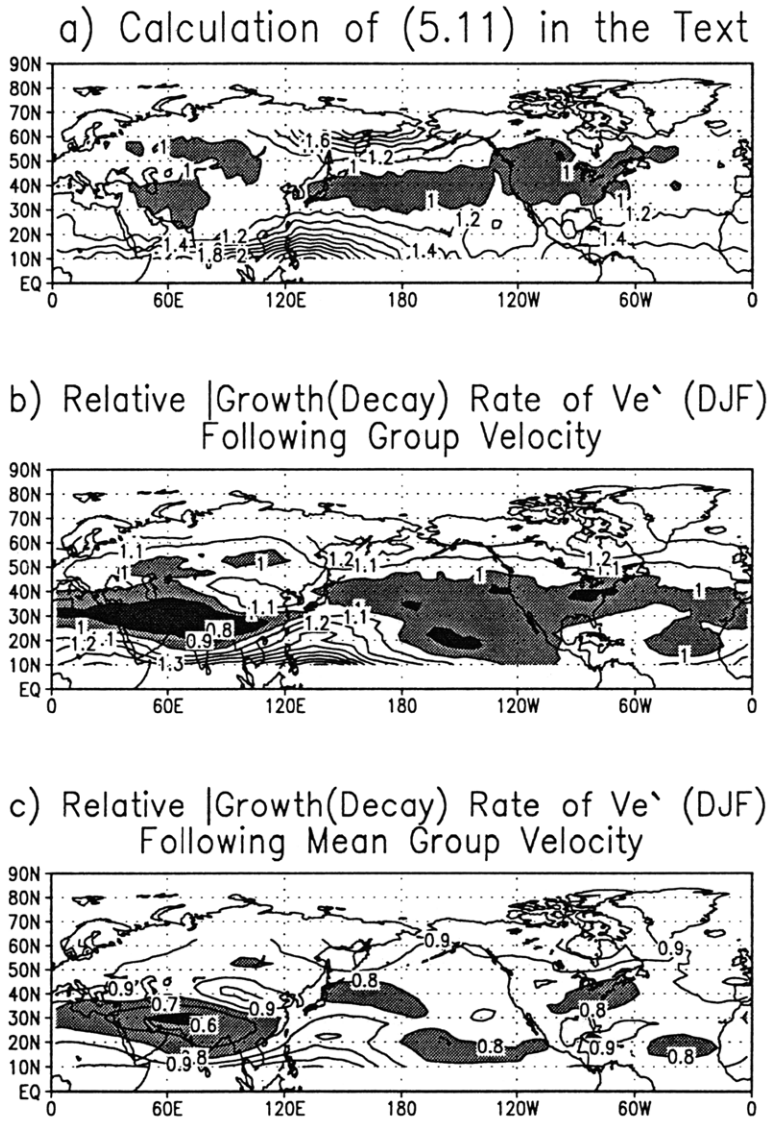

Figure 5-1: a)$(|\overline{\frac{\partial Cg}{\partial t} + Cg\frac{\partial Cg}{\partial x}}|)/\overline{Cg}$ in winter. b) Relative change of ve' following group velocity in winter, according to equation (5.15) in the text. c) Relative change of ve' following mean group velocity in winter, according to equation (5.14) in the text. Contour intervals are 0.2 $\times 10^{-5} s^{-1}$ in a), and 0.1 $\times 10^{-5} s^{-1}$ in b) and c). The shades represent values less than 1 in a), 0.9 and 1 in b), 0.6 and 0.8 in c).

correlation, the fact (we showed in section 3.6) that higher timelag correlations are sometimes accompanied by stronger Ubar can be partly explained.

Description of timelag correlation of *ve* and PCI in more details will be given in the next section. PCI will be shown to resemble the relative growth (decay) rate of wave packets (both spatially and temporally) following (statistical) group velocity.

5.3 Timelag correlation of *ve* and PCI

Let us consider the positive timelag correlation between $ve'(x,t)$ and $ve'(x+dx, t+dt)$. Here, ve' (deviation from seasonal mean) is the perturbation field of *ve* and is used in calculation of timelag correlation, dx is the distance between base point and certain point around, and dt can be regarded as timelag. Downstream index of wave packets coherence of certain base point, as we have defined, is the maximum value of the positive timelag correlations of that base point. Recall the method to calculate statistical group velocity ($\overline{Cg}$) using timelag correlation of *ve* (For readers not familiar with this, please refer to CY), it's straight forward to get:

Packet downstream coherence index will be the correlation between base point and the point wave packets (starting from base point x at time t) reach (on average) after time interval dt, saying, the moving distance for downstream index is $dx = \overline{Cg}\ dt$.

The positive timelag correlation between $ve'(x,t)$ and $ve'(x+\overline{Cg}dt, t+dt)$ is given by:

$$r(x, x+\overline{Cg}dt) = \frac{\sum_{t=1}^{N} ve'(x,t)ve'(x+\overline{Cg}dt, t+dt)}{\sigma(x)\sigma(x+\overline{Cg}dt)}$$

where

$$\sigma(x) = [\sum_{t=1}^{N} ve'^2(x,t)]^{\frac{1}{2}}$$

$$\sigma(x+\overline{Cg}dt) = [\sum_{t=1}^{N} ve'^2(x+\overline{Cg}dt, t+dt)]^{\frac{1}{2}}$$

The absolute change (positive) between $ve'(x,t)$ and $ve'(x+\overline{Cg}dt, t+dt)$ is:

$$\mid ve'(x+\overline{Cg}dt, t+dt) - ve'(x,t) \mid = \mid \frac{\partial ve'}{\partial t} + \overline{Cg}\frac{\partial ve'}{\partial x} \mid dt \tag{5.12}$$

The timelag correlation is high if there exists a strong linear relation between the observed time series $ve'(x,t)$ at a fixed position x and $ve'(x+\overline{Cg}dt, t+dt)$ at the other fixed position $x+\overline{Cg}dt$. Say, if the growth (decay) is linear,

$$ve'(x,t) = Cve'(x+\overline{Cg}dt, t+dt), \ (C \text{ is a constant})$$

then the timelag correlation will still be one, which suggests that the timelag correlation isn't directly associated with the growth or decay of above two time series. However, Lee and Held suggested that coherence of wave packets is inversely related to baroclinicity. The shortcoming of their suggestion is they didn't take the magnitude of ve' into account which is important in calculating the relative change of ve' (defined by equation (5.15)). Obviously, it's the relative change, rather than absolute change of ve', which could possibly have relation with timelag correlation of ve. Based on the comparison between PCI and baroclinicity, Chang and Yu argued it's not true that coherence of wave packets is inversely related to baroclinicity. They suggested that PV gradient is the key element to determine the coherence of wave packets. On the other hand, we find PV gradient distribution also isn't in perfect agreement with PCI. Thus it's of interest to consider the relative change (positive) of ve'. When we take meridional group velocity into account and look at the relative change between $ve'(\vec{x},t)$ and $ve'(\vec{x}+\overrightarrow{\overline{Cg}}dt, t+dt)$, we find it is in good agreement with PCI distribution. Next we shall use below form to replace (5.12):

$$\mid ve'(\vec{x}+\overrightarrow{\overline{Cg}}dt, t+dt) - ve'(\vec{x},t) \mid = \mid \frac{\partial ve'}{\partial t} + \overline{Cgx}\frac{\partial ve'}{\partial x} + \overline{Cgy}\frac{\partial ve'}{\partial y} \mid dt \tag{5.13}$$

In order to see statistical result of the relative change (positive) of ve', we consider below formulas:

$$\overline{seasonal\ mean\ [\mid \frac{\partial ve'}{\partial t} + \overline{Cgx}\frac{\partial ve'}{\partial x} + \overline{Cgy}\frac{\partial ve'}{\partial y} \mid / RMS(ve')]} \tag{5.14}$$

and

$$\overline{seasonal\ mean\ [|\ \frac{\partial ve'}{\partial t} + Cgx\frac{\partial ve'}{\partial x} + Cgy\frac{\partial ve'}{\partial y}\ |\ /RMS(ve')]} \qquad (5.15)$$

where bar represents 16-winter mean and RMS(ve') is the standard deviation of ve', which represents the magnitude of ve'. The reason for replacing $\overline{Cgx}$ and $\overline{Cgy}$ in (5.14) by Cgx and Cgy in (5.15) is just due to the purpose of more convenient interpretation in physics. For example, (5.15) represents mean relative change of wave packets following group velocity. Later we shall see they give similar results.

If we consider negative timelag correlation between $ve'(\vec{x}, t)$ and $ve'(\vec{x}+\vec{dx}, t+dt)$, the moving distance for packet upstream coherence index is:

$$dx = \overline{Cgx}\ dt \text{ and } dy = \overline{Cgy}\ dt,\ (dt < 0)$$

Following the same steps as downstream index and recalling that PCI is just the average of downstream and upstream index, we would like to see if (5.14) and (5.15) (approximation of (5.14)) can pick up main characteristics of PCI. Plotting results of (5.14) and (5.15) are shown in Figs. 5-1c and 5-1b respectively, where $\frac{\partial ve'}{\partial t}(t)$ is calculated by

$$\frac{ve'(t+\delta t) - ve'(t-\delta t)}{2\delta t}$$

and δt is taken to be 12-hour interval. Basically, we can see they own much similarity to PCI pattern in Fig. 1-2c and schematic wave guide showed in CY. For example, two branches are observed over Asia. And regions with maximum value are located in South Asia and North Africa.

As we have analyzed above, PCI has an uncertain relation with the growth or decay of ve'. But the physical meaning of formula (5.15) does represent the relative growth (decay) of wave packets. So it's an interesting question why relative change of propagating wave packets can resemble PCI so well.

Chapter 6

Summary and Conclusion

Downstream development of baroclinic wave packets is well known to radiate energy to the regions of low baroclinicity and cause the zonal extension of storm trcaks in midlatitudes. Recently, it has attracted much attention of investigators to study the behaviour of baroclinic waves propagation in the storm tracks. The major purpose of this thesis is to investigate the properties of baroclinic waves propagation and their relation with interannual variability of storm tracks. Below questions have been raised in our study: What mechanism accounts for the geographical distribution of baroclinic wave guides? Can the interannual variations of baroclinic waves propagation influence the interannual variability of storm tracks? Are the variations of basic states important to the interannual variability of waves propagation? And what is the physical linkage among the interannual variabilities of storm tracks, baroclinic waves propagation and basic states ?

The wave coherence index (WCI) and packet coherence index (PCI) are computed to depict the characteristics of waves and wave packets propagation. The band with higher PCI is referred to as baroclinic wave guides. Geographical distribution of baroclinic wave guides was shown to be different with the distribution of storm tracks. The most coherent wave guide is located in the South Asia and North Africa, which is definitely out of storm tracks. Coherence change of propagating waves and wave packets was found to be somehow inversely related to the baroclinicity and it suggests chaotic development in regions of high baroclinicity may reduce the coherence of

passing waves and wave packets. The distribution of baroclinic wave guides is in good agreement with the relative change of wave packets following group velocity. In chapter 2, interannual seesaws of storm tracks, westerlies, and baroclinicity in winter season were shown. In the Pacific and Atlantic, we found intensification of storm track is accompanied by stronger basic state flow in certain sides of Ubar seesaw. The intensity of Pacific storm track seems to be controlled mainly by the EOF1 mode of Ubar, while the relation between Ubar and the Atlantic storm track is not so high. We suggested that nonlinear developments of baroclinic eddies in the Atlantic storm track may lead to much more complex variation of its intensity.

The 12-hourly group velocity and phase velocity have been obtained by tracking the most spatially coherent waves and wave packets. The growth and decay rate of wave amplitudes following group velocity were calculated in Chapter 3. The regions of prominent growth in winter are located near the Pacific jet core of the highest baroclinicity, while the main regions of growth in summer are located downstream of strong baroclinic areas. We examined the interannual variabilities of RMS(v'), WCI and PCI, and found the first leading EOF mode of interannual anomalies of RMS(v') is closely associated with the basic state flow and baroclinicity, while at least two other leading modes have relation with WCI or PCI. Further investigation of timelag correlation of v' by choosing base points along the baroclinic wave guides shows that higher timelag correlations are always accompanied by the intensification of local storm track, and sometimes by the stronger basic state flow.

In order to give more complete description of waves structure evolution, we have analyzed difference between concepts of spatial coherence and temporal coherence. The quantitative indications of spatial coherence of baroclinic waves and wave packets were given in Chapter 4. The spatial coherence indices (SCI) of wave and wave packets are computed by applying a box technique to track the propagating waves and wave packets and calculate their spatial correlation with the original packets. We find the spatial coherence is higher in regions with lower meridional IPV gradient, which suggests that PV front theory may not valid in describing spatial coherence of wave packets. The barolinicity which seems to have little influence on SCI of wave packets,

however, projects an obvious effect on SCI of waves. Our calculation showed that mid-latitude SCI in summer is higher than in winter. In winter season, the mid-latitude SCI of baroclinic wave packets is a bit lower than that of baroclinic waves, which suggests that the way to forcast weather by exploring the evolution of wave packets may not work.

In Chapter 5, we gave theoretical interpretation of spatial coherence and temporal coherence of wave packets, assuming both wave number and wave frequency are real. Spatial coherence of wave packets mainly depends on the dispersion relation while temporal coherence is mainly determined by the dispersion relation and group velocity. An approximational calculation of temporal coherence was found to be fairly similar to the distribution of PCI. Thus we suggested that temporal coherence of wave packets is important to timelag correlation, as well as WCI and PCI. The distribution of PCI was shown to be in good agreement with the relative change of wave packets following group velocity, which is an interesting observation still open for discussions.

References

Berberry, E.H., and C.S. Vera, 1996: Characteristics of the Southern Hemisphere winter storm track with filtered and unfiltered data. *J. Atmos. Sci.*, **53**, 468-481.

Blackmon, M.L., 1976: A climatological spectral study of the 500 mb geopotential height of the Northern Hemisphere. *J. Atmos. Sci.*, **33**, 1607-1623.

—, M.L., Y.-H. Lee, and J.M. Wallace, 1984: Horizontal structure of 500 mb height fluctuations with long, intermediate and short time scales. *J. Atmos. Sci.*, **41**, 961-979.

Branstator, G., 1995: Organization of storm track anomalies by recurring low-frequency circulation anomalies. *J. Atmos. Sci.*, **52** 207-226.

Briggs, R.J., 1964: Electron-stream interaction with plasmas. M.I.T. Press.

Chang, C.-B., D.J. Perkey, and C.W. Kreitzberg, 1982: A numerical case study of the effects of latent heating on a developing wave cyclone. *J. Atmos. Sci.*, **39**, 1555-1570.

Chang, E.K.M., 1993: Downstream development of baroclinic waves as inferred from regression analysis. *J. Atmos. Sci.*, **50**, 2038-2053.

—, and I. Orlanski, 1993: On the dynamics of a storm track. *J. Atmos. Sci.*, **50**, 999-1015.

—, and D.B. Yu, 1997: Characteristics of wave packets in storm tracks. Part I: Northern hemisphere winter. Submitted to *J. Atmos. Sci.*

—, 1997: Characteristics of wave packets in storm tracks. Part II: Seasonal and hemispheric variations. Submitted to *J. Atmos. Sci.*

Frederiksen, J.S., and C.S. Frederiksen, 1993: Southern hemisphere storm tracks, blocking, and low-frequency anomalies in a primitive equation model. *J. Atmos. Sci.*, **50**, 3148-3163.

Gall, R., 1976: The effects of released latent heat in growing baroclinic waves. *J. Atmos. Sci.*, **33**, 1686-1701.

Hoskins, B.J., and D.J. Karoly, 1981: The steady linear response of a spherical atmosphere to the thermal and orographic forcing. *J. Atmos. Sci.*, **38**, 1179-1196.

—, B.J., I.N. James, and G.H. White, 1983: The shape, propagation and mean-flow interaction of large-scale weather systems. *J. Atmos. Sci.*, **40**, 1595-1612.

—, B.J., M.E. McIntyre, and A.W. Robertson, 1985: On the use and significance of isentropic potential vorticity maps. *Quart. J. Roy. Meteor. Soc.*, **111**, 877-946.

—, B.J., and P.J., Valdes, 1990: On the existence of storm tracks. *J. Atmos. Sci.*, **47**, 1854-1864.

Kalnay, E., M. Kanamitsu, R. Kistler, W. Collins, D. Deaven, L. Gandin, M. Iredell, S. Saha, G. White, J. Woollen, Y. Zhu, M. Chelliah, W. Ebisuzaki, W. Higgins, J. Janowiak, K.C. Mo, C. Ropelewski, J. Wang, A. Leetmaa, R. Reynolds, R. Jenne, and D. Joseph, 1996: The NCEP/NCAR 40-year reanalysis project. *Bull. Amer. Meteor. Soc.*, **77**, 437-471.

Lau, N.-C., 1988: Variability of the observed midlatitude storm tracks in relation to low-frequency changes in the circulation pattern. *J. Atmos. Sci.*, **45**, 2718-2743.

Lee, S., and I.M. Held, 1993: Baroclinic wave packets in models and observations. *J.*

Atmos. Sci., **50**, 1413-1428.

—, S., 1995: Localized storm tracks in the absence of local instability. *J. Atmos. Sci.*, **52**, 977-989.

Lim, G.H., and J.M. Wallace, 1991: Structure and evolution of baroclinic waves as inferred from regression analysis. *J. Atmos. Sci.*, **48**, 1718-1732.

Merkine, L.O., 1977: Convective and absolute instability of baroclinic eddies. *Geophys. Astrophys. Fluid Dyn.*, **9**, 129-157.

Morgan, M.C., 1994: An observationally and dynamically determined basic state in the study of synoptic scale waves. Ph.D. dissertation, Department of Earth, Atmospheric, and Planetary Sciences-Center for Meteorology and Physical Oceanography, M.I.T., 34 pp.

Murty, T.S., G.A. Mcbean, and B. Mckee, 1983: Explosive cyclogenesis over the northeast pacific ocean. *Mon. Wea. Rev.*, **111**, 1131-1135.

Nakamura, H., 1992: Midwinter suppression of baroclinic wave activity in the Pacific. *J. Atmos. Sci.*, **49**, 1629-1642.

Nielsen-Gammon, J.W., and R.J. Lefevre, 1996: Piecewise tendency diagnosis of dynamical processes governing the development of an upper-tropospheric mobile trough. *J. Atmos. Sci.*, **53**, 3120-3142.

Peixoto, J.P., and A.H. Oort, 1992: *Physics of Climate.* Amer. Inst. of Phy. 492 pp.

Pierrehumbert, R.T., 1984: Local and global baroclinic instability of zonal varying flow. *J. Atmos. Sci.*, **41**, 2141-2162.

Roebber, P.J., 1984: Statistical analysis and updated climatology of explosive cyclones. *Mon. Wea. Rev.*, **112**, 1131-1135.

Sanders, F., and J.R. Gyakum, 1980: Synoptic-dynamic climatology of the "bomb", *Mon. Wea. Rev.*, **108**, 1589-1606.

Simmons, A.J., and B.J. Hoskins, 1979: The downstream and upstream development of unstable baroclinic waves. *J. Atmos. Sci.*, **36** 1239-1254.

Swanson, K., and R.T. Pierrehumbert, 1994: Nonlinear wave packet evolution on a baroclinically unstable jet. *J. Atmos. Sci.*, **51**, 384-394.

Trenberth, K.E., 1991: Storm tracks in the southern hemisphere. *J. Atmos. Sci.*, **48**, 2159-2178.

Wallace J.M., G.H. Lim, and M.L. Blackmon, 1988: Relationship between cyclone tracks, anticyclones tracks, and baroclinic waveguides. *J. Atmos. Sci.*, **45**, 439-462.

Whitaker, J.S., and R.M. Dole, 1995: Organization of storm tracks in zonally varying flows. *J. Atmos. Sci.*, **52**, 1178-1191.